Lei Zhao

Dynamic Modelling and Control Design of Pre-combustion Power Cycles

Thesis for the degree of philosophize doctor
Trondheim, August 2012

Norwegian University of Science and Technology
Faculty of Information Technology, Mathematics and Electrical Engineering
Department of Engineering Cybernetics

NTNU
Norwegian University of Science and Technology

Thesis for the degree of philosophize doctor

Faculty of Information Technology, Mathematics and Electrical Engineering
Department of Engineering Cybernetics

ISBN 978-82-471-3756-7 (printed version)
ISBN 978-82-471-3757-4 (electronic version)
ISSN 1503-8181
ITK Report 2012-5-W

Doctoral theses at NTNU, 2012:227

Printed by NTNU-trykk

Summary

Pre-combustion capture is an important CCS technology. Pre-combustion capture of CO_2 incurs less of an energy penalty than current post combustion technologies. For this type of reforming to be competitive for power generation, excellent operability and robustness is required. Important for this is a thorough understanding of the system dynamics and a robust control structure design. Therefore the dynamic modelling and control design of two pre-combustion power cycles, i.e., a hydrogen membrane reformer (HMR) based power cycle and an autothermal reforming (ATR) based power cycle, are studied.

The first contribution of this thesis is to develop new mathematical models of the two novel pre-combustion power cycles based on first principles. The pre-combustion gas power cycle plants consist of reformers and separation units, compressors, gas and steam turbines and a heat recovery system. Analysis of dynamic models at an early stage of design can give valuable information to control structure design as well as to further process design. Dynamic behaviours of the critical reactors as well as the whole plants are investigated based on these models. The simulations are focused on how different process inputs affect the important variables in the system, e.g., SOT, S/C ratio, TIT, GT power, ST power. The simulations show that both the steady state and dynamic behaviour of the plant depend strongly on the flow rates of feed streams. Due to the complexity of the system and the nonlinearities of the dynamic responses, a systematic approach to control structure design is advocated.

The second contribution is to design the control structures of the two power cycles by a systematic approach. To determine the control structure, an economic objective is chosen, the degrees of freedoms and constraints are found, and the possible disturbances are assumed. The controlled variables are selected by using self-optimizing control. The results show that the control structure depends on the CO_2 price. Finally, the control structures with well-tuned PI controllers and feedforward controllers are simulated and evaluated. The results show that the designed control structure can result in a stable system and that PI controllers can make the controlled variables converge to desired values. However, some constraints may be violated during the transient period.

The third contribution is to implement MPC controllers with state estimation for the HMR power cycle. The dynamic simulation reveals that constraint violations may be encountered during operation of the HMR power cycle. Therefore, an MPC controller may be used to handle the constraints systematically. Some selected control loops in the control structure of HMR power cycle is replaced with

MPC controllers, and the dynamic simulation results are shown. The results show that because of the nonlinearities, the MPC controllers give a better dynamic behaviour than PI with feedforward controllers for given disturbances. PI with feedforward controllers are easy to implement and do not require much information about the system. However, they may give larger overshoot or constraint violation. MPC controllers can overcome these drawbacks and provide a smoother dynamic performance. Hence, for the HMR power cycle studied here, MPC controllers are recommended above PI controllers.

Finally, the last contribution is the study on benchmarking the two power cycles. The dynamic responses and control structures are compared. The dynamic responses of the two systems have lots in common. The main differences are due to different syngas generators, different operating conditions, and process structure. The designed control structures for both systems give rapid response to load changes and exhibit good load-following capabilities. However, the control structure of the ATR power cycle has a lower complexity as compared to the HMR power cycle.

Contents

List of figures

List of tables

Preface

This thesis is submitted in partial fulfillment of the requirements for the degree of philosophize doctor (PhD) at the Norwegian University of Science and Technology (NTNU).

I have done this work at Department of Engineering Cybernetics (NTNU) in the period August 2008 - September 2012. This work was financially supported by the CCERT project, performed under the strategic Norwegian research program Climit.

Acknowledgments

The special thank goes to my helpful supervisor, Professor Bjarne Foss, for providing me the excellent opportunity and supporting me during my studies.

I am grateful to Finn Michelsen and Knut Ingvar Åsen for their guidance and constant supervision as well as for providing necessary information regarding the project and also for their support in completing the thesis.

Finally, I would like to thank to all my colleagues and people in developing the project and those who have willingly helped me out with their abilities.

Glossary

List of abbreviations

ATR	Autothermal reforming
BFW	Boiler feed water
BT	Buffer tank
CC	Combustion chamber
CCS	CO_2 capture and storage
CV	Controlled variable
CW	Cooling water
DoF	Degree of freedom
FT	Flash tank
GT	Gas turbine
HE	Heat exchanger
HGBL	Pressurized gas vs. boiling liquid
HGCW	Pressurized gas vs. boiler feed water
HGHG	Pressurized gas vs. pressurized gas
HGLG	Pressurized gas vs. low pressure gas
HMR	Hydrogen membrane reformer
HPST	High pressure steam turbine
HRSG	Heat recovery steam generation
IGCC	Integrated gasification combined cycle
KF	Kalman filter
LTWGS	Low temperature water gas shift
LHV	Lower heating value
MTWGS	Medium temperature water gas shift
MPC	Model predictive control
NG	Natural gas
O/C	Oxygen to carbon
PID	Proportional integral derivative
RTO	Real-time optimization
S/C	Steam to carbon
SMR	Steam methane reforming
SOFC	Solid oxide fuel cell
SOH	Syngas outlet hydrogen concentration
SOT	Syngas outlet temperature
ST	Steam turbine

TET	Turbine exhaust temperature
TIT	Turbine inlet temperature
VIGV	Variable inlet guiding vanes
WGS	Water gas shift

Nomenclature

A	Areas $[m^2]$
C	Constant
C_{CO_2}	Captured CO_2 rate $[kmol/kmol]$
C_r	Stoichiometric coefficient
E	Energy $[MW]$
E_S	Heat to raise the temperature to vaporization temperature $[kJ]$
F	Gain from a change of disturbance to the measurements
G	Scaled gain
H	Enthalpy.$[kJ]$
H_c	Selecting matrix for controlled variable
ΔH_r	Enthalpy changes by reactions $[kJ]$
I_d	Inertia of a rotating disc $[kgm^2]$
J	Objective $[€/s]$
K	Constant for reaction rate
L	Loss $[€/s]$
M	Molar mass $[kg/kmol]$
N	Rotation speed
P	Power $[MW]$
Q	Heat transfer $[kJ]$
R	Universal gas constant $[J/Kmol]$
R_s	Equivalent height of fin for heat exchangers.$[m]$
T	Temperature $[K]$
U	Overall heat transfer coefficient $[kJ/sm^2K]$
V	Volume $[m^3]$
W	Work $[MW]$
W_s	Scaling matrix
c	Controlled variable
c_p	Heat capacity $[J/molk]$
c_s	Set of candidate controlled variable
d	Disturbance
e	Differences
h_c	Combination of the controlled variables
k	Constant for reaction rate
k_p	Gain for PI controller
k_i	Gain for integral part of PI controller
l	Length $[m]$
l_m	Membrane thickness $[m]$
l_{shaft}	Radius of rotating disc $[m]$

m	Mass $[kg]$
n	Molar concentration $[kmol]$
$\dot{n}$	Molar flow rate $[kmol/s]$
$\dot{n}_r$	Molar concentration changes per time by reactions $[kmol/s]$
n_d	Dimension of disturbances
n_u	Dimension of inputs
n_y	Dimension of outputs
n^y	Measurement error
p	Pressure $[bar]$
r	Reaction rate $[kmol/s]$
r_{SC}	S/C ratio
r_{CO_2}	Split rate for CO_2 split
t	Time $[s]$
t_s	Sampling time $[s]$
u	Manipulated variable
v	Velocity $[m/s]$
v	Measured disturbances
v_{un}	Unmeasured disturbances
w_n	Measurement noise
w	Width of a single channel for the membrane reactor $[m]$
w_i	Weight $[m]$
x	State
y	Output
z	Axial position $[m]$

Greek Symbols

α	Angle of the inlet vane $[^o]$
α_{bp}	Bypass flow rate proportion for each heat exchanger
α_v	Fraction of feed that is vaporized
γ	Heat capacity ratio.
γ_l	Liquid mole fraction
γ_v	Vapour mole fraction
ϵ	Void fraction
η	Efficiency
λ	Molar fraction
π	Pressure ratio
ρ	Density $[kg/m^3]$

Subscripts

AC	Air compressor
C	Compressor
CO_2C	CO_2 compressor
CV	Variation for compressor by VIGV
L	Load
$Mech$	Mechnical

S	Saturation
T	Turbine
cat	Catalyst
cg	Cold gas
cov	Coveriance
ds	Design value
dl	Non-dimensional
$extr$	Extraction
hg	Hot gas
liq	Liquid
in	Inlet
$isen$	Isentropic
out	Outlet
p	Process gas
$perm$	Permeation
r	Reaction
rc	Reactor
red	Reduced
s	Sweep gas
$surge$	Surge line for GT
$sync$	Syngas cooler
tot	Total
vap	Vapour

Chapter 1

Introduction

1.1 Motivation

CO_2 capture and storage (CCS) is becoming an increasingly important part of any discussion on clean coal and gas based power production. Generation of electricity and heat was by far the largest producer of CO_2 emissions and was responsible for about 41% of the world CO_2 emissions in 2009 (IEA, 2011a). Energy scenarios developed by the International Energy Agency suggest that CCS from power plants might contribute by 2050 to around 10% of the energy related carbon dioxide emission reduction required to stabilize global warming (Finkenrath, 2011). CCS is a potential key contributor to CO_2 emission mitigation, in addition to other important aims such as improving energy efficiency and increasing renewable power generation. Contribution of technologies to reduce power sector CO_2 emissions is about 31% based on report (IEA, 2011b).

CCS is an emerging technology in the power sector, where it has not yet been demonstrated at large scale. Applying CCS to full-size power plants requires scale-up of commercially available CO_2 capture processes. Approaches for CO_2 capture from power plants can be grouped into three categories, post-combustion, which involves capture from flue gases, pre-combustion, which involves capture from high pressure synthesis gas (syngas) streams, and Oxy-fuel, which involves combustion with pure oxygen.

Pre-combustion capture is an important CCS technology. Pre-combustion capture of CO_2 under pressure incurs less of an energy penalty (around 20%) than current post combustion technology (around 30%) at 90% CO_2 capture (Global CCS Institute, 2011). Studies show that, for integrated gasification combined cycle (IGCC), the lowest plant cost with capture is lower than that of the lowest cost post-combustion capture plants and about 11% lower than the Oxy-combustion plants (Davison, 2007). For natural gas combined cycle (NGCC), however, the thermal efficiency of pre-combustion is lower than that of post-combustion due to the lower efficiency of hydrogen fired GT than NG fired GT with current technologies.

For this type of power cycle to be competitive for power generation, excellent operability and robustness is required. Important for this is a thorough understanding of the system dynamics and a robust control structure design.

1.2 Two pre-combustion power cycles

This thesis will study two pre-combustion power cycles. These are a hydrogen membrane reformer (HMR) based power cycle and an autothermal reforming (ATR) based power cycle. Hence, the HMR and ATR power cycles are introduced below.

1.2.1 The hydrogen membrane reformer power cycle

The HMR power cycle, which is described by Smith and co-workers, is a novel pre-combustion power cycle (Smith et al., 2009). This power cycle uses NG as the fuel, and steam reforming to generate syngas. To remove carbon content before the syngas enters the combustion chamber (CC), water gas shift (WGS) reactors and a CO_2 separation process are integrated. Since the start up in 2001 and through 2008, the reactor system was developed through several stages, and different process configurations were evaluated. One of the most cost effective HMR concepts from that study is the case which is studied in this work.

Figure 1.1 shows the layout of the HMR power cycle that is studied in this thesis. The explanation includes nominal values for some key variables. These are values which are specific for the design used in this work. NG ($30°C$, $30bar$) is heated up to $400°C$ by heat exchangers HE1 and HE4 and mixed with steam after removal of sulphur. There are two sources of steam: one is extracted from a high pressure steam turbines (HPST) with temperature $364°C$ and pressure $32bar$, and the other source is boiler feed water (BFW). The BFW is vaporized in a heat exchanger HE5 and a medium temperature WGS (MTWGS) reactor. The mixed steam and NG is fed into a pre-reformer where all the higher order hydrocarbons are converted into a mixture of hydrogen, carbon monoxide, carbon dioxide, methane and steam. The outlet gas from the pre-reformer is first heated up to $750°C$ by HE2 and then fed into the reaction side of the HMR. This reactor is a syngas reactor with a high temperature hydrogen selective membrane inside. Inside the reaction side, methane is reformed to syngas, and parts of the generated hydrogen is permeated through a ceramic membrane to the other (sweep gas) side. The sweep gas is air from the gas turbine (GT). At the sweep gas side, hydrogen is combusted to provide the necessary heat for steam methane reforming (SMR). The outlet streams of the HMR are syngas and oxygen depleted air with a temperature of 1000 to $1100°C$. The extracted air from the GT ($310°C$, $10bar$) is first cooled down to $25°C$. This step is to provide a low inlet temperature for the air compressor. Then, the air is compressed to $24bar$, and heated up to about $750°C$ by heat exchangers HE9 and HE3 before it is fed into the sweep gas side of the HMR. The oxygen depleted air from the HMR is first used to warm up the air from the compressor by heat exchanger HE3, and then fed directly to the combustion chamber. In order to get high thermal efficiency, the heat from the syngas is extracted in several heat exchangers (HE2, HE4, and HE5) and in the pre-reformer. The cooled syngas ($250°C$) goes through the MTWGS and the low temperature WGS (LTWGS) stages to convert CO to H_2. The syngas, which contains mainly H_2, H_2O, and CO_2 after the WGS reactors, is condensed. H_2O is removed by flash tank (FT), and CO_2 is removed by a separation plant and compressed to $150bar$. The remaining gas, mainly H_2, is used as fuel in the combined GT and steam turbine (ST) power cycle.

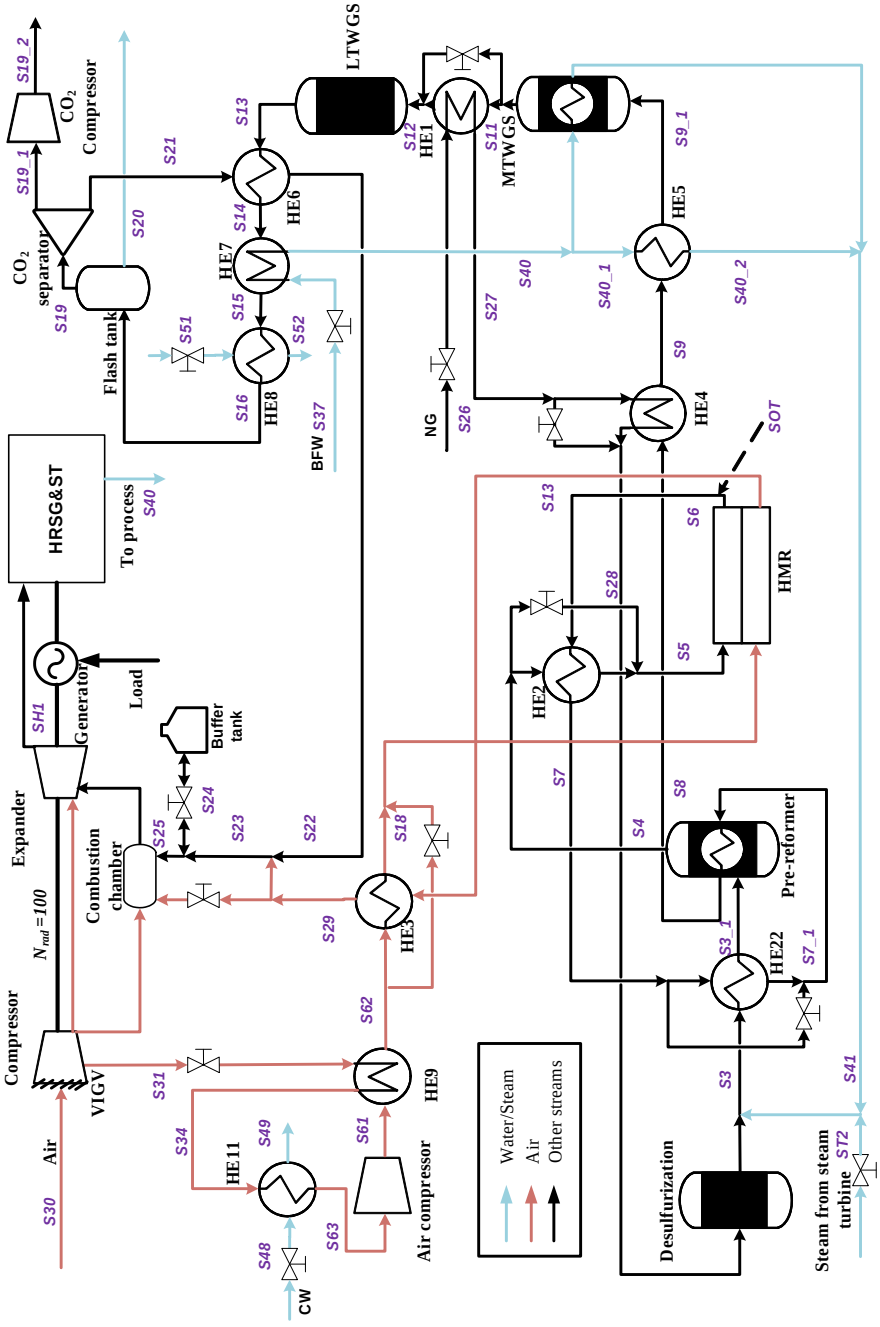

Figure 1.1: The HMR power cycle flow sheet.

1.2.2 The autothermal reforming power cycle

Pre-combustion power plants with ATR technologies are one of the most extensively studied processes for reducing CO_2 emission. Similar to the HMR power cycle, the ATR power cycle includes a desulphurization unit, a pre-reformer, two shift stages, a CO_2 separation unit, and a combined cycle to generate electric power (Nord et al., 2009). The differences are that the ATR power cycle uses an ATR reactor to convert the fuel to syngas which contains air instead of an HMR reactor in the HMR power cycle. Thus, the syngas and air are treated separately in the HMR power cycle. Because of the different reactors, the heat integration in the ATR power cycle is very different.

Different process structures are presented in previous studies, e.g., Fiaschi et al. (2003), Fiaschi et al. (2004), Ertesvåg et al. (2005), Nord et al. (2009), and Corradetti and Desideri (2005). One of the most efficient processes described by Nord et al. (2009) is selected in this study. The process in this work as shown in Figure 1.2 has some small modifications from the original process structure. These are

1. The heat is exchanged through HRSG1, HRGS2, HRSG3, and HRSG4 with streams extracted from the heat recovery steam generation (HRSG), and then, the extracted streams are fed back to the HRSG, while in the process by Nord et al. (2009), the fuel is heated inside the HRSG. This modification is made because of different models of the two processes. However, the two configuration give the same thermodynamic results.
2. Similar to the HMR power cycle, a buffer tank is added to increase the flexibility with respect to load changes in this study.
3. The steam injection to the CC is ignored to make it comparable with the HMR power cycle.
4. The steam used in the CO_2 separation unit is not considered which is to make it comparable to the HMR power cycle's configuration.

1.2.3 Main process units

The main process units for these two power cycles are pre-reforming, HMR, ATR, WGS, and a combined GT and ST cycle. These units are described in some detail.

Pre-reforming

Pre-reforming located upstream of the main reformer reactor is used to completely convert higher hydrocarbons into a mixture of hydrogen, carbon monoxide, carbon dioxide, methane and steam. The gas feed into the pre-reformer is a mixture of NG and steam (Rostrup-Nielsen, 1973).

There are several advantages with the pre-reformer

- Increase the capacity of the main reformer reactor.
- Improve the efficiency.
- Avoid carbon formation.
- Increase the lifetime of downstream steam reformer and shift catalysts.

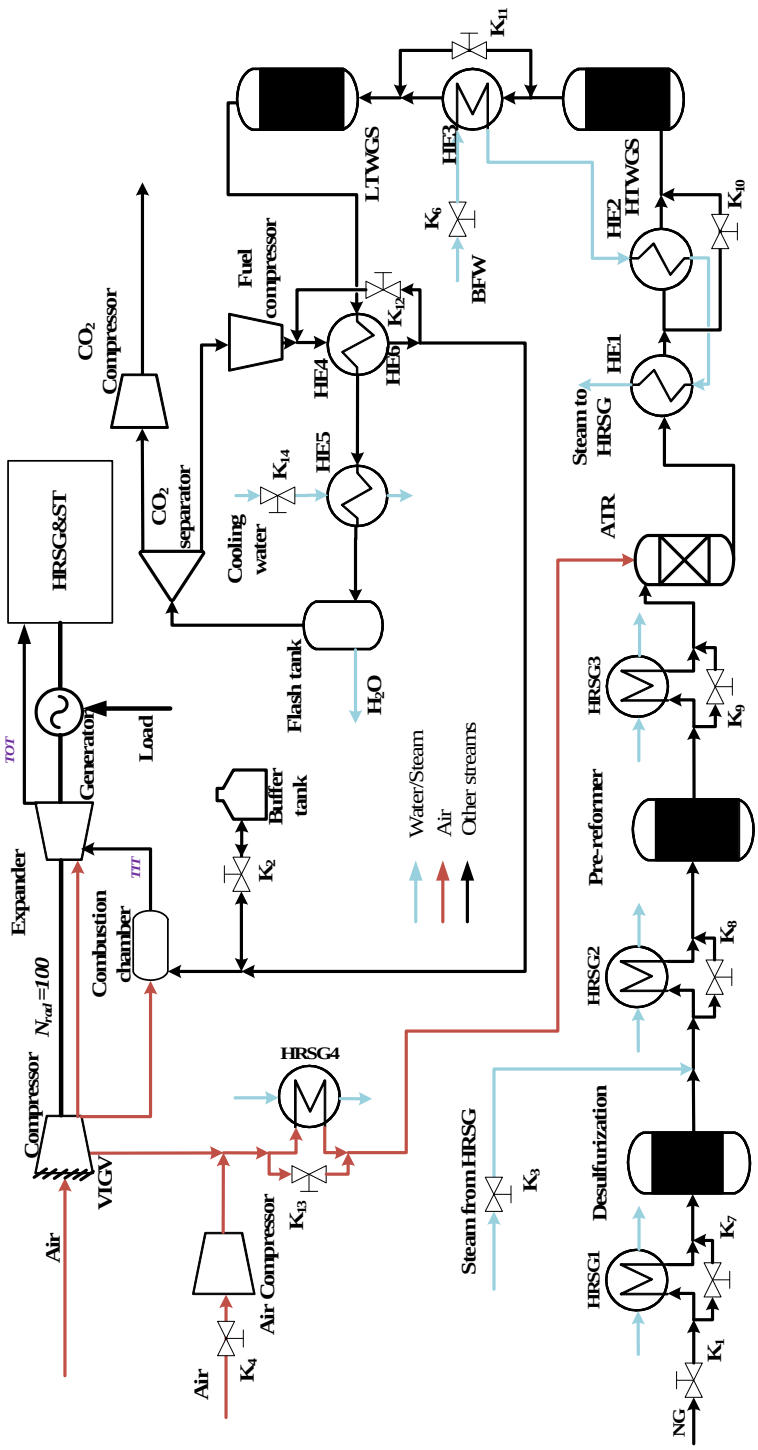

Figure 1.2: The flow sheet of an ATR power cycle.

The reactions in pre-reformer include the endothermic higher order hydrocarbon reforming reactions (reaction 1, 2, and 3) and the equilibration of the exothermic methanation and shift reactions (reaction 4, 5, and 6). The overall reaction is endothermic and the preferred temperature range is $350 - 550^oC$ and pressures of up to $30bar$ (Rostrup-Nielsen and Rostrup-Nielsen, 2002).

1. Ethane conversion
   $C_2H_6 + 2H_2O \leftrightarrow CH_4 + CO_2 + 3H_2$, $\triangle H_{298} = 346\ kJ/mol$
2. Propane conversion
   $C_3H_8 + 2H_2O \leftrightarrow 2CH_4 + CO_2 + 2H_2$, $\triangle H_{298} = 499\ kJ/mol$
3. Butane conversion
   $C_4H_{10} + 2H_2O \leftrightarrow 3CH_4 + CO_2 + H_2$, $\triangle H_{298} = 651\ kJ/mol$
4. Methane reforming
   $CH_4 + H_2O \leftrightarrow CO + 3H_2$, $\triangle H_{298} = 206\ kJ/mol$
5. Water gas shift
   $CO + H_2O \leftrightarrow CO_2 + H_2$, $\triangle H_{298} = -41.2\ kJ/mol$
6. Methane reforming
   $CH_4 + 2H_2O \leftrightarrow CO_2 + 4H_2$, $\triangle H_{298} = 164.8\ kJ/mol$

The pre-reformer are monolithic reactors as shown in Figure 1.3. The reforming reactions take place in one set of channels and the hot gas is in the other set of channels. The selected catalyst for pre-reformer is nickel/alumina.

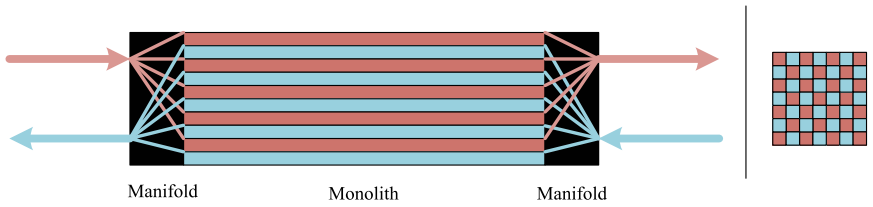

Figure 1.3: Monolithic reactor.

Monolithic membrane reactors structured with parallel micro channels with a square cross section lead to a high packing density and a homogeneous temperature distribution. Therefore these reactors probably offer the most stable and efficient design (Drioli and Giorno, 2009). The micro channels can reduce the gas-phase diffusion limitation and increase membrane surface. This leads to a fast reaction, high heat transfer between each channel, and a compact structure.

Hydrogen membrane reformer

HMR is a reactor to generate syngas using SMR. SMR is a method that converts fossil fuels such as NG into syngas by catalytic reactions. The most important SMR reactions are reaction 1, 2, and 3. Steam reforming of hydrocarbon is an endothermic reaction, high temperatures are preferred. The conversion efficiency of SMR is among the highest current commercially available production methods

(Padro and Putsche, 1999). This technology is preferred for large scale hydrogen generation.

The HMR reactor has a monolith structure similar to the pre-reformer as shown in Figure 1.3. In one set of channels, a thin ceramic hydrogen membrane ($30 - 50\mu m$ thickness) and the reforming catalyst are coated on the support. The process gas from the pre-reformer is fed into these channels. In the other set of channels, permeated hydrogen is combusted by reaction with air to provide heat for steam reforming.

Compared with conventional steam reforming reactors, the main characteristics of the HMR are

- The continuous removal of hydrogen from the reformer breaks the equilibrium, and improves the performance of the reformer.
- The monolith reactor has a high membrane surface area to reactor volume ratio, and is ideal for integrated transfer of H_2 and heat.
- No extra heat source is needed since the combustion of hydrogen provides the heat.

Autothermal reforming

ATR reforms hydrocarbons with steam and air to syngas. It combines the advantages of endothermic SMR and exothermic partial oxidation (reaction 7) to an autothermal process.

7 Partial oxidation

$$CH_4 + \frac{1}{2}O_2 \leftrightarrow CO + 2H_2 \ (\triangle H_{298} = -36kJ/mol)$$

A part of the fuel is burned in the reactor to provide the heat for the steam reforming reaction, so that no external heat source is required and the reaction are thermally self sustaining. Autothermal reforming thus requires a special catalyst, suitable for operating in a high temperature range, since the combustion reaction results in high temperatures. Further, the steam reforming reaction counteracts this, resulting in a stable temperature. The advantages are high thermal efficiency and reduced capital cost (Rostrup-Nielsen and Rostrup-Nielsen, 2002).

Water gas shift

The reformed gas contains a high percentage of carbon monoxide in addition to hydrogen and carbon dioxide. Two steps, MTWGS/high temperature WGS (HTWGS) ($250 - 500\ ^\circ C$) and LTWGS ($200 - 250\ ^\circ C$) (reaction 5) is considered here to convert as much CO to CO_2 as possible for capture. An MTWGS/HTWGS using an iron oxide catalyst converts most of the carbon monoxide to hydrogen and CO_2. The shift reaction is endothermic. In this design, water at saturation temperature is fed in, and the heat from the shift reaction is used to vaporize the water. By this, the reactor can keep a constant temperature and the steam is produced for HMR. Since high temperature favours high CO content even at equilibrium, the MTWGS/HTWGS effluent still contains around $2 - 5\%$ CO. This rest CO is usually treated in a LTWGS including a CuO-ZnO catalyst. The exit gases from the LTWGS contain less than 0.3% CO.

CO_2 separator

There are several ways to separate CO_2 from a mixed gas. Examples are chemical absorption, membrane separation, cryogenic fractionation, and adsorption using molecular sieves (Howard Herzog, 1999). Commercial CO_2 capture plants use separators based on chemical absorption with a monoethanolamine (MEA) solvent, also known as absorption towers. In the tower the flue gas is in contact with an MEA. The MEA selectively absorbs the CO_2, which is sent to a stripper. In the stripper the MEA is heated to release almost all CO_2. The lean MEA is then recycled to the absorber. The monolithic membrane separator which have the same structure as an HMR reactor can also be used. This approach gives a high efficiency.

Combined GT and ST cycle

The GT has an upstream compressor coupled to a downstream turbine, and a combustion chamber in-between them. The compressor draws air from the ambient and compresses it to a pressure in the range $10-35bar$. The fuel is combusted with the air. The hot gas is then expanded to slightly above atmospheric pressure in an expander (Bolland, 2009).

The air is compressed as it flows axially along the compressor shaft in a multistage design. This allows higher efficiency and higher pressure ratios. In the GT, the hot gasses are converted to mechanical energy by turning a turbine wheel. Single shaft design is generally used for electrical power generation because it is simple, efficient, reliable and compact. This kind of engine has one shaft on which all rotating parts of the engine are mounted. The thermal efficiency for a gas turbine is more than 40% (Saravanamuttoo et al., 2009).

An HRSG is a set of energy recovery heat exchangers that recover heat from a hot gas. In gas power cycles, the exhaust gas is the hot gas from GT. The HRSG produces steam to drive STs. The STs extract thermal energy from pressurized steam, and converts it into rotary motion.

Here, a three stage expansion, i.e., high pressure ST, intermediate pressure ST, and low pressure ST is considered. The exhaust gas from the GT flows into the HRSG unit to generate steam for the STs. Cooling water ($30°C$, 120 bar) is fed through an economizer to rise the temperature to the saturation temperature ($325°C$). An evaporator is used to vaporize the water to steam. Future, the steam is heated up to about $560°C$. The hot gas is fed into the high pressure ST and expands to a pressure of about $32bar$. The temperature is reduced to about $360°C$. In order to increase the heat recovery, the steam is reheated in the HRSG, and then expanded by the intermediate pressure ST and the low pressure ST.

1.3 Methodology

This section introduces the methodology used for dynamic modelling and control structure design of the HMR and ATR power cycles. First, dynamic models of the two pre-combustion power cycles are developed. Then, systematic control structure design procedures are implemented, and the control structures which efficiently reduce the cost lost incurred by key disturbances are found. Finally, model predictive

control (MPC) controllers are introduced to improve the dynamic behaviour and in particular handle the constraints during operation.

1.3.1 Dynamic modelling and simulation

A novel mathematical model based on first principles is developed. The purpose of this model is to study dynamics, control and ultimately develop an overall robust operational strategy. Since the process units in the power cycle have different properties and complexities, the modelling strategies used for each unit are different.

The models for the heat exchangers and the ATR reactor are relatively simple. Thus these models use a one-dimensional distributed approach with mass and energy conservation. This is generally described by

$$\begin{aligned} \frac{\partial n}{\partial t} &= -\frac{\partial n}{\partial z} + \dot{n}_r \\ \frac{\partial H}{\partial t} &= -\frac{\partial H}{\partial z} + \dot{H}_r + Q \end{aligned} \tag{1.1}$$

Here, n is molar concentration, $\dot{n}_r$ molar concentration changes per time by reactions, H enthalpy as function of temperature (T), $\dot{H}_r$ enthalpy changes by reactions, and Q heat transfer from the surroundings.

The other reactors are modelled using an aggregated approach, generally described by

$$\begin{aligned} \frac{dn}{dt} &= \dot{n}_{in} - \dot{n}_{out} + \dot{n}_r \\ \frac{dH}{dt} &= \dot{H}_{in} - \dot{H}_{out} + Q - \dot{H}_r \end{aligned} \tag{1.2}$$

The subscript *in* indicates the inlet flow and *out* indicates the outlet flow from the reactors.

The separators, mixers, FT, GT, HRSG, and ST are modelled at steady state conditions, including overall mass and energy balances. The parameter values for the GT, i.e., rotation speed, inlet air flow rate, and isentropic efficiency are obtained from compressor and turbine maps as a general representation of the characteristics. The parameter values for the HRSG and the ST are found from proven design software (Thermoflow Inc., 2011). Dynamic models are developed from the steady state models by including reasonable time constants.

The models are implemented in MATLAB and SIMULINK. Twelve species, i.e., H_2O, CO, CO_2, H_2, CH_4, C_2H_6, C_3H_8, C_4H_{10}, O_2, N_2, Ar, and H_2S, and temperature, flow rate, and pressure in each stream are considered.

The model parameter values are found from literature, steady state models, and communication with experienced researchers.

1.3.2 Control structure design

Previous studies on control structure design for reforming processes and power plants are mainly based on experience rather than on a systematic design procedure. In this study, the control structure design procedure proposed by Skogestad (2004) is used. The control structure design procedure is described in Chapter 3.

1.3.3 Model predictive control

MPC is a well-known advanced technology in process control, and it has been used for many applications since the 1980s. Previous studies and applications show that MPC has several advantages over a conventional controller (Rossiter, 2003). First, MPC is highly attractive for its ability to handle constraints online in a systematic way. For safety and economic reasons, the controller should maintain the variables inside the constraints. Second, MPC may automatically incorporate feedforward control. MPC can hence take action before a disturbance occurs based on the knowledge of future demands. Another major advantage with MPC is that it can handle multivariable systems in a systematic way. This is by using a model that provides information about the interactions from each input on each output. Since the 1980s, thousands of successful applications of MPC have been reported.

Algorithms for MPC can have various forms. A description of the MPC algorithm as used in this work can be found in many books, e.g., Rossiter (2003), and Rawlings and Mayne (2009). The structure of a linear MPC with a state estimator is presented in Figure 1.4. An MPC controller contains a model, cost function, constraints, and an optimiser to calculate the inputs. The Kalman filter (KF) uses the linearized model and measurements to estimate the states. Based on these states a prediction model and constraints on input and output values that track the references are calculated. The MPC controller uses the receding horizon principle. At

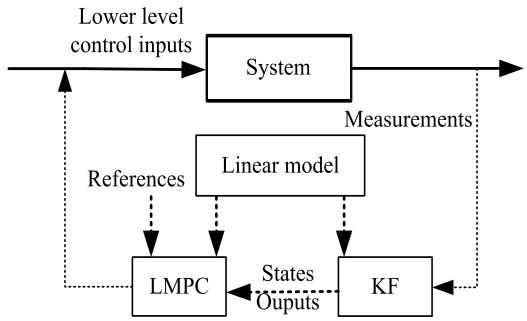

Figure 1.4: The structure of a linear MPC controller with state estimation.

each time step i, the controller receives the measurements, estimates the states, and solves an optimisation problem over a future interval $[i, ..., i + N - 1]$. Generally, only the first step in the resulting optimal control sequence is applied to the real system. This procedure is therefore repeated at the next time step. The output of MPC controllers are typically setpoints to underlying low-level controllers.

1.4 Contributions

The contributions of this thesis are

- New mathematical models of two novel pre-combustion power cycles based on first principles are developed.

- The operating window and optimal operating points of the two power cycles based on economic objectives are found.
- Dynamic behaviours of the critical reactors as well as the whole plants are investigated.
- The control structures of the two power cycles are designed by a systematic approach. Feedback, and feedforward controllers, compensators, and filters are suggested for load changes.
- MPC controllers for selected part of the power cycles are designed to handle important operating constraints.
- A comparison of the HMR and ATR pre-combustion power cycles are made.

1.5 Thesis organization

The remaining part of the thesis is organized as follows

In chapter 2, the HMR pre-combustion power cycle is modelled in detail. Steady state as well as transient analysis is performed. Then, different scenarios are simulated. The simulations are focused on how different process inputs affect important variables in the system, e.g., syngas outlet temperature (SOT), steam to carbon (S/C) ratio, turbine inlet temperature (TIT), GT power, and ST power.

In chapter 3, a control structure for the HMR power cycle is designed. This is made by an economic objective. Further, the design of degree of freedom (DoF) for optimization, and constraints on control inputs and outputs are found. Disturbances are assumed. The system is linearised at a nominal operating point. Next, controlled variables are selected by using self-optimizing control. Finally, the control structures with well-tuned PI controllers and feedforward controllers are simulated and evaluated.

In chapter 4, MPC controllers with state estimation are implemented for the HMR power cycle. Because of the large number of states in the overall system, different sampling times between the process units, and the nonlinearities of the system, a centralised MPC may be not practical. Instead, decentralised MPC combined with PI controllers are used.

In chapter 5, an ATR based pre-combustion gas power cycle has been studied, and dynamic models and the control structure for the system are designed. The ATR power cycle is then used as benchmark for evaluation of dynamic responses and control structures for the HMR power cycle.

In chapter 6, concluding remarks and recommendation for further work are given.

1.6 List of publications

Journal papers

- Zhao L., F. Michelsen, B. Foss, Control design and dynamic simulation of an HMR pre-combustion power cycle based on economic measures, 2012, Energy (submitted for publication)

- Michelsen F. , K. I. Åsen, Ø. Wilhelmsen, L. Zhao, B. Foss, A distributed dynamic model of an HMR reactor, 2011, Energy Conversion and Management (submitted for publication)
- Michelsen F., L. Zhao, B. Foss, Operability analysis and control design of an IRCC cycle HMR unit with membrane leakage, TCCS6, Trondheim, 2011, Energy Procedia (accepted for publication)

Conference papers and presentations

- Zhao L., F. Michelsen, B. Foss, K. Åsen, Dynamic behaviour of an HMR pre-combustion gas power cycle, DYCOPS, 2010
- Zhao L., F. Michelsen, B. Foss, K. Åsen, Control of an HMR Pre-Combustion Gas Power Cycle, presentation at 16th Nordic Process Control Workshop, 2010, Lund, Sweden
- Michelsen F., L. Zhao, B. Foss, Modeling and simulation of HMR pre-combustion gas power cycle, TCCS5, Trondheim, June, 2009
- Michelsen F., B. Foss, L. Zhao, Operability of power plants with CCS, Workshop on operating flexibility of CCS plants, Imperial College London, November, 2009
- Michelsen F., L. Zhao, B. Foss, Operability analysis and control design of an IRCC cycle HMR unit with membrane leakage, TCCS6, Trondheim, June, 2011

Chapter 2

Modelling and simulation of the HMR power cycle

The dynamic model of the HMR power cycle is described in this chapter. First, a literature survey is given. Then, models for each unit are described. In the end, the results from steady state and dynamic simulations are displayed.

2.1 Literature survey

Earlier work on modelling and simulation of similar processes as the HMR power cycle is presented in this section.

Previous studies have investigated modelling and simulation of conventional reactors which use similar materials and have a similar structure as those studied in the thesis.

Bredesen et al. (2004) made a survey of high-temperature membranes and several possible applications of membrane reactors for integration in power generation cycles with CO_2 capture. Performance and limitations of relevant inorganic membranes were presented and discussed. Integrated H_2, O_2 or CO_2 membrane separation was analyzed and it was concluded that development of power plant concepts including membrane technology requires significant degree of optimization in order to identify efficient, feasible and environmentally sound technical solutions. In addition, further development and validation of performance of membranes in real applications were needed.

Chen et al. (2004) investigated catalyst deactivation and reformer performance in a circulating fluidized bed membrane reformer for steam reforming of higher order hydrocarbons using mathematical models. The reactor has a nickel reforming catalyst and palladium based hydrogen selective membranes. A one-dimensional plug-flow reactor model was developed to investigate effects of the operating parameters. The results showed that the reformer had a strong tendency for carbon formation and catalyst deactivation at low steam to carbon (S/C) feed ratios (less than 1:4), for high reaction temperatures ($530°C$) and high pressures ($5bar$). The catalyst activity decreased when S/C feed ratio decreased, reaction temperature increased or reaction pressure increased.

Xu and Froment (1989) derived intrinsic rate equations for the SMR, accompanied by WGS on a $Ni/MgAl_2O_4$ catalyst. A large number of detailed reaction mechanisms were considered. The parameter estimates in the best model were statistically significant and thermodynamically consistent. This model is the most applied reaction model in SMR studies.

Adris et al. (1997) presented a new approach for modelling of a fluidized-bed membrane reactor. They considered the two-phase nature of the fluidized-bed reactor system and the parallel reactions taking place in SMR, as well as selective permeation through the walls of the membrane tubes immersed in the bed. The model is based on a two-phase bubbling bed model with allowance for some gas flow in the dense phase. Plug flow is assumed for the combined sweep gas and the permeating hydrogen through the membrane tubes. Freeboard non-isothermal effects and reactions are also taken into account. The coupled differential equations for the fluidized bed and membrane tubes are solved numerically. The model is in very good agreement with experimental data, both with and without permeation, which were obtained in a pilot-scale reactor system. Parametric investigations demonstrated the effect of key operating variables and design parameters over a wide operating range.

Bose (2008) gave an overview of ceramic membrane technology for H_2 production. The advantages and applications of the membrane were presented.

Matsumura and Tong (2008) studied SMR over a ruthenium catalyst at $500°C$ and 1 - $6bar$ in a membrane reactor equipped with a palladium membrane supported on a porous stainless steel tube. Steam was used as a sweep gas. The results showed that the degree of hydrogen separation was mainly governed by the performance of palladium membrane and the flow rate of sweep gas. Operation at a high reaction pressure was advantageous as this enhanced the catalytic reaction and increased the permeation rate.

Jørgensen et al. (1995) investigated methane reforming in a Pd/Ag membrane reactor. The operational limits for the S/C were discussed. They suggested that the reformer should be operated at a higher S/C (~ 2.9) compared to an ordinary reactor.

Most of the units in the system as studied in this thesis are conventional devices. These devices have been studied extensively in the literatures.

Ampaya and Rinker (1978) did a pseudo-homogeneous mathematical simulation representing the dynamic behavior of an autothermal water gas shift reactor with internal countercurrent flow. The parameters and variables of the model were homogeneous in the radial direction, hence this is a 1 dimensional model. The results showed that a rapidly lumped transient model was useful in displaying the complexity of the reactor response to a feed-temperature perturbation.

Christensen (1996) studied an adiabatic pre-reformer, which converted higher hydrocarbons by SMR reactions in the low temperature range, $350 - 550°C$. Design aspects of adiabatic pre-reforming were reviewed. Reaction kinetics, poisoning, transient deactivation, and limits for carbon formation were formulated mathematically and simulated. A feed purification and selection of operating conditions within the allowed operation window, depending on H_2S/C-ratio and H_2-recycle were suggested.

Sperle et al. (2005) studied pre-reforming of natural gas on a nickel catalyst at 480 - 550°C and 20bar using a tapered element oscillating microbalance reactor. Coking thresholds for feed gas with different S/C ratio at various temperatures were studied.

Lazzaretto and Toffolo (2001) presented a gas turbine design and off-design model by constructing artificial machine maps through appropriate scaling techniques. They applied GT maps which were taken from the literature and validated with test measurement data from real plants. In particular, off-design performance was obtained through compressor map modifications according to variable inlet guide vane closure.

Modelling and simulation of the HMR power cycle as made in this thesis follows a similar structure as documented in the following papers

Stiller et al. (2006) focused on model-based design, operation and control of solid oxide fuel cell (SOFC) and gas turbine hybrid systems. Spatially discretized models were used for the most relevant components, e.g., tubular SOFC, indirect internal reformer, and heat exchangers. For the turbomachinery, map-based steady-state models were used. Gas residence times and pressure drops were considered for all relevant components.

Kandepu et al. (2006) studied a SOFC-GT-based autonomous power system. The first part of that thesis included development of control relevant models of all the components of the SOFC-GT hybrid system using first principles. The SOFC model was tested against a very detailed model and the results showed that the control relevant model captured the dynamics of the process and thus could be used to design a control structure with high performance. Next, a regulatory controller was designed in order for the hybrid system to be able to follow the dynamic load changes while the SOFC temperature is controlled.

Transient behavior of a natural gas-fired power plant for CO_2 capture that incorporates mixed-conducting membranes for integrated air separation was investigated by Eichhorn Colombo et al. (2010). For the turbomachinery components, performance maps were implemented. A multi-scale modelling approach for the time and spatial domains was chosen. Spatially distributed conservation balances for energy, species, and mass were developed for key process components. Performance maps were used for proper off-design performance of the turbomachinery components.

Thorud (2005) also developed a dynamic SOFC/GT model. Calibration and sensitivity of the model was studied. The model was based on a pressurized tubular Siemens Westinghouse-type SOFC, which was integrated in a gas turbine cycle. The process further included a plate-fin recuperator for stack air preheating, a pre-reformer, an anode exhaust gas recycling loop for S/C control, an afterburner and a shell-tube heat exchanger for air preheating. The fuel cell tube, the recuperator and the shell-tube heat exchanger were described by spatially distributed models. The SOFC model was further thermally integrated with the pre-reformer. The compressor and turbine models were based on performance maps. In addition, a shaft model which incorporated moment of inertia was included to account for gas turbine transients.

The above survey shows that

- Different types of SMR reactor models have been developed earlier. The model parameters, e.g., reaction rate coefficients, and permeation rates have been widely studied.
- The novel HMR reactor as studied in this thesis has been designed and studied experimentally, but no dynamic model has been published.
- There exists no dynamic model and analysis of the HMR power cycle. The modelling approach could be similar as previous studies on oxyfuel, SOFC, and ATR pre-combustion power cycles. However, because of the more complicated flow sheet as used in the current study, it makes sense to develop a model to identify important dynamic features and implement control and operability studies on the HMR power cycle.

2.2 Modelling of the HMR power cycle

In this section, the proposed mathematical model is derived. The purpose of this model is to study dynamics, control and ultimately develop an overall robust operational strategy. The model includes sub models for each unit in the HMR power cycle as described in Chapter 1.

2.2.1 Assumptions

The following assumptions are made for all the units

- All gasses are regarded as ideal gasses.
- One-phase flow, i.e., gas only, except units integrated with water evaporation.
- Twelve species, i.e., H_2O, CO, CO_2, H_2, CH_4, C_2H_6, C_3H_8, C_4H_{10}, O_2, N_2, Ar, and H_2S, are considered in each stream.
- Heat capacity, c_p, at constant pressure and calculated from thermodynamic tables (see Appendix A).
- Steady state mass balances.
- Adiabatic conditions.
- Diffusion inside the gas is neglected (Eichhorn Colombo et al., 2010).
- Thermal conduction inside gas is not considered, since this term has no significant effect on temperature (Michelsen et al., 2012).
- Gas pressure drops within all reactors and heat exchangers are neglected (Hagh, 2003).

All the reactors have the following assumptions

- Fixed bed reactors and the reaction rate throughout the catalyst is uniform.
- Assume the internal energy is the dominant contribution and neglect the kinetic and potential energies of the gases.
- The reactors are described by aggregated models, i.e., equal distribution of mass and energy within bounded volumes. This implies that the outlet pressure and temperature equal those within the bounded volume.

- The reactions take place only in bulk gas.

In addition

- Here we only consider an ideal CO_2 split with no pressure drop.
- The gas mixers and splits are ideal processes with no pressure drop.
- Constant overall heat transfer coefficient (U) is used to calculate heat transfer for reactors and heat exchanger channels. Heat exchanger areas (A) are independent parameters, which are used for determining the dynamic response for the model. The heat transfer (Q) is given by

$$Q = AU\Delta T \tag{2.1}$$

  where ΔT is the temperature difference between two sides.

- Compact plate-fin type of heat exchangers is chosen in the model. These are often used in recuperated gas turbine cycles, and the type is suitable for the HMR power cycle according to STATOIL (personal communication, June 8, 2009). A plate-fin heat exchanger is a type of heat exchanger design that uses plates and finned chambers to transfer heat between fluids. It has a relatively high heat transfer surface area to volume ratio.
- The heat exchanger uses a distributed model and is discretized into n sections along the heat exchanger.
- The heat exchangers have even pressure and mass distribution along the heat exchanger.
- The reactors of pre-reformer and HMR are discretized into n cells along the reactor, see Figure 2.1 where each cell is an aggregated model.

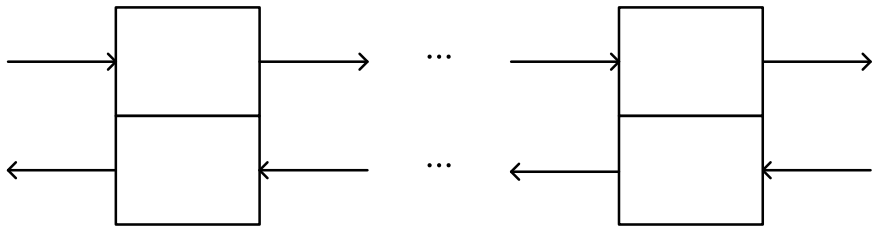

Figure 2.1: Aggregated cell model.

- The membrane in the HMR reactor has 100% selectivity for hydrogen (Adhikari and Fernando, 2006).
- Steady state assumption is made for the flash tank which condensates and removes steam from the mixed gas. The content of vapour and water are calculated from functions by the Antoines equation and the Rachford-Rice equation (Whitson and Michelsen, 1989).
- The reaction rate (r_j) of SMR is calculated from Xu and Froment (1989) as (2.2).

$$r_j = A_2 R_j V \rho, j = 4, 5, 6 \tag{2.2}$$

$$R_4 = \frac{k_{1,SMR}}{p_{H_2}^{2.5}} \frac{p_{CH_4} p_{H_2O} - p_{H_2}^3 p_{CO} / K_{1,SMR}}{DEN^2}$$

$$R_5 = \frac{k_{2,SMR}}{p_{H_2}} \frac{p_{CO} p_{H_2O} - p_{H_2} p_{CO_2} / K_{2,SMR}}{DEN^2}$$

$$R_6 = \frac{k_{3,SMR}}{p_{H_2}^{3.5}} \frac{p_{CH_4} p_{H_2O}^2 - p_{H_2}^4 p_{CO_2} / K_{3,SMR}}{DEN^2}$$

$$DEN = 1 + K_{CO,SMR} p_{CO} + K_{H_2O,SMR} p_{H_2O} / p_{H_2} + K_{H_2,SMR} p_{H_2} + K_{CH_4,SMR} p_{CH_4}$$

where p are partial pressures, k and K are given by Arrhenius equations, A_2 the surface area, V the reactor volume, and ρ the catalyst density.

- The hydrogen combustion in the HMR reactor and combustion in the CC are totally converted and always in equilibrium (Hagh, 2003). The reaction rate of hydrogen combustion ($r_{s,j}$) is

$$r_{s,j} = K_c p_{H_2,s} p_{O_2,s} \tag{2.3}$$
$$K_c = k_c e^{(-\frac{E_c}{RT_s})}$$

- The permeation rate is calculated by (2.4) which is provided by STATOIL (STATOIL, 2008)

$$r_p = k_{m,t} \frac{Q_H}{d_m} \left[\frac{1}{k_H \sqrt{p_{H_2}} + 1} - \frac{1}{k_H \sqrt{p_{H_2,s}} + 1} \right] \tag{2.4}$$

Here, $p_{H_2}, p_{H_2,p}$ are partial pressures at the retentate side and permeate side of the reformer,and l_m is the membrane thickness. The permeability of hydrogen Q_H and the constant k_H depend on the temperature by the Arrhenius coefficients. $k_{m,t}$ is used to tune the permeation rate.

- The reaction rate models of the LTWGS and MTWGS are from Richards (2006)

$$r_j = A_j R_j V_j \rho_j \tag{2.5}$$
$$R_j = k_1 P_{CO} P_{H_2O} - k_2 P_{CO_2} P_{H_2} \tag{2.6}$$

- The reactions of heavier hydrocarbons (C_2H_6, C_3H_8, C_4H_{10}) are totally converted in a pre-reformer (Christensen, 1996), and the reaction rate is calculated as

$$r_j = \dot{n}_{i,in}, i = [\ C_2H_6 \quad C_3H_8 \quad C_4H_{10}\ ], j = 1, 2, 3 \tag{2.7}$$

- Temperatures at the cooling side of MTWGS and HE5 are kept constant at $237°C$, which is the saturation temperature at $32bar$.
- The HRSG and ST are simulated in GTPro/GTMaster. Algebraic equations are used to fit the data from different simulation scenarios.

Assumptions for GT model are (Bolland, 2009)

- The gas turbine model is based on experimental maps due to computational simplicity. Further, it has the ability to deal with plants having large variations in the operating parameters. Generalized maps of the machines are taken from Lazzaretto and Toffolo (2001)
- Gas residence time is negligible.
- Fouling and degradation are negligible.
- The kinetic energy of the gas is negligible compared to the enthalpy.
- A variation in the inlet flow angle by the variable inlet guiding vanes (VIGV) results in a modification of the characteristic curves for the compressor. A simple model can be used to calculate the variation for compressor work (W_{CV}), pressure ratio (π_{CV}) and isentropic efficiency (η_{CV}). This is expressed by (2.8)

$$\begin{aligned} W_{CV} &= W_C(1 + \frac{C_1 \triangle\alpha}{100}) \\ (\pi_{CV} - 1) &= (\pi_C - 1)(1 + \frac{C_2 \triangle\alpha}{100}) \\ \eta_{CV} &= \eta_C(1 - \frac{C_3 \triangle\alpha^2}{100}) \end{aligned} \tag{2.8}$$

  Here C_1, C_2 and C_3 are constants. $\triangle\alpha$ is the angle. The mass flow and pressure ratio follow a linear relationship and efficiency follows a quadratic relationship versus guide vane angle (Kurzke, 1996).

2.2.2 Models

Heat exchanger

The heat exchanger model is a one-dimensional distributed model. It describes a dynamic energy balance for each stream. By this, the temperature profiles along the heat exchanger for the gas in each stream are calculated.

Mass balances

Steady state mass balance along the reactor means that the inlet mass flow always equals to the outlet mass flow.

$$\dot{m}_{in} = \dot{m}_{out} \tag{2.9}$$

Energy balances

By considering convection and heat transfer between cold and hot fluids, the dynamic models for temperature T are given by

$$\sum_i c_{p,i} m_i \left(\frac{\partial T}{\partial t} + v \frac{\partial T}{\partial z} \right) = Q \tag{2.10}$$

where

$$\begin{aligned} m &= \rho V \\ \rho &= \frac{p}{RT}\sum_i M_i\lambda_i \\ V &= \frac{1}{2}AR_s \end{aligned} \tag{2.11}$$

Here i denotes each component in the stream, m is the total fluid mass inside the reactor, v is the velocity of fluid, ρ the total density of the fluid, V the total volume, R the universal gas constant, λ the molar fraction of each component, p the pressure, M the molar mass, A the contact area, R_s the equivalent height of a fin.

HE5

For the heat exchangers including water evaporation, the following models are used

Mass balances

Component balances for heat exchangers with evaporation are

$$\begin{aligned} \frac{dn_{hg,i}}{dt} &= \dot{n}_{hg,i,in} - \dot{n}_{hg,i,out} \\ \frac{dn_{cg,i}}{dt} &= \dot{n}_{cg,i,in} + \dot{n}_{cg,i,r} - \dot{n}_{cg,i,out} \\ \dot{n}_{cg,Steam,r} &= (Q - E_S)/H_S \\ \dot{n}_{cg,Water,r} &= -(Q - E_S)/H_S \end{aligned} \tag{2.12}$$

Here, i denotes the steam and liquid water components, n moles, subscript cg cold gas, hg hot gas, $\dot{n}_r$ is the molar rate of water that is vaporized, T_S the saturation temperature, E_S the heat to raise the temperature to vaporization temperature, H_S the enthalpy for vaporization, and $\dot{n}_{i,out}$ is the mole rate of component leaving the reformer, which is given by

$$\dot{n}_{i,out} = \frac{\lambda_i}{\sum_i \lambda_i M}\sum_i (\dot{n}_{i,in}M + \dot{n}_{i,r}M) \tag{2.13}$$

Energy balance

Aggregated energy balances including convection and heat transfer between hot and cold gases are described by

$$\sum_i n_{hg,i}c_{phg,i}\frac{dT_{hg}}{dt} = \sum_i \dot{n}_{hg,i,in}c_{phg,i,in}T_{hg,in} - \sum_i \dot{n}_{hg,i,in}c_{phg,i}T_{hg} + Q \tag{2.14}$$

$$\sum_i n_{cg,i}c_{pcg,i}\frac{dT_{cg}}{dt} = \sum_i \dot{n}_{cg,i,in}c_{pcg,i,in}T_{cg,in} - \sum_i \dot{n}_{cg,i,in}c_{pcg,i}T_s - Q \tag{2.15}$$

If the heat transfer from hot gas to water is less than the energy needed to raise the water temperature to vaporization temperature, (2.15) is used. Otherwise temperature is constant and the heat is used to generate steam (2.14).

Pre-reformer

The model of a pre-reformer is described by cell models. For each cell, the models are given by

Mass balances

The species balances for each cell are given by

$$\begin{aligned} \frac{dn_{p,i}}{dt} &= \dot{n}_{p,i,in} - \dot{n}_{p,i,out} + \dot{n}_{p,i,r} \\ \dot{n}_{hg,i,in} &= \dot{n}_{hg,i,out} \end{aligned} \tag{2.16}$$

Subscript p means process gas.

The overall mass balance is given by

$$\dot{m}_{in} - \dot{m}_{out} = 0 \tag{2.17}$$

Then, the outlet molar flow rate can be calculated by

$$\dot{n}_{in} \sum_i \lambda_{i,in} M_i = \dot{n}_{out} \sum_i \lambda_{i,out} M_i \tag{2.18}$$

where $\dot{n}_{i,r}$, the mole rate of component reacted in the reformer, are given by

$$\dot{n}_{i,r} = \sum_j^m C_{r,ij} r_j \tag{2.19}$$

C_r are stoichiometric coefficients. r_j are the reaction rates of the m reactions that take place.

Energy balances

By including heat of convection, conduction and reaction, the temperatures T are given by

$$\sum_i n_{p,i} c_{pp,i} \frac{dT_p}{dt} = \sum_i \dot{n}_{p,i,in} c_{pp,i,in} T_{in} - \sum_i \dot{n}_{p,i,in} c_{pp,i} T + Q - \sum_j r_j \Delta H_{r,j} \tag{2.20}$$

$$\sum_i n_{hg,i} c_{phg,i} \frac{dT_{hg}}{dt} = \sum_i \dot{n}_{hg,i,in} c_{phg,i,in} T_{hg,in} - \sum_i \dot{n}_{hg,i,in} c_{phg,i} T_{hg} - Q$$

The heat of reactions of the six reactions are given by

$$\Delta H_j = \sum_i C_{rij} H_i, j = 1...6 \tag{2.21}$$

H_i is the enthalpy.

HMR

The model for each channel of HMR reactor is given by

Mass balances

Each channel is described by aggregated models

$$\begin{aligned}\frac{dn_{p,i}}{dt} &= \dot{n}_{p,i,in} - \dot{n}_{p,i,r} - \dot{n}_{p,i,out} - \dot{n}_{H_2,perm} \\ \frac{dn_{s,i}}{dt} &= \dot{n}_{s,i,in} - \dot{n}_{s,i,r} - \dot{n}_{s,i,out} + \dot{n}_{H_2,perm}\end{aligned} \tag{2.22}$$

Subscript p is the process side of the reactor, and s is the sweep gas side of the reactor. $\dot{n}_{H_2,perm}$ is the molar flow rate of permeated H_2 through the membrane.

The overall mass balances are described by

$$\begin{aligned}\dot{m}_{in,s} - \dot{m}_{out,s} - \dot{m}_{perm} &= 0 \\ \dot{m}_{in,p} - \dot{m}_{out,p} + \dot{m}_{perm} &= 0\end{aligned} \tag{2.23}$$

The outlet molar flow rate for each channel is calculated by

$$\dot{n}_{in}\sum_i \lambda_{i,in} M_i = \dot{n}_{out}\sum_i \lambda_{i,out} M_i + \dot{n}_{perm} M_{H_2} \tag{2.24}$$

$$\dot{n}_{out} = \frac{\dot{n}_{in}\sum_i \lambda_{i,in} M_i - \dot{n}_{perm} M_{H_2}}{\sum_i \lambda_{i,out} M_i}$$

The molar changes caused by steam reforming are calculated similarly as for the pre-reformer as described in the previous section

$$\dot{n}_{i,r} = \sum_j^m C_{rij} r_j \tag{2.25}$$

Energy balances

The temperatures T_p and T_s are given by

$$\begin{aligned}\sum_i n_{p,i} c_{pp,i} \frac{dT_p}{dt} &= \sum_i \dot{n}_{p,i,in} c_{pp,i,in} T_{p,in} - \sum_i \dot{n}_{p,i,in} c_{pp,i} T_p + Q - \sum_j r_j \Delta H_{r,j} \\ \sum_i n_{s,i} c_{ps,i} \frac{dT_s}{dt} &= \sum_i \dot{n}_{s,i,in} c_{ps,i,in} T_{s,in} - \sum_i \dot{n}_{s,i,in} c_{ps,i} T_s - Q - \sum_j r_{s,j} \Delta H_{r,s,j}\end{aligned} \tag{2.26}$$

MTWGS and LTWGS

The models for MTWGS and LTWGS are described below

Mass balances

The species balances in the MTWGS are

$$\begin{aligned} \frac{dn_i}{dt} &= \dot{n}_{i,in} - \dot{n}_{i,out} + \dot{n}_{i,r} \\ \frac{dn_{cg,j}}{dt} &= \dot{n}_{cg,j,in} + \dot{n}_{cg,j,r} - \dot{n}_{cg,j,out} \\ \dot{n}_{cg,Steam,r} &= (Q - E_S)/H_S \\ \dot{n}_{cg,Water,r} &= -(Q - E_S)/H_S \end{aligned} \tag{2.27}$$

The subscript j denotes the steam and water in the reactor.

The species balances in the LTWGS are

$$\frac{dn_i}{dt} = \dot{n}_{i,in} - \dot{n}_{i,out} + \dot{n}_{i,r} \tag{2.28}$$

With the constant overall mass balance

$$\begin{aligned} \dot{m}_{in} - \dot{m}_{out} &= 0 \\ \dot{n}_{in}\sum_i \lambda_{i,in} M_i &= \dot{n}_{out}\sum_i \lambda_{i,out} M_i \end{aligned} \tag{2.29}$$

The molar changes by shift reactions are given by

$$\dot{n}_{i,r} = \sum_j^m C_{rij} r_j \tag{2.30}$$

Energy balances

The outlet temperatures T of the MTWGS are given by

$$\sum_i n_i c_{pi} \frac{dT}{dt} = \sum_i n_{i,in} c_{pi,in} T_{in} - \sum_i n_{i,in} c_{pi} T + Q + \sum_j r_j \Delta H_{r,j} \tag{2.31}$$

$$\sum_i n_{cg,j} c_{pcg,j} \frac{dT_{cg}}{dt} = \sum_i n_{cg,j,in} c_{pcg,j,in} T_{cg,in} - \sum_i n_{cg,j,in} c_{pcg,j} T_{cg} - Q + E_{cg}$$

while the temperature for the LTWGS is

$$\sum_i n_i c_{pi} \frac{dT}{dt} = \sum_i n_{i,in} c_{pi,in} T_{in} - \sum_i n_{i,in} c_{pi} T + Q + \sum_j r_j \Delta H_{r,j} \tag{2.32}$$

Gas turbine

The GT includes air compressors, gas expanders, and a shaft. The models of compressors and expanders use steady state models, while the model for the shaft is given by the momentary balance.

Model equations

The high pressure compressor map has the following parameters

- Reduced flow rate, expressed as a corrected flow rate $\dot{m}_{red}$ or non-dimensional flow rate $\dot{m}_{red,dl}$. As opposed to the real flow rate $\dot{m}$, $\dot{m}_{red,ds}$ is the designed reduced mass flow rate.

$$\begin{aligned} \dot{m}_{red} &= \frac{\dot{m}\sqrt{T_{in}}}{p_{in}} \\ \dot{m}_{red,dl} &= \frac{\dot{m}_{red}}{\dot{m}_{red,ds}} \end{aligned} \tag{2.33}$$

- Pressure ratio

$$\begin{aligned} \pi &= \frac{p_{out}}{p_{in}} \\ \pi_{red,dl} &= \frac{\pi_{red}}{\pi_{red,ds}} \end{aligned} \tag{2.34}$$

  $\pi_{red,dl}$ is the non-dimensional ratio, and $\pi_{red,ds}$ is the design ratio.

- Constant rotational corrected speed lines

$$\begin{aligned} N_{red} &= \frac{N}{\sqrt{T_{in}}} \\ N_{red,dl} &= \frac{N_{red}}{N_{red,ds}} \end{aligned} \tag{2.35}$$

  $N_{red,dl}$ is the non-dimensional corrected speed, and $N_{red,ds}$ is the designed corrected speed.

  The speed lines are near vertical, for the lines close up rapidly, due to choking. Beyond choke, any further increase in speed will generate no further increase in air flow.

- Efficiency η
- Surge line Above this line there is a region of unstable flow, which should be avoided.

The performance map for the modelled radial compressor is shown in Figure 2.2 .

The maps in Figure 2.2 cannot be directly used in a simulation program for two main reasons

1. Some of the constant reduced speed lines are almost vertical. This is due to the compressor operating in a choked condition.
2. For low values of rotation speed and assigned value of the pressure ratio, two values of m_{in}, T_{in}, and p_{in} may exist.

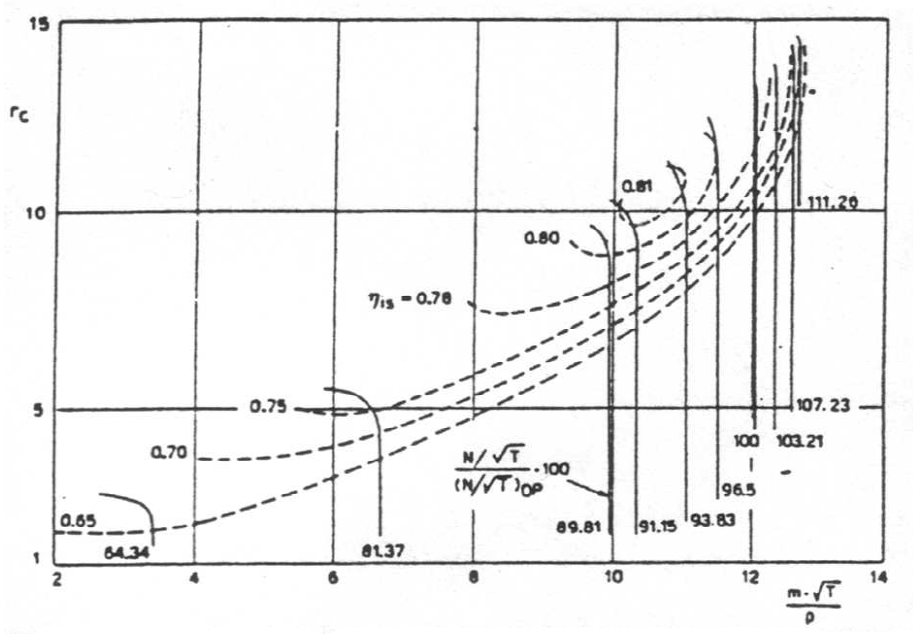

Figure 2.2: Compressor map (Kurzke, 1996).

These problems are overcome by introducing auxiliary coordinates (also called β line), which has no direct physical meaning. These lines are used to parameterize all the constant speed curves through a monotonic parameter β ranging from 0 to 1. Equally spaced parabolic lines are chosen here. In this way, for given values of N, T_{in}, and β, the values of m_{in}, T_{in}, p_{in}, π_{comp}, and η_{comp} remain determined (Kurzke, 1996; Mirandola, 1986) .

Dimensionless variables are calculated by

$$\begin{aligned} \dot{m}_{red,dl} &= \frac{f_1(N_{red,dl}, \beta)}{\dot{m}_{red,0}} \\ \eta_{isen,dl} &= f_2(N_{red,dl}, \beta) \\ \pi_{dl} &= \frac{f_3(N_{red,dl}, \beta)}{\pi_0} \\ \pi_{surge} &= f_4(\dot{m}_{red,dl}) \end{aligned} \tag{2.36}$$

Here $\dot{m}_{red,0}$ and π_0 are nominal values. f_1, f_2, f_3, and f_4 are polynomial functions generated from the compressor map, see (Stiller, 2006) for more details on this.

The outlet temperature and compressor work are found by solving the following

equations

$$\begin{aligned}
\dot{m}_{in} &= \dot{m}_{out} + \dot{m}_{out,extr} \qquad (2.37)\\
s(T_{isen,out}, p_{out}, \lambda_{out}) - s(T_{in}, p_{in}, \lambda_{in}) &= 0\\
s(T_{extr,isen,out}, p_{extr,out}, \lambda_{extr,out}) - s(T_{in}, p_{in}, \lambda_{in}) &= 0\\
h(T_{isen,out}, p_{out}, \lambda_{out}) - h(T_{in}, p_{in}, \lambda_{in}) &= \triangle H_{isen}\\
h(T_{extr,isen,out}, p_{extr,out}, \lambda_{extr,out}) - h(T_{in}, p_{in}, \lambda_{in}) &= \triangle H_{isen,extr}\\
\triangle H &= \frac{\triangle H_{isen}}{\eta_{isen}}\\
\triangle H_{extr} &= \frac{\triangle H_{isen,extr}}{\eta_{isen}}\\
W_{comp} &= \dot{m}_{out}\triangle H + \dot{m}_{out,extr}\triangle H_{extr}
\end{aligned}$$

Here, function s is used to calculate the entropy and h enthalpy.

The isentropic efficiency η_{isen} for a compression process is defined as the ratio between the isentropic work and the actual work. T_{extr}, and P_{extr} are the temperature and pressure in the air that is extracted to the HMR reactor, and assume P_{extr} is constant.

Solve T_{out}, and $T_{out,extr}$ from

$$\begin{aligned}
h(T_{out}, p_{out}, \lambda_{out}) - h(T_{in}, p_{in}, \lambda_{in}) &= \triangle H \qquad (2.38)\\
h(T_{out,extr}, p_{out,extr}, \lambda_{extr,out}) - h(T_{in}, p_{in}, \lambda_{in}) &= \triangle H_{extr}
\end{aligned}$$

The expander is assumed to be a chocked nozzle. Based on the chocked nozzle assumption the expander work can be calculated from the mechanical efficiency, enthalpy change and the mass balance (2.39).

$$\begin{aligned}
\dot{m}_{in,T} &= \dot{m}_{out,T} \qquad (2.39)\\
s(T_{isen,out,T}, p_{out,T}, \lambda_{out,T}) - s(T_{in,T}, p_{in,T}, \lambda_{in,T}) &= 0\\
h(T_{isen,out,T}, p_{out,T}, \lambda_{out,T}) - h(T_{in,T}, p_{in,T}, \lambda_{in,T}) &= \triangle H_{isen}\\
\triangle H_T &= \eta_{T,isen}\triangle H_{T,isen}\\
W_T &= \eta_{m,T}\dot{m,}T\triangle H_T
\end{aligned}$$

Here, the isentropic efficiency for a expansion process is defined as the ratio between actual work and isentropic work.

The angular acceleration due to excess shaft power is expressed by (2.40) by assuming that the shaft can be described as a rotating disc with radius l_{shaft} and mass m_{shaft}.

$$\begin{aligned}
\frac{d\omega}{dt} &= \frac{\triangle P}{I_{shaft}\omega} \qquad (2.40)\\
\triangle P &= P_T - W_C - W_L
\end{aligned}$$

The inertia of a rotating disc is calculated by (2.41).

$$I_{shaft} = \frac{m_{shaft} l_{shaft}^2}{2} \qquad (2.41)$$

Combustion chamber

High pressure air and fuel are fed into the combustion chamber. All the combustible gas, e.g., H_2 and small portion of CO and CH_4, are combusted. The released energy is used for turbine expansion. The models are given by

Mass balances

The species balances are expressed similarly as for previous sections

$$\frac{dn_i}{dt} = \dot{n}_{i,in} - \dot{n}_{i,out} + \dot{n}_{i,r} \tag{2.42}$$

The molar flow changes by reaction are calculated by

$$\dot{n}_{i,r} = \sum_j C_{rij} r_j \tag{2.43}$$
$$r_j = \dot{n}_{i,in}, i = H_2, CH_4, CO$$

The overall steady state mass balance is described as

$$\dot{m}_{in} - \dot{m}_{out} = 0 \tag{2.44}$$
$$\dot{n}_{in} \sum_i \lambda_{i,in} M_i = \dot{n}_{out} \sum_i \lambda_{i,out} M_i$$

Energy balance

The outlet temperature is calculated by

$$\sum_i n_i c_{p,i} \frac{dT}{dt} = \sum_i n_{i,in} c_{pi,in} T_{in} - \sum_i n_{i,in} c_{p,i} T + \sum_j r_j \Delta H_{r,j} \tag{2.45}$$

Split and mixer

The models for splits and mixers are considered to be ideal with no pressure drop.

Mass balances

By assuming no pressure drop, p_{out} is given by the inlet pressures, which are calculated to be equal for consistency. The outlet flow rate w_{out}, composition λ_{out} and temperature T_{out} are calculated by steady state mass and energy balances by considering convection only.

Species balances for the splits are given by

$$\dot{n}_{i,in} = \dot{n}_{i,out,1} + \dot{n}_{i,out,2} \tag{2.46}$$

For the mixers

$$\dot{n}_{i,in,1} + \dot{n}_{i,in,2} = \dot{n}_{i,out} \tag{2.47}$$

And for an ideal CO_2 split

$$\dot{n}_{i,in} = \dot{n}_{i,out,1} + \dot{n}_{CO_2,out,2} \tag{2.48}$$
$$\dot{n}_{CO_2,out,2} = r_{CO_2} \dot{n}_{CO_2,in}$$

The split rate for CO_2, r_{CO_2}, is constant.

Energy balances

The energy balance for the split is expressed by

$$\dot{n}_{i,in,1}h_{in,1}(T_{in,1}) + \dot{n}_{i,in,2}h_{in,2}(T_{in,2}) = \dot{n}_{i,out}h_{out}(T_{out}) \tag{2.49}$$

Likewise for the mixers

$$\dot{n}_{i,in}h_{in}(T_{in,1}) = \dot{n}_{i,out,1}h_{out,1}(T_{out,1}) + \dot{n}_{i,out,2}h_{out,2}(T_{out,2}) \tag{2.50}$$

Flash tank

The flash tank is designed to separate a mixture of gases by utilizing the difference in the boiling point temperatures of the gas components. The steady state models are

Steady state model

Partial pressure is calculated by the Antoines equation with coefficient from literature (Richards, 2006)

$$p_i = e^{(C_1+C_2/(T+C_3)+C_4ln(T)+C_5T^{C_6})} \times 10^{-2} \tag{2.51}$$

The fraction of feed that is vaporized α_v can be calculated from Rachford-Rice equation

$$\sum_i \frac{\lambda_{i,in}(I-\pi_i)}{\alpha_v + (1-\alpha_v)\pi_i} = 0 \tag{2.52}$$
$$\pi_i = \frac{p_i}{p_{tot}}$$

The liquid mole fraction γ_l and vapour mole fraction γ_v in the reactor are

$$\gamma_l = \frac{\lambda_{in}}{(\alpha_v + (1-\alpha_v)\pi)} \tag{2.53}$$
$$\gamma_v = k\gamma_l$$

Vapour and liquid outflow rates are given by

$$\dot{n}_{vap} = (I-\alpha_v)\dot{n}_{in} \tag{2.54}$$
$$\dot{n}_{liq} = \alpha_v\dot{n}_{in}$$

Heat recovery steam generation and steam turbine

An HRSG is an energy recovery heat exchanger that recovers heat from a hot gas. The HRSG produces steam to drive steam turbines. The HRSG and STs have relatively complicated structures and slow dynamics. Algebraic equations with two time constants can be used to represent the dynamics of the HRSG. This kind of model has been studied by several authors, e.g., de Mello et al. (1994), Zhang and So (2000), and Mantzaris and Vournas (2007).

Model

The total power generated by the steam turbines P_{ST}, the temperature of the extracted steam T_{extr}, and the pressure of the extracted steam p_{extr} are calculated by

$$\begin{aligned} P_{ST} &= P_{ST,ds}\,(1 + P_{ST,dl}) \\ T_{extr} &= T_{extr,ds}\,(1 + T_{extr,dl}) \\ p_{extr} &= p_{extr,ds}\,(1 + p_{extr,dl}) \end{aligned} \tag{2.55}$$

The scaled P_{ST}, T_{extr}, and p_{extr} are calculated from polynomial functions by

$$\begin{aligned} P_{ST,dl} &= f_1(\dot{n}_{extr,dl}, H_{GT,out,dl}) \\ T_{extr,dl} &= f_2(\dot{n}_{extr,dl}, H_{GT,out,dl}) \\ p_{extr,dl} &= f_3(\dot{n}_{extr,dl}, H_{GT,out,dl}) \end{aligned} \tag{2.56}$$

Here, f_1, f_2, and f_3 are polynomial functions which are estimated from GT-Pro/GTMaster and have the following form

$$f_i = C_1 x_1 + C_2 x_2 + C_3 x_1 x_2 + C_4 x_1^2 + C_5 x_2^2 \tag{2.57}$$

$\dot{n}_{extr,dl}$ and $h_{GT,out,dl}$ are the scaled extracted steam flow rate and scaled enthalpy of exhausted gas from GTs, expressed by

$$\begin{aligned} \dot{n}_{extr,dl} &= \frac{\dot{n}_{extr} - \dot{n}_{extr,ds}}{\dot{n}_{extr,ds}} \\ H_{GT,out,dl} &= \frac{H_{GT,out} - H_{GT,out,ds}}{H_{GT,out,ds}} \end{aligned} \tag{2.58}$$

A two time constant model is used to represent the dynamics of the HRSG (de Mello et al., 1994).

$$G_{HRSG} = \frac{1}{(1 + t_{HRSG1}s)\,(1 + t_{HRSG2}s)} \tag{2.59}$$

Miscellaneous relations

The carbon content of one stream is calculated as

$$n_C = \dot{n}(\lambda_{CO} + \lambda_{CO_2} + \lambda_{CH4} + 2\lambda_{C_2} + 3\lambda_{C_3} + 4\lambda_{C_4}) \tag{2.60}$$

The captured CO_2 rate is the ratio of captured CO_2 to the carbon content in NG plus the carbon content of the fuel from the buffer tank, expressed by

$$C_{CO_2} = \frac{C_{S19\_1}}{C_{S26} + C_{S24}} \tag{2.61}$$

The net power output is the difference of GT and STs produced power and the power consumed by the process. This is expressed by

$$P_{net} = P_{GT} + P_{ST} - W_{AC} - W_{CO_2C} \tag{2.62}$$

W_{AC} is the power consumed by the air compressor and W_{CO_2C} is the power used to compress the captured CO_2.

The efficiency is the net power output divided by a low heat value (LHV) of inlet fuel, H_{S26}, and H_{S24}.

$$\eta_{LHV} = \frac{P_{net}}{H_{S26} + H_{S24}} \tag{2.63}$$

The pressure ratio and isentropic efficiency for the air and CO_2 compressors are assumed to be constant. The outlet temperatures from these compressors are

$$T_{out} = T_{in}\left(1 + \frac{\pi^{\frac{\gamma-1}{\gamma}} - 1}{\eta_{isen}}\right) \tag{2.64}$$

where γ is the heat capacity ratio.

The required power by the compressors are

$$P = (H_{out} - H_{in})\dot{n} \tag{2.65}$$

2.3 Simulation results

This section presents the simulation results of the dynamic model for the HMR power cycle. The parameter values can be found from Appendix B. Evaluation of each process unit by an Aspen model is described in Appendix C. Further, this Appendix provides more information on the implementation including numerical solvers.

2.3.1 Steady state behavior of the HMR power cycle

Comparison between some important variables for the Aspen and SIMULINK models are shown in Table 2.1 and Table 2.2. The maximum difference is 2.8% at outlet temperature for the pre-reformer, T_{S8}. The differences are mainly caused by different GT, HRSG, and ST models, and different model structures as described in Appendix C. The results indicate that the model errors are below 3% which is relatively small. Further, this study is mainly focus on dynamic responses. Hence, the SIMULINK model is suitable for the current study.

Table 2.1: Steady state results from SIMULINK model and Aspen model.

Variable [$^{\circ}C$]	Simulink	Aspen plus	Difference	%
T_{S3}	336.1	332.5	−3.6	1.1
T_{S4}	585.0	582.8	−2.2	0.4
T_{S5}	757.6	750.0	−7.6	1.0
T_{S6}	1070.9	1063.9	−7.0	0.7
T_{S18}	743.3	750.0	6.7	0.9
T_{S7}	874.6	877.6	3.0	0.3
T_{S8}	442.0	430.0	−12.0	2.8
T_{S9}	344.7	342.1	−2.6	0.8
T_{S11}	250.2	250.0	−0.2	0.1
T_{S12}	202.1	202.0	−0.1	0.0
T_{S16}	25	25	0	0
T_{S29}	731.0	732.3	1.2	0.2
T_{S23}	428.3	438.1	9.8	2.2
T_{S25}	1393.1	1400.6	7.6	0.5
T_{S62}	283.8	290.0	6.2	2.1

Table 2.2: Results from SIMULINK model and Aspen model, combined cycle.

Variable [MW]	Simulink	Aspen plus	Difference	%
Load	390	397.9	7.9	2.0
Compressor	263.0	260.8	2.2	0.8
Expander	551.3	556.0	4.7	0.8
Power generation	410.3	416.4	6.1	1.5
LHV(NG)	790.88	790.88	–	0
Gross efficiency	51.88%	52.65%	0.77%	1.5

2.3.2 Dynamic behavior of the HMR power cycle

Figure 2.3 - 2.7 show some important dynamic behavior. A 10% step change is made in input variables at 100% and 60% load. At 100% load the input is changed in both directions. These step changes are performed for analysis of the dynamic response of the system, and they are done with a minimum of control. Two control loops, however, must be included to secure stable performance. These control the shaft speed of the GT and the vapor quality of MTWGS. Single loop PI controllers are used for these control loops.

Figure 2.3 shows the responses from 10% step changes of the NG flow rate when all the other inputs are constant. Changes in the NG flow rate give

- Small disturbance on the rotation speed. The rotation speed is driven back to the setpoint fast, because of the large gains of the PI controller and the usage of the buffer tank. The dynamic responses are approximate linear.
- Less than 1% change in the TIT and GT power due to changes in the power consumption by the process. The power consumption by the process is mainly affected by the air compressor and the CO_2 compressor. Here, a reduced NG

flow rate results in less amount of captured CO_2 and less power consumption by the CO_2 compressor, despite the capture rate is increased. The dynamics are first influenced by rotation speed. Then, it is slowly varied following the power by the ST and the process. Nonlinearities are observed, for the power by the ST is changed at 60% load, while the power is constant at 100% load.

- Slowly varied SOT. A reduced NG flow rate results in less reforming reactions in the reformers. The time constant is large because of the large mass of the catalyst. The dynamics are approximately linear.
- Similar responses in the S/C ratio as in the CO_2 capture rate. A reduced NG flow rate gives an increased S/C ratio and CO_2 capture rate. This is because of the less amount of hydrocarbons to the reformers and the higher SOT which give higher conversion of methane to H_2. There are mainly three time constants. One instant changes due to the NG flow rate change. Then, the dynamics are mainly affected by the reaction rate changes because of the concentration changes. In the end, the values are slowly varied due to the slow temperature changes which also influence the reaction rates. The responses at 100% load has a smaller gain than at 60%. Thus they are nonlinear. The nonlinearities are mainly caused by the different conversion rate for reformers at different inlet flow rates.
- No changes of the power by the ST at 100% load. The ST and HRSG models are affected by the inlet enthalpy, and the flow rate and temperature of extracted steam to the process. At 100% load, the design values for power output of the ST are the same as the maximum values. This means that, at this operating point, any increase of the inlet enthalpy or decrease of the extracted steam flow cannot increase the power output. Further, the flow rate for extracted steam is lower than the design value. This gives some back-off before the outlet power of the ST decreases. At 60% load, the outlet power is not at the maximum value, thus it is free to vary. The dynamics are first influenced by the instant NG low rate changes, then they are slowly varied due to the two time constants for the HRSG and ST model.

Figure 2.4 shows the responses from 10% step changes of the air flow rate when all the other inputs are constant. A reduced extracted air flow rate gives

- Surplus of the fuel from the buffer tank because of the less power consumptions and the less power production by the GT. The dynamics are nonlinear at different load. This is caused by the nonlinear behavior of the rotation speed. The nonlinearities of the rotation speed is due to the combined effects of the GT power, the ST power and the power consumptions in the process.
- Less power is required by the air compressor and the CO_2 compressor. Thus the power consumed by the process is reduced. The response is approximately linear.
- Less GT power output despite a higher TIT. The air flow is extracted from the GT, less extraction means more compressor work is required. To compensate the increased compressor work, a higher temperature is required for the expander, thus TIT is increased. The steady state response of the GT power

is opposite for 60% load compared to 100% load. This is due to the changes of the power by the ST at 60% load.

- Lower values of the SOT, the S/C ratio and the captured CO_2 rate. Less H_2 is combusted in the HMR because of the reduced air flow rate, despite less air could increase SOT due to less cooling on the air side of the HMR reactor. A decreased SOT results in decreased SMR reactions, thus the S/C ratio and the captured CO_2 rate are reduced. The time constants of the SOT and S/C are large, for the temperature dominates the dynamics of these two variables. The inverse responses on the captured CO_2 rate are the combined effects of fast flow rate and slow temperature changes.

Figure 2.5 shows the responses from 10% step changes of the steam flow rate when all the other inputs are constant. An increase of the extracted steam flow rate from the steam turbine gives

- An increased S/C and captured CO_2 rate, and a slightly decreased SOT, because the increased steam to the HMR results in a higher methane conversion. The change in the SOT is less significant than the change from the air flow rate. The nonlinear behaviours are mainly caused by the nonlinearities of the reforming reactors.
- The steam is extracted from the ST, thus the power by the ST is directly affected by the extracted flow rate. The gain at 100% load is much smaller than the gain at 60% because of the nonlinear HRSG and ST model. With the same amount of steam extraction, the ST power varies less at 100% load than 60% load.
- An increase of the TIT and the GT power due to the lower ST power. The nonlinearities are mainly caused by the nonlinear HRSG and ST model.

Figure 2.6 - 2.7 show the responses from two disturbances, i.e., the CH_4 concentration in NG, and load. The step changes are a 0.2% CH_4 increase/decrease and 0.1% decrease/increase of C_2H_6 and C_3H_8, and 10MW load changes at time 50s.A reduced load gives

- Increased surplus of fuel to the GT, reduced power production by the ST and GT, and decreased TIT. The dynamics are approximately linear and the time constants are small due to the usage of the buffer tank.
- No significant influence on the process because of the constant inputs to the H_2 production process.
- Increased captured CO_2 rate. The dynamics are nonlinear at different load. This is mainly due to the different carbon concentration in the buffer tank at different load.

When all the inputs are constant, changes in CH_4 concentration in the NG flow give the similar responses as the responses from changes in NG flow rate.

The positive and negative step responses at 100% load show that the responses from three inputs and two disturbances are approximate linear at this operating point except load by ST. However, the responses are nonlinear with respect to different operating points, e.g., different load. This is mainly because of the nonlinear reactor, GT, and ST models. Most of the responses have more than one time

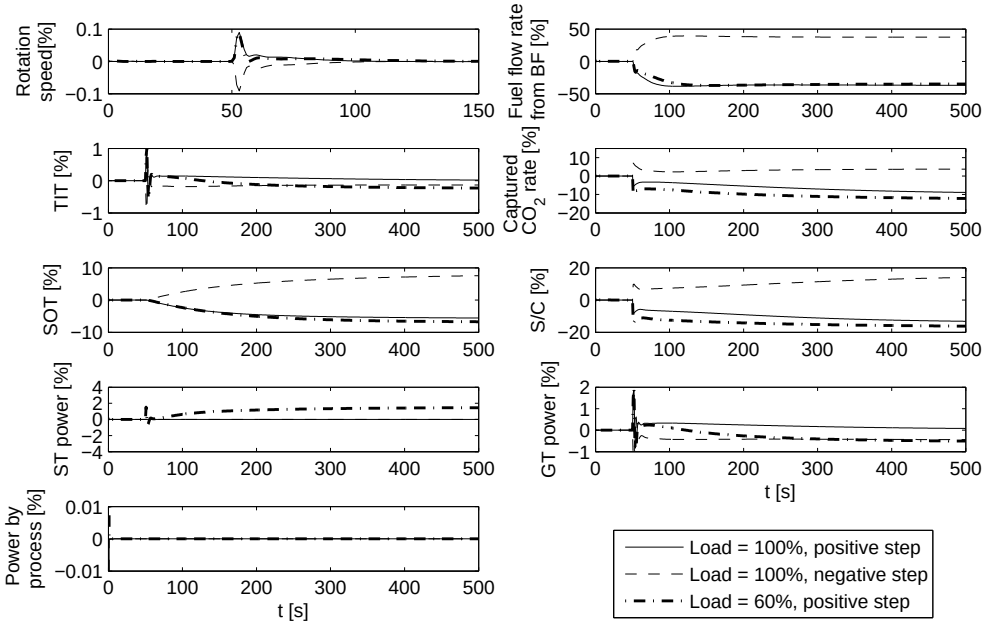

Figure 2.3: Dynamic responses from 10% NG flow rate changes at $50s$.

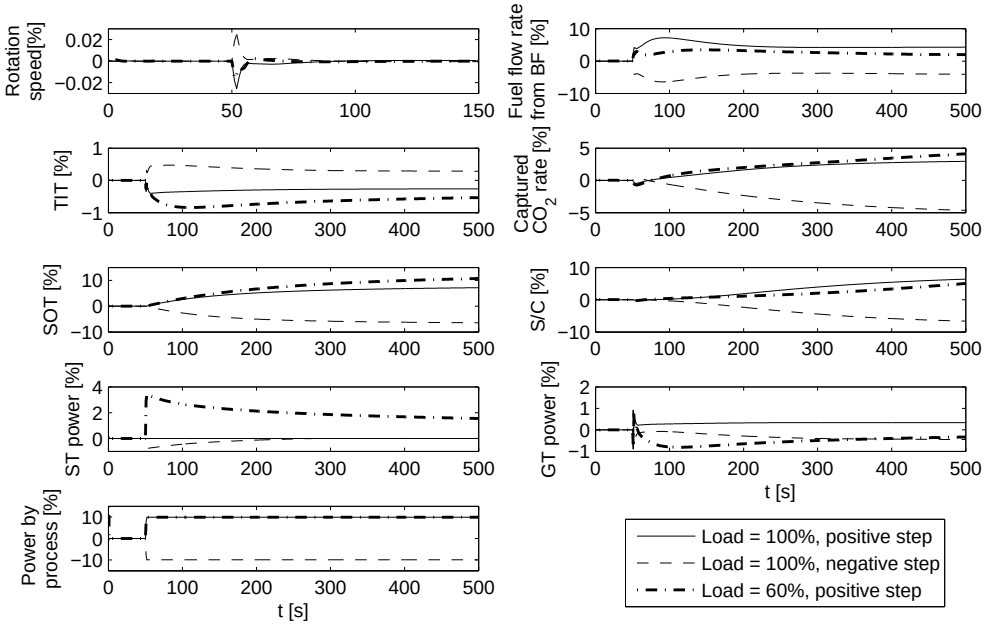

Figure 2.4: Dynamic responses from 10% air flow rate changes at $50s$.

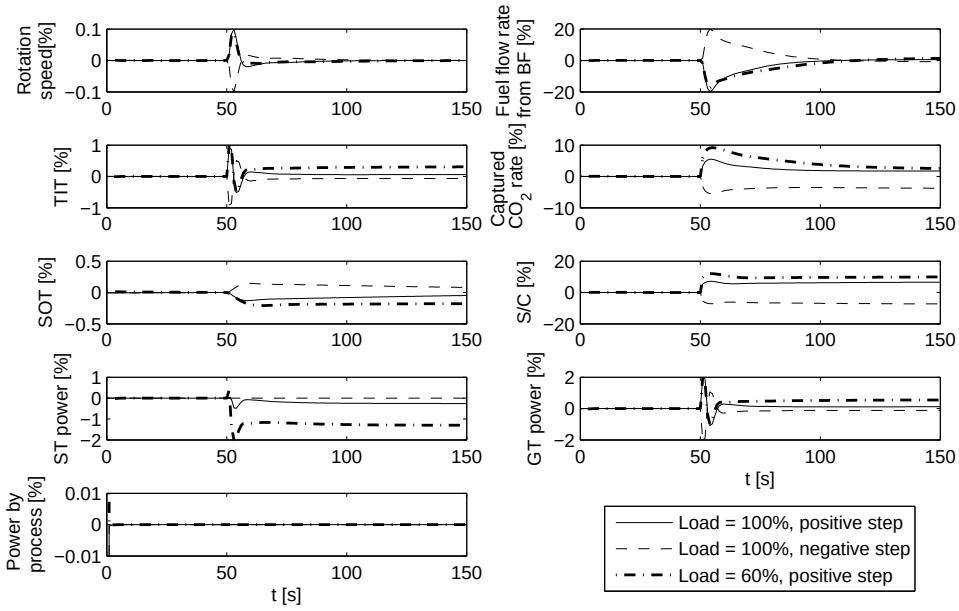

Figure 2.5: Dynamic responses from 10% steam flow rate changes at 50s.

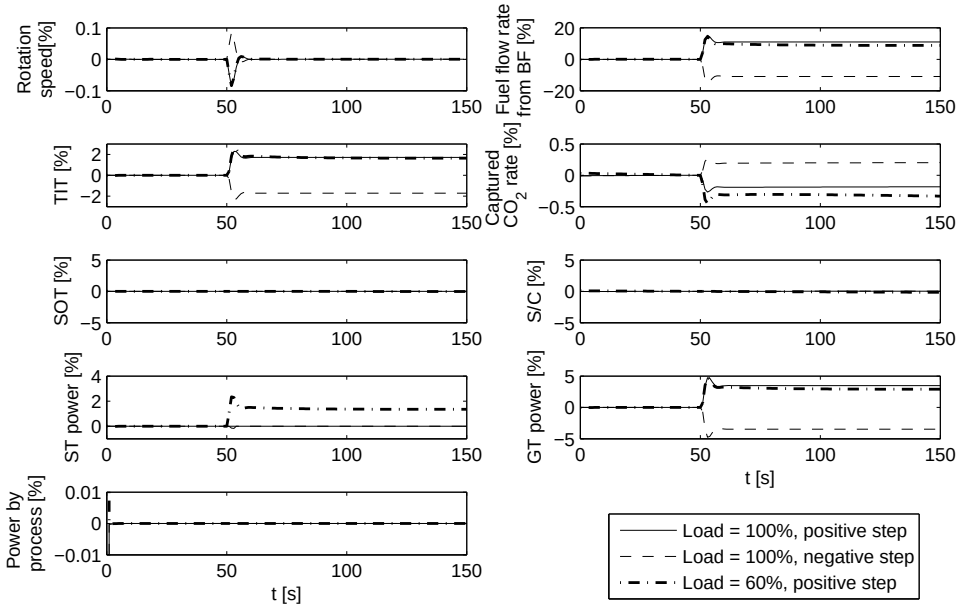

Figure 2.6: Dynamic responses from 10MW load changes at 50s.

constant. The fast responses are mainly caused by the fast flow rate; and the slow responses are caused by slowly varied temperatures.

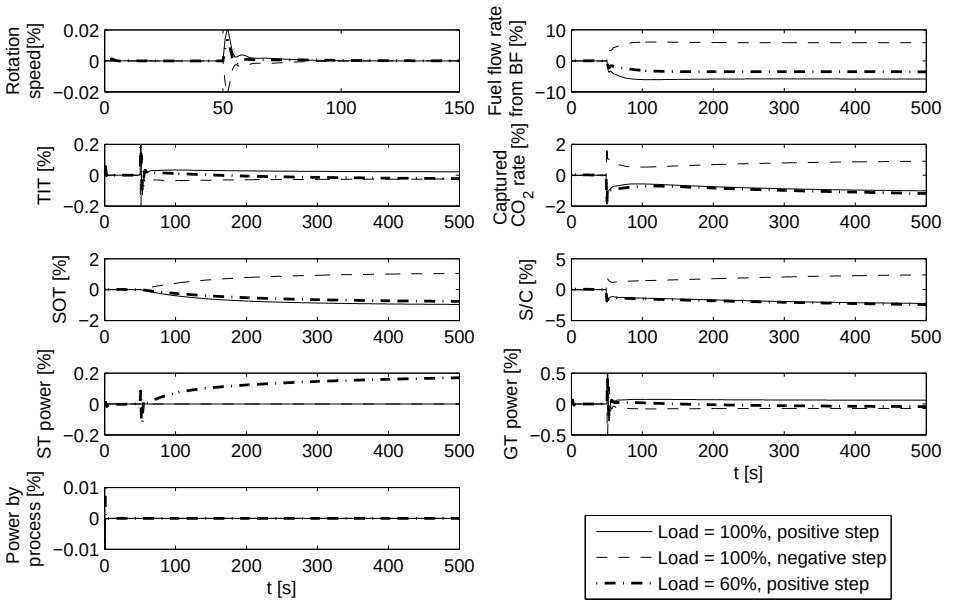

Figure 2.7: Dynamic responses from 2% CH_4 concentration changes at 50s.

2.4 Conclusion

In this chapter, steady state as well as dynamic models of a HMR based pre-combustion gas power cycle has been studied by simulation scenarios.

The HMR pre-combustion gas power cycle plant consists of reformers and separation units, compressors, gas and steam turbines and a heat recovery system. Analysis of dynamic models at an early stage of design can give valuable information to control structure design as well as to further process design. The dynamic models include a novel mathematical model based on first principles.

An Aspen Plus model was developed in the plant design phase for steady state process simulations. The SIMULINK model has been validated against that Aspen model by using available open literature data as well as data from in-house experiments. Parameters for chemical reactions and heat exchanges in the dynamic model were tuned at different operation points to obtain similar steady state values for compositions, flows, temperatures, pressures as obtained from the steady state data. The model errors are below 3%, which are satisfactory for the control structure design as described in the following chapters.

The simulations are focused on how different process inputs affect the important variables in the system, e.g., SOT, S/C ratio, TIT, GT power, ST power. They show that both the steady-state and dynamic behavior of the plant depend strongly on the load and the flow rates of feed streams.

The nonlinearities and the multiple time constants may cause difficulties when designing a control scheme with good operability and robustness. Moreover, control structure may vary for different economic objectives. Thus a systematic control design is implemented for this power cycle.

Chapter 3

Control structure design of the HMR power cycle

Control structure for the HMR power cycle is introduced in this chapter. First, a literature survey of control structure design for several similar processes as the HMR power cycle is presented. Then, the control structure design procedure proposed by Skogestad and Postlethwaite (2005) is introduced. Finally, design of a control structure for the HMR power cycle and dynamic simulation results are given to assess the control structure.

3.1 Literature survey

This section includes a survey of control structures for several similar processes as the HMR power cycle.

Stiller (2006) proposed a control structure of a SOFC and GT hybrid system based on a system analysis including RGA analysis of the model (Romagnoli and Palazoğlu, 2006). The dynamic simulation results showed that the proposed control strategy provided safe and efficient operation within the desired operation envelope.

Imsland et al. (2005) analysed a semi-closed O_2/CO_2 GT power cycle for CO_2 capture. The control structure was proposed based on an analysis of a dynamic model. A PI controller and an MPC based on a linearization of the model were compared. The results showed that the PI controller provides good power control at the expense of TIT constraint violations, whereas the MPC controller yielded much better control of temperature.

Govatsmark (2004) studied plant-wide control design for a single pressure combined cycle with a back-pressure steam turbine. Three different operating conditions were selected, and the system had eleven manipulated variables. A self optimising control design method was used to find the controlled variables, and the pairing was found from RGA analysis.

Robinson and Luyben (2011) studied a process that combines an integrated gasification combined cycle (IGCC) electric power plant with a methanol plant. The plant-wide control structure and interaction among units were shown, and the control structure for the methanol reaction section, methanol distillation sec-

tion, and hybrid IGCC/MeOH plant were studied. The results showed that large disturbances can be effectively handled by the plant-wide control structure.

Eichhorn Colombo et al. (2010) investigated the transient behaviour of a novel oxyfuel power plant. Two load-control strategies were selected based on system analysis. The results showed that load reduction with a variable air flow rate and a controlled turbine exit temperature was essential because of the considerably higher and faster load reduction capability, increased stability of the catalytic combustion in the membrane reactor, and the higher power plant efficiencies.

None of the previous studies apply a systematic control structure design method for the pre-combustion power cycles. In this study, the control structure design procedure proposed by Skogestad (2004) is used for the HMR power cycle. A control structure is proposed that gives the minimizes economic loss when the system is affected by various disturbances and uncertainties.

3.2 Introduction

The objective of control structure design is to develop a control structure that meets the design objectives for the process. Many industrial processes are complex because of recycle streams, energy integration, and many different unit operations. The number of measurements and inputs may hence be very large. A common approach is to decompose the system horizontally into subsystems which can be treated individually and hierarchically into several layers. Such a hierarchical control structure is shown in Figure 3.1. At the top layer, scheduling is made to perform business planning based on economic measures. The second layer solves the site-wide optimization problem based on the business planning and defines the objectives for local optimization, which is used to find the optimal operating conditions for the subsystems. The local optimization layer computes the setpoints for the control layers, which contain the supervisory layer and the regulatory layer. The supervisory layer tries to keep the controlled variables at optimal setpoints, while the regulatory layer rejects low level disturbances and keeps the system stable. These layers typically involve automatic feedback control whereas the layers above typically include humans in the loop.

At each control layer, control structure design may include the following tasks (Skogestad and Postlethwaite, 2005)

- Selection of controlled variables.
- Selection of manipulated variables.
- Selection of measurements.
- Selection of control configuration which interconnects measurements and manipulated variables.
- Selection of controller types e.g., PID, MPC.

A general feedback control structure is shown in Figure 3.2.

One approach to decide on the control structure is based on system insight which includes process analysis and engineering experiences. This process oriented

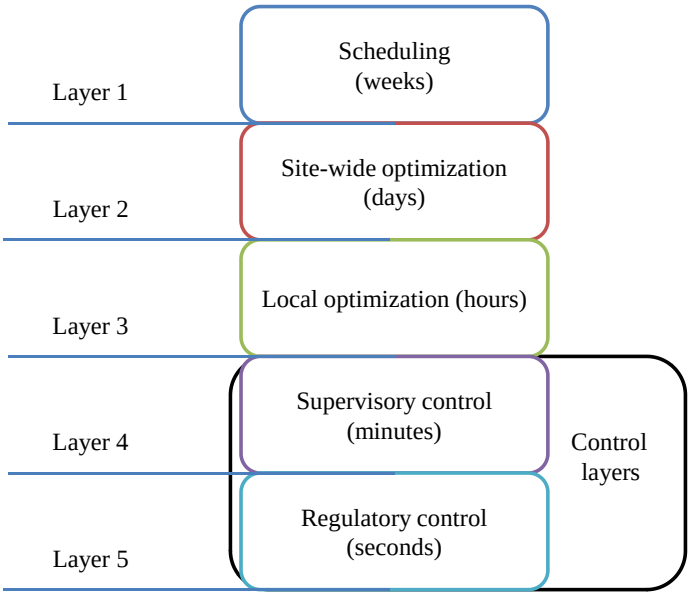

Figure 3.1: Hierarchical control structure.

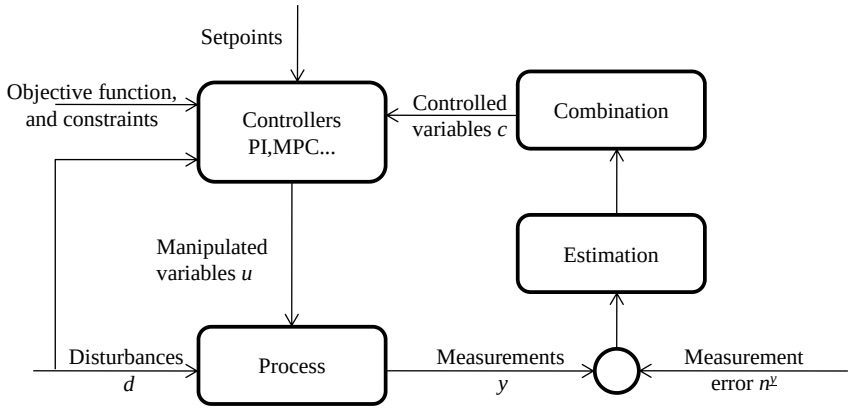

Figure 3.2: General feedback control structure.

approach starts with identifying the degree of freedom for control, available measurements and selection of controlled variables. Then the overall system is decomposed into several subsystems in some heuristic way. Some decomposition methods are discussed in the literature, e.g., unit-based (Umeda and Kuriyama, 1978), process structure based (Douglas, 1988; Ng and Stephanopoulos, 1998), control objective based (Luyben et al., 1997), and time based (Buckley, 1964).

Another approach is mathematically oriented. The control structure is found from a mathematical model or experimental data. A complete procedure for this approach is described by Skogestad (2004). The degree of freedom for control and measurements is first selected, and the controlled variables are found from the so-

called self-optimizing control design procedure. The control configuration which interconnects the control inputs and controlled variables can be centralized or decomposed into blocks of sub-systems. Some rules for selecting the configuration is described by Skogestad (2004). The first step is to choose the inputs for stabilizing control by using single-loop feedback controllers. Next, extra measurements are often added to improve the control. The controller can be centralized controllers, single loop controllers, or cascaded controllers.

The control structure design of the HMR and combined-cycle gas turbine system is done by using a procedure proposed for the design of control structures for chemical plants (Skogestad, 2004). This approach gives a systematic way to design the control structure.

3.3 Plant-wide control structure design

Table 3.1 provides an overview of the whole procedure. Each step of the design procedure is treated sequentially in a separate subsection below.

Table 3.1: The plantwide control structure design procedure.

I. Top-down analysis
1. Define operational objective and constraints.
2. Identify degrees of freedom and optimise for disturbances.
3. Choose primary controlled variables (CV).
4. Find where set the production rate should be set.
II. Bottom-up design.
5. Design regulatory control layer.
6. Design supervisory control.
7. Design optimisation layer.
8. Validation based on dynamic simulation.

3.3.1 Operating objectives and constraints

Different objectives may lead to different control structures. Choosing an appropriate operating objective is therefore essential for the whole procedure. The objectives may include the available plant inputs, product quality specifications, product grades and demand determination, environmental restrictions, and the range of safe operating conditions (Luyben et al., 1997).

An objective can be expressed by a function J with certain constraints.

$$J = \frac{1}{t_{end} - t_{start}} \int_{t_{start}}^{t_{end}} j(t)dt \tag{3.1}$$
$$C(t) \leq 0$$

Here, t_e, and t_s denote the start time and end time for the period of interest, and function C are a set of constraints. In many cases $j(t)$ is an economic cost

function. A steady state cost function is often considered because most of the time the plants operate at a steady state operating point. The operating objective is then a steady state cost function aimed to maximise the revenue generated by the product minus the inlet material and environment cost

$$J = j_{in} - j_{out}$$

where, j_{in} is the inlet materials and environment cost, and j_{out} is the production revenue.

3.3.2 Identify degrees of freedom and disturbances

The DoF for control are the number of variables that can be manipulated. One straightforward approach to find the DoF is e.g., by counting the number of control valves and other actuators available. The DoF for control and optimization is the number of variables with effect on the cost function J. Usually the DoF for optimization is less than the DoF for control. Some variables that can be used for control may not be used for optimization. One example is the pressure in a gas tank that may have no effect on J. Further, correlated variables will reduce the DoF for optimization. The DoF for optimization can be used to satisfy the constraints and to optimize the operation.

3.3.3 Primary controlled variables

Primary controlled variables are variables that need to be controlled to ensure optimal economic operation. Selection of controlled variables is probably the least studied problem in the control structure design procedure (Larsson and Skogestad, 2000). However, most of the processes select controlled variables based on engineering insight and experience. Some other approaches try to relate the selection rules to the economic loss, e.g., by applying self-optimizing control. Self-optimising control attempts to find the controlled variable with a constant setpoint that yields an acceptable level of loss despite disturbances, uncertainties, and noise. This concept was first introduced by Morari et al. (1980), and then further developed by Skogestad and co-workers (Skogestad, 2004; Alstad, 2005). Skogestad (2004) gives four requirements for selecting the controlled variables

1. Its optimal value should be insensitive to disturbances.
2. It should be easy to measure and control accurately.
3. Its value should be sensitive to changes in the manipulated variables.
4. For cases with two or more controlled variables, the selected variables should not be closely correlated.

Based on these requirements, three sets of controlled variables can be identified

1. Control variables to achieve a satisfactory regulatory control.
2. Control variables that hit limits at the optimal operating point.
3. Control variables that are not active but give the optimal solution in the presence of disturbances and uncertainties.

A brief introduction of self-optimising control is described below.

An optimal operating point of the power cycle can be found by solving the following optimisation problem with disturbances d at the nominal operating point d^*, for the sake of simplification $d^* = 0$.

$$\begin{aligned} \min_u J(u, y, d) \\ s.t.\ f(x, u, d) = 0 \\ y = g(u, x, d, n_y) \\ C_{in}(u, x, y, d) \leq 0 \\ C_{eq}(u, x, y, d) = 0 \end{aligned} \tag{3.2}$$

where u are the manipulated variables, x the system states, y the outputs, n^y measurement error, function f and g represent the system model, and C_{in} and C_{eq} are the inequality and equality constraints, respectively.

Generally, many of the constraints become active at the optimal point. Based on the three rules for controlled variable selection, these active constraints should be chosen as primary controlled variables. Next, the optimal solution in the presence of disturbances d should be determined. If there are active constraints, these constraints should be controlled. Otherwise multiple control structures can be used including a switching point when the disturbance value makes the constraints active.

The remaining DoF can be used to minimise the effect of disturbances and uncertainties.

Define

(u^*, d^*, y^*, c^*) as the nominal value.

$(u^{opt}, d, y^{opt}, c^{opt})$ as the optimal value for disturbance $d \neq d^*$.

(u, d, y, c) as the value with a selected control structure and disturbance d.

Here c are the controlled variables $c = h_c(y, n^y)$. h_c is hence some function which combines the controlled variables.

The objective function (3.3) is the difference between the optimal value and the values using constant control structures when various disturbances are applied to the system, see also Figure 3.3.

The following minimisation problem is formulated to find the controlled variables for the remaining DoF

$$\begin{aligned} \min_{h_c} L = J(u, d) - J(u^{opt}, d) \\ y^{opt} = g(u^{opt}, d) \\ y = g(u, d) \\ h_c(y) = h_c(y^* + n^y) \end{aligned} \tag{3.3}$$

This is a nonlinear optimization problem and can be solved by appropriate methods. The problem may, however, be simplified further as follows.

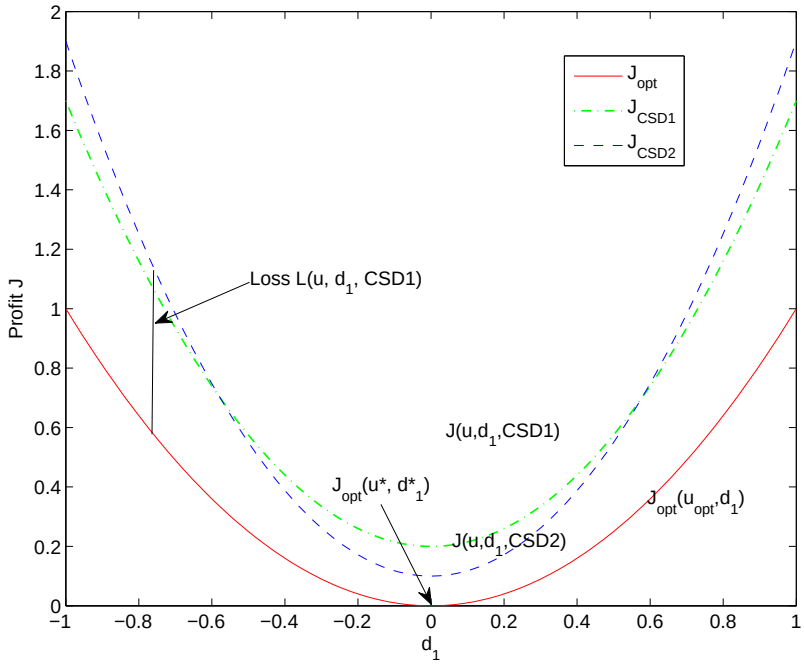

Figure 3.3: Losses due to disturbances.

First, use a first order Taylor series expansion at the optimal value to approximate $g(u, d)$

$$
\begin{aligned}
y &= g(u,d) \\
&= g(u^*,d^*) + \left.\frac{\partial g}{\partial u}\right|_{(u^*,d^*)} (u-u^*) + \left.\frac{\partial g}{\partial d}\right|_{(u^*,d^*)} (d-d^*) \\
&= y^* + g_u(u-u^*) + g_d(d-d^*) \\
y^{opt} &= y^* + g_u(u^{opt}-u^*) + g_d(d-d^*) \\
e_y &= y - y^{opt} = g_u(u-u^{opt}) = g_u e_u \\
\Delta y &= g_u \Delta u + g_d \Delta d \\
\Delta y &= y - y^*, \Delta u = u - u^*, \Delta d = d - d^*
\end{aligned}
\tag{3.4}
$$

Then, the loss function L can be approximated by the second order expansion of $J(u, d)$.

$$
\begin{aligned}
\min_{h_c} L &= \frac{1}{2} e_u^T J_{uu} e_u \\
e_u &= u - u^{opt}
\end{aligned}
\tag{3.5}
$$

Here, J_{uu} is the Hessian matrix of J.

Assuming J_{uu} is positive definite. When L is optimal, we have

$$\frac{dJ}{dd} = 0 \tag{3.6}$$
$$J_{uu}\Delta u = -\Delta d^T J_{du}$$

Here, J_{ud} is the second-order mixed derivatives of J.
Choose the control structure as a linear combination of measurements

$$h_c(y, n^y) = H_c(y + n^y) \tag{3.7}$$

The problem (3.3) is thus reduced to

$$\min_{H_c} L = \frac{1}{2} e_u^T J_{uu} e_u \tag{3.8}$$
$$s.t.\ \Delta y = g_u \Delta u + g_d \Delta d \tag{3.9}$$
$$J_{uu}\Delta u = -\Delta d^T J_{du} \tag{3.10}$$
$$e_y = g_u e_u \tag{3.11}$$
$$H_c y = H_c(y^* + n^y) \tag{3.12}$$

(3.12) and (3.11) are substituted into (3.8)

$$\min_{H_c} L = \frac{1}{2} e_c^T (H_c g_u)^{-T} J_{uu} (H_c g_u)^{-1} e_c \tag{3.13}$$
$$e_c^T = -H_c(y^{opt} - y^*) - H_c n^y$$

A scaling matrix W_s is chosen which gives $e_{c,2} = W_s e_c$ and $\|e_c'\| \leq 1$. This yields

$$\min_{H_c} L = \frac{1}{2} (W_s^{-1} e_{c,2})^T (H_c g_u)^{-T} J_{uu} (H_c g_u)^{-1} W_s^{-1} e_{c,2} \tag{3.14}$$
$$\leq \frac{1}{2} \sigma \left(J_{uu}^{\frac{1}{2}} (H_c g_u)^{-1} W_s^{-1} \right)$$

where σ is the singular value of the matrixes $J_{uu}^{\frac{1}{2}} (H_c g_u)^{-1} W_s^{-1}$. If e_c is independent of the disturbances and

$$W_s = diag\left(\frac{1}{e_c}\right) \tag{3.15}$$

The problem is to find the maximum value of $\sigma\left(W_s H_c g_u J_{uu}^{-\frac{1}{2}}\right)$ with respect to different inputs. This approach equals the so-called maximum gain rule. This method may give poor results for multiple inputs because of the correlation of the different inputs. We can, however, use the system model to overcome this drawback.
Substitution of (3.9) and (3.10) into (3.13) gives

$$\min_{H_c} L = \frac{1}{2} e_u J_{uu} e_u \tag{3.16}$$
$$e_u = (H_c g_u)^{-1} H_c (g_u J_{uu}^{-1} J_{ud} - g_d)(d - d^*) - (H_c g_u)^{-1} H_c n_y$$

Giving the scaling matrices $W_{s,d}$ and $W_{s,n}$, then $d - d^*$ and n_y can be written as

$$\begin{aligned} d - d^* &= W_{s,d} d' \\ n_y &= W_{s,n} n^{y\prime} \end{aligned} \tag{3.17}$$

which satisfy

$$\left\| \begin{bmatrix} d' \\ n^{y\prime} \end{bmatrix} \right\|_2 \leq 1 \tag{3.18}$$

The objective function of the optimization problem is then

$$\min_{H_c} L = \frac{1}{2} z^T z \tag{3.19}$$

$$\begin{aligned} z &= J_{uu}^{\frac{1}{2}} e_u \\ e_u &= (H g_u)^{-1} H_c \begin{bmatrix} -FW_{s,d} & -W_{s,n} \end{bmatrix} \begin{bmatrix} d' \\ n^{y\prime} \end{bmatrix} \\ F &= -\left(g_u J_{uu}^{-1} J_{ud} - g_d \right) \end{aligned} \tag{3.20}$$

To minimise the worst case loss is equivalent to minimising the singular value σ of z with respect to H_c, g_u, and g_d.

The problem becomes

$$\min \sigma \left(J_{uu}^{\frac{1}{2}} (H_c g_u)^{-1} H_c \begin{bmatrix} -FW_{s,d} & -W_{s,n} \end{bmatrix} \right) \tag{3.21}$$

Note that

$$\begin{aligned} u \in R^{n_u}, d, d' \in R^{n_d}, y, n'_y \in R^{n_y} \\ z, e_u \in R^{n_u}, J_{uu} \in R^{n_u \times n_u}, J_{ud} \in R^{n_u \times n_d} \\ g_u \in R^{n_y \times n_u}, g_d \in R^{n_y \times n_d} \\ F \in R^{n_y \times n_d}, H_c \in R^{n_u \times n_y} \end{aligned} \tag{3.22}$$

where n_u, n_y, and n_d are the number of inputs, outputs, and disturbances, respectively.

Here we assume that there are more measurements available than the number of inputs and disturbances, i.e., $n_y \geq n_u + n_d$. More controlled variables will lead to the less loss because more variables can be used to minimize the objective function. In practice, however, we may want to install as few measurements as possible to reduce the costs of installation. This leads to the problem of how to select the minimal set of measurements that gives the minimal loss under influence of disturbances.

Based on the discussion above, a minimum number of measurements to design control variable is $n_u + n_d$ measurements from the candidate measurements, and thus the optimisation problem becomes

$$\min \sigma \left(J_{uu}^{\frac{1}{2}} (H_c S_1 g_u)^{-1} H_c S_1 \begin{bmatrix} -FW_{s,d} & -W_{s,n} \end{bmatrix} \right) \tag{3.23}$$

Here, $S_1 \in R^{(n_u + n_d) \times n_y}$ is the matrix used to select the measurements.

Several methods can be used to solve the problem as discussed in Michelsen et al. (2010) and Alstad (2005). A brute-force method is to test all possible combinations and to find the minimal solution, which gives the global solution. The total number of calculations for solving the optimization problem is then $\frac{n_y!}{(n_u+n_d)!(n_y-n_u-n_d)!}$.

A sequential method first selects the largest element from

$$J_2 = \left\| J_{uu}^{\frac{1}{2}} (H_c g_u)^{-1} H_c \begin{bmatrix} -FW_{s,d} & -W_{s,n} \end{bmatrix} \right\|_2 \tag{3.24}$$

Then, the remaining measurements are added one by one until the number of selected measurements is $n_u + n_d$. The measurement that gives the minimal value of J_2 is added at each iteration. The sequential method may not give the global optimal solution.

Alstad (2005) provided a suboptimal method to determine the subset of the measurements. First, H_c is chosen to make $J_{uu}^{\frac{1}{2}}(H_c g_u)^{-1} = I$, and then objective function (3.25) is used. The objective function is equivalent to minimising the scaled gain matrix from the inputs and the disturbance to the outputs. The derivation of this approach is described by Alstad et al. (2009).

$$\min \sigma \left(g'_u + g'_d \right) \tag{3.25}$$

For a given process, the following procedure gives the matrices required for the optimisation problem

- A matrix F is defined as the gain from a change of disturbances to the measurements y. When the objective function is at its optimum, F can be calculated by making a change in each disturbance.

$$F = \begin{bmatrix} \frac{y_1^{opt}(d_1)-y_1^*}{d_1-d^*} & \cdots & \frac{y_1^{opt}(d_{n_d})-y_1^*}{d_{n_d}-d^*} \\ \vdots & \ddots & \vdots \\ \frac{y_{n_y}^{opt}(d_1)-y_{n_y}^*}{d_1-d^*} & \cdots & \frac{y_{n_y}^{opt}(d_1)-y_{n_y}^*}{d_{n_d}-d^*} \end{bmatrix} \in R^{n_y \times n_d} \tag{3.26}$$

  To find this matrix we need n_d optimisation runs, i.e., one for each disturbance. Also, F can be calculated by (3.20).

- g_u and g_d are the gains from the inputs and disturbances to the measurements

$$g_u = \begin{bmatrix} \frac{y_1(u_1)-y_1^*}{u_1-u_1^*} & \cdots & \frac{y_1(u_{n_u})-y_1^*}{u_{n_u}-u_{n_u}^*} \\ \vdots & \ddots & \vdots \\ \frac{y_{n_y}(u_1)-y_{n_y}^*}{u_1-u_1^*} & \cdots & \frac{y_{n_y}(u_{n_u})-y_{n_y}^*}{u_{n_u}-u_{n_u}^*} \end{bmatrix} \in R^{n_y \times n_u} \tag{3.27}$$

$$g_d = \begin{bmatrix} \frac{y_1(d_1)-y_1^*}{d_1-d^*} & \cdots & \frac{y_1(d_{n_d})-y_1^*}{d_{n_d}-d^*} \\ \vdots & \ddots & \vdots \\ \frac{y_{n_y}(d_1)-y_{n_y}^*}{d_1-d^*} & \cdots & \frac{y_{n_y}(d_{n_d})-y_{n_y}^*}{d_{n_d}-d^*} \end{bmatrix} \in R^{n_y \times n_d}$$

  $n_d + n_u$ simulations are needed.

- The Hessian matrix can be found from a first order approximation

$$J_{uu} \in R^{n_y \times n_d} = \tag{3.28}$$

$$\begin{bmatrix} \frac{J(u_1)+J(u_1')-2J(u^*)}{\Delta u_1^2} & \cdots & \frac{J(u_1,u_{n_u})-J(u_1^*,u_{n_u})-J(u_1,u_{n_u}^*)+J(u_1^*,u_{n_u}^*)}{\Delta u_1 \Delta u_{n_u}} \\ \vdots & \ddots & \vdots \\ \frac{J(u_1,u_{n_u})-J(u_1^*,u_{n_u})-J(u_1,u_{n_u}^*)+J(u_1^*,u_{n_u}^*)}{\Delta u_1 \Delta u_{n_u}} & \cdots & \frac{J(u_{n_u})+J(u_{n_u}')-2J(u_{n_u}^*)}{\Delta u_{n_u}^2} \end{bmatrix}$$

Here $\Delta u_k = u_k - u_k^* = u_k^* - u_k'$. $\frac{n_u!}{2!(n_u-2)!}$ simulations are needed.

3.3.4 Set the production rate

The location where to set the production rate affects the control structure considerably. The production rate is set at its bottleneck when a plant is running at maximum capacity (Buckley, 1964). An upstream process of this location has to process whatever enters, and a downstream process of this location has to produce the desired production.

3.3.5 Design regulatory control layer

Examples of controlled variables in the regulatory control layer are (Luyben et al., 1997; Skogestad, 2004)

- Liquid levels and gas pressures.
- Flow in a recycle loop.
- Individual unit operation, e.g., a tubular reactor usually requires control of the inlet temperature.
- Product quality and safety control variables.
- Local disturbance rejection, e.g., pressure and temperature control for the inlet NG flow.

These variables can be controlled with the manipulated variable that has the largest effect on them (Luyben et al., 1997). PI type controllers are selected to ensure that the controlled variables stay in the vicinity of the setpoint and reduce the effect caused by noise.

3.3.6 Design supervisory control layer

The supervisory control layer can be centralized, e.g., centralized MPC, or decentralized. A centralized controller combines all the controlled variables and inputs, and it reduces the complexity of the control loop configuration. However, a decentralized configuration may have some advantages, e.g., less computation, less sensitive to model uncertainty, less cost to make the controller, faster response for disturbances, and higher failure tolerance.

3.3.7 Design optimisation layer

The optimisation layer evaluates and alters the operating conditions of a process continually to maximize the economic productivity of the process. An advanced approach used in the optimization layer is real-time optimization (RTO). RTO is usually based on steady state models. Steady state real-time optimization calculates the setpoints for the control layers by solving the following problem

$$\begin{aligned} \min_{c_s} J(u,d,y) \\ s.t.\ f(u,x,d) &= 0 \\ y &= g(x,d) \\ c_s &= h(y) \\ C_{in}(u,x,y,d) &\leq 0 \\ C_{eq}(u,x,y,d) &= 0 \end{aligned} \tag{3.29}$$

Here, J is generally an economic objective function, c_s are the setpoints for the controllers in the supervisory layer, functions f and g give the system model, h presents the relation between measurements and controlled variables, C_{in} and C_{eq} are the inequality and equality constraints, respectively.

Self-optimising control used for the control layers can reduce the frequency with which to run the optimisation layer.

3.3.8 Validation based on dynamic simulation

The previous analysis are mainly based on steady state models. The selected control loops may give some performance degradation if the dynamic responses are nonlinear. Hence, the designed control structures should be validated by dynamic simulations.

3.4 Control structure design of the HMR power cycle

This section describes design of a plant-wide control structure for the HMR power cycle following the procedure as outlined in last section.

3.4.1 Operating objectives and constraints

The operating objective of the HMR power cycle is described by a steady state cost function that is used to maximise the revenue generated by electricity minus the costs of the inlet materials and emissions

$$\begin{aligned} J &= w_{fuel}\dot{n}_{fuel} + w_{air}\dot{n}_{air} + w_{CW}\dot{n}_{CW} - w_p P_{net} + w_{CO_2}\dot{n}_{CO_2} \\ \text{where } P_{net} &= P_{GT} + P_{ST} - W_{AC} - W_{CCO_2} - W_{CW1} \\ &\quad - W_{CW2} - W_{MDEA} - W_{BFW} - W_{UA} \end{aligned} \tag{3.30}$$

Here, w are the prices for each input and output factor. $\dot{n}_{fuel}$, $\dot{n}_{air}$, $\dot{n}_{water}$, and $\dot{n}_{CO_2}$ are the molar flow rates of NG, air, water, and CO_2 emission. P_{GT},

and P_{ST} are the electric power generated by the GT and ST, respectively. W_{AC}, W_{CCO_2}, W_{CW1}, W_{CW2}, W_{MDEA}, W_{BFW}, and W_{UA} are the electric work of the air compressor for HMR, CO_2 compressor, two cooling water pumps, MDEA plant pump to recycle sorption, the BFW pump, and other auxiliary power.

The objective function may be simplified. The inlet air and water are assumed to be under normal conditions (ambient temperature and pressure), so no cost is assumed for these two resources. Further, W_{CW1}, W_{CW2}, W_{MDEA}, W_{BFW}, and W_{UA} are neglected because they are very small compared to the other work components. Here, we consider the case of constant net electricity production, which is the general case when the plant is connected to an electric grid. This gives

$$J = w_{fuel}\dot{n}_{fuel} + w_{CO_2}\dot{n}_{CO_2} \tag{3.31}$$

with a net power production constraint

$$P_{net} = P_{GT} + P_{ST} - W_{CCO_2} - W_{C1} = const \tag{3.32}$$

P_{net} is chosen to be 390 MW at the nominal operating point, which is also defined as 100% load, while the price for natural gas is $5.56€/kmol$ $(23.70€/MWh)$. Further, two cases for the price of CO_2 emissions are considered: case 1, $0.71€/kmol$ $(16.15€/t)$, which is the current value, and case 2, $1.50€/kmol$ $(34.09€/t)$, which may be reached in the future.

The constraints are chosen based on experience and design specifications. Further, we ignore the detailed structure of the HRSG and assume that all the process units are perfectly controlled and that the NG pressure and temperature are well controlled before entering the system. Table 3.2 shows the equality constraints and Table 3.3 shows the inequality constraints which may be active during operation. The values in these tables originate from several sources as included in the last column of the tables.

3.4.2 Identification of degrees of freedom and disturbances

The variables in Table 3.4 are selected for optimization. A pre-assumption for this is that the variables in the HRSG and ST are well controlled. Hence, the DoF for these units are not considered here.

During normal operation, the power cycle may encounter many types of disturbances, including

- Frequent load changes when the power cycle is connected to an electric grid.
- Leakage of pipelines for gas transportation that leads to reduced efficiency and reduced CO_2 capture rate in addition to potential hazardous effects.
- Changes in the ambient temperature and pressure changes influence especially the GT and STs (Saravanamuttoo et al., 2009).
- Variations in fuel feed pressure, temperature, or feed components.
- Variations in cooling water temperature.
- Damage in the reactors, especially membrane leakage in the HMR.

Table 3.2: The equality constraints in the HMR power cycle.

Constraint	Variable	Constraint value	Description
$C_{eq,1}$	The inlet fuel temperature of CC, $T_{CC,in}$	$400°C$	Design specification for the GT
$C_{eq,2}$	Rotation speed, N_{rs}	3000 rpm	Design specification for the GT
$C_{eq,3}$	Inlet temperature for desulphurisation reactor, $T_{DS,in}$	$400°C$	Design specification for the desulphurisation, reactor to obtain the best catalyst activity
$C_{eq,4}$	Inlet temperature for air compressor, $T_{Comp2,in}$	$50°C$	Design specification for air compressor, avoid damage and increase efficiency
$C_{eq,5}$	Outlet temperature for the cooling side of MTWGS, $T_{MTWGS,c,o}$	$237°C$	Temperature where all the water is vaporised at 32 bar
$C_{eq,6}$	Outlet temperature for HE5 cooling side, $T_{HE5,c}$	$237°C$	Temperature where all the water is vaporised at 32 bar
$C_{eq,7}$	Inlet temperature for flash tank, T_{FT}	$30°C$	Design specification of flash tank
$C_{eq,8}$	Outlet flow rate for the buffer tank, $\dot{n}_{fuel,b}$	$0kmol/s$	Fuel flow rate is 0 at steady state

Table 3.3: The inequality constraints in the HMR power cycle.

Constraint	Variable	Constraint value	Description
C_1	VIGV angle	$-30° < \alpha < 60°$	Design specification for the GT (Eichhorn Colombo et al., 2010)
C_2	GT fuel flow	$67\% < \dot{n}_{NG} < 100\%$	Design specification for the GT (Kiameh, 2002)
C_3	Extracted steam flow rate from ST	$0.8 < \dot{n}_{Steam} < 2.3\ kmol/s$	Design specification for HRSG (Thermoflow Inc., 2011).
C_4	Extracted air flow rate from GT	$0 < \dot{n}_{air,ex} < 20\%$	Air extraction from GT (Smith et al., 2002).
C_5	Turbine inlet temperature for the GT	$T_{TIT} < 1400°C$	Design specification for the GT (Chiesa et al., 2005)
C_6	Inlet S/C ratio for pre-reformer	$2.1 < r_{SC,PR} < 3.4$	Avoid carbon formation
C_7	Inlet S/C ratio for HMR	$2 < r_{SC,HMR} < 3.4$	Avoid carbon formation
C_8	Inlet temperature for pre-reformer	$300 < T_{PR,in} < 750°C$	Design specification for pre-reformer
C_9	Outlet temperature for pre-reformer	$300 < T_{PR,out} < 750°C$	Design specification for pre-reformer
C_{10}	Inlet temperature for HMR reforming side	$750 < T_{HMRp,in} < 1100°C$	Design specification for HMR
C_{11}	Outlet temperature for HMR reforming side	$750 < T_{HMRp,out} < 1100°C$	Design specification for HMR
C_{12}	Inlet temperature for HMR sweep side	$750 < T_{HMRs,in} < 1100°C$	Design specification for HMR
C_{13}	Outlet temperature for HMR sweep side	$750 < T_{HMRs,out} < 1100°C$	Design specification for HMR
C_{14}	Inlet temperature for MTWGS	$250 < T_{MTWGS} < 330°C$	Design specification for MTWGS
C_{15}	Inlet temperature for LTWGS	$190 < T_{LTWGS} < 210°C$	Design specification for LTWGS
C_{16}	CO_2 capture rate	$C_{CO_2} > 90\%$	Design objective
C_{17}	Pressure difference between HMR two sides	$P_{HMR,s} - P_{HMR,p} \leq 1bar$	Design specification for HMR
$C_{18} - C_{23}$	Bypass flow rate of heat exchangers	$0 < \dot{n}_{HX,bp} < 100\%$	Bypass flow rate for heat exchangers HE1, HE2, HE22, HE3, HE4, and HE9

Table 3.4: DoF for optimization of the HMR power cycle.

DoF	Variable	Description
u_1	$\dot{n}_{Steam}$ $[kmol/s]$	Extracted steam flow rate from HRSG
u_2	$\dot{n}_{Air}$ $[kmol/s]$	Extracted air flow rate from GT
u_3	$\dot{n}_{BFW}$ $[kmol/s]$	BFW flow rate
u_4	$\dot{n}_{NG}$ $[kmol/s]$	NG flow rate
u_5	$\dot{n}_{BF}$ $[kmol/s]$	Buffer tank flow rate
u_6	α [°]	VIGV angle
$u_7 - u_8$	$\dot{n}_{CW}$ $[kmol/s]$	Cooling water to HE11 and HE8
u_9	$p_{s,HE3}$ [%]	Flow rate proportion to the total flow rate
u_{10}	$p_{s,HE7}$ [%]	Flow rate proportion to the total flow rate
$u_{11} - u_{16}$	$\dot{n}_{by}$ $[kmol/s]$	Bypass flow rate for heat exchangers HE1, HE2, HE22, HE3, HE4, HE9
u_{17}	W_{AC} [MW]	Power by air compressor

The most important disturbances are considered to be load changes and fuel component changes. These disturbances are frequent during operation and influence the whole system significantly. Some disturbances only have effect locally and are easy to reject, e.g., cooling water temperature, fuel feed pressure and temperature. Some of the disturbances may not be easy to reject and may need replacement of devices, e.g., leakage of pipelines and damage of reactors. These disturbances are not considered here.

For the HMR power cycle, the important disturbances are listed in Table 3.5. The changes of CH_4 fraction are around the typical values which are 87.0 - 96.0% based on Union Gas (2012). The range of load changes is the same as the specification of the GT and ST models.

Table 3.5: Important disturbances in the HMR power cycle.

Disturbance	Variable	Range	Description
d_1 :	λ_{NG,CH_4} $[kmol/kmol]$	$[-5\%, 5\%]$	CH_4 molar fraction in NG.
d_2 :	P_L [MW]	$[-156, 10]$	The load $(60\% - 102.5\%)$.

3.4.3 Primary controlled variables

The controlled variables for the HMR power cycle are selected based on the self-optimising control design procedure as described in the last section. The equality constraints that should be controlled are those listed in Table 3.2. Eight DoF are used to satisfy these constraints. The constraint C_5 is difficult to measure in practice. Instead, the turbine exhaust temperature (TET) is selected as the controlled variable since the value of TET is easy to measure and related to TIT. TET is controlled to a calculated optimised value as function of the load. Thus, TET is an equality constraint which can be controlled by VIGV and inlet fuel flow rate. The outlet pressure of air compressor (u_{17}) is used to control the pressure difference

between the HMR streams. Further, the seven DoFs, u_1, u_2, u_{11}, u_{12}, u_{13}, u_{14}, and u_{16}, are left for optimisation.

The process is optimised with the objective function (3.31). To find the optimal point and reduce the calculation time, some decision variables, e.g., the variables that are active at the optimal solution, are first found through observation of the curve of the objective function with respect to each decision variable. The optimal solution is then found by a model-based method. This method is a derivative-free optimization method which uses a model to update the decision variables. A detailed description can be found in (Nocedal and Wright, 1999). The nominal optimal operating points for the two different CO_2 price cases are given in Table 3.6.

Table 3.6: Nominal optimal operating point for case 1 and case 2.

Nominal operation	Case 1	Case 2
Objective function (3.31) [€/s]	4.54	4.62
NG price [€/$kmol$]	5.56	5.56
Price of CO_2 emissions [€/$kmol$]	0.72	1.50
Number of active constraints	7	6
Number of DoF for self-optimizing control	0	1
LHV [MW]	754	770
Load [MW]	390	390
GT power output [MW]	287	289
ST net output [MW]	124	124
Auxiliary power including CO_2 compressed to 150 bar [MW]	21	23
Net efficiency (the ratio between load and LHV of NG) [%]	51.71	50.60
O/C [$kmol/kmol$]	0.95	1.07
S/C [$kmol/kmol$]	2.10	2.52
SOT [$°C$]	999	1095
Captured CO_2 rate [%]	90.00	96.57
TIT [$°C$]	1394	1387

Controlled variables for case 1

For the case with 0.71 €/$kmol$ of CO_2 emission, the optimal operation is found at the constraint for the CO_2 capture rate (90%). There are 7 active constraints (C_6, C_9, C_{15}, C_{16}, C_{19}, C_{21},and C_{23}) at this operating point. All manipulated variables are used to control the active constraints, and no DoF remains to reduce the loss due to disturbances.

Controlled variables for case 2

When the price for CO_2 emission is increased to 1.50 €/$kmol$, the optimal operation is at a higher CO_2 capture rate. SOT becomes active and higher capture efficiency is obtained. The results show that 6 constraints (C_9, C_{13}, C_{15}, C_{19}, C_{21},and C_{23})

are active and that one DoF can be used to minimise the effects of uncertainty and disturbances.

The set of candidate controlled variable are, see Table 3.7.

$$c_s^T = [\ u \quad \lambda_{CO_2} \quad r_{SC} \quad \lambda_{S6,H_2} \quad \lambda_{S6,H_2O} \quad \lambda_{S13,O_2} \quad \lambda_{LTWGS,CO} \quad P_{ST} \quad T_{S8}\ ] \tag{3.33}$$

These variables are observed to have large sensitivity to inputs changes and low sensitivity to disturbance changes.

Table 3.7: Candidate controlled variables.

Variable	Unit	Description
u	-	All of the inputs used in the optimisation
C_{CO_2}	$kmol/s$	Captured CO_2 rate
r_{SC}	$kmol/kmol$	Steam to carbine ratio at the pre-reformer inlet
λ_{S6,H_2O}	$kmol/kmol$	Syngas outlet H_2O concentration at the HMR reactor
λ_{S6,H_2}	$kmol/kmol$	SOH, syngas outlet H_2 concentration at the HMR reactor
λ_{S13,O_2}	$kmol/kmol$	Sweep gas outlet O_2 concentration at the HMR reactor
$\lambda_{LTWGS,CO}$	$kmol/kmol$	Outlet CO concentration at the LTWGS reactor
P_{ST}	MW	Power generated by the steam turbine.
T_{S8}	$^\circ C$	Pre-reformer outlet temperature

The measurement errors are assumed to be $1^\circ C$ for temperatures, 0.01 $kmol/s$ for flow rates, and 0.2 MW for power (Irwin, 2011).

One or a combination of measurements from the candidate set is selected as the controlled variable(s). In the following, two methods for selecting CVs described in section 3.3.3 are applied, see step 1 and 2 below. The final selection is subsequently based on evaluation of the loss in the two cases and simulation of the nonlinear simulator model.

1.Maximum gain analysis

Table 3.8 shows the selected scaled gain with respect to input, steam flow rate, and the two disturbances. The variable with the maximum gain is the S/C ratio. Hence we can use $y_1 = r_{S/C}$ as the last controlled variable. The optimal setpoint from optimization is 2.52.

Table 3.8: Selected maximum scaled singular value for candidate controlled variables.

Measurement	r_{SC}	λ_{S6,H_2O}	λ_{S6,H_2}	u_1	$\lambda_{LTWGS,CO}$	T_{S8}
Scaled gain G	4.9212	4.8911	2.8508	1.5495	1.2085	0.5950

If the load is reduced and the S/C ratio becomes active (Figure 3.4), then $r_{S/C}$ should be controlled to a constant setpoint of 2.1.

2. Null space method with measurement selection

The minimal number of controlled variables is 3 ($= n_d + n_u$). We want to find the combination of three controlled variables that provides the minimal loss in the presences of specified disturbances and uncertainties.

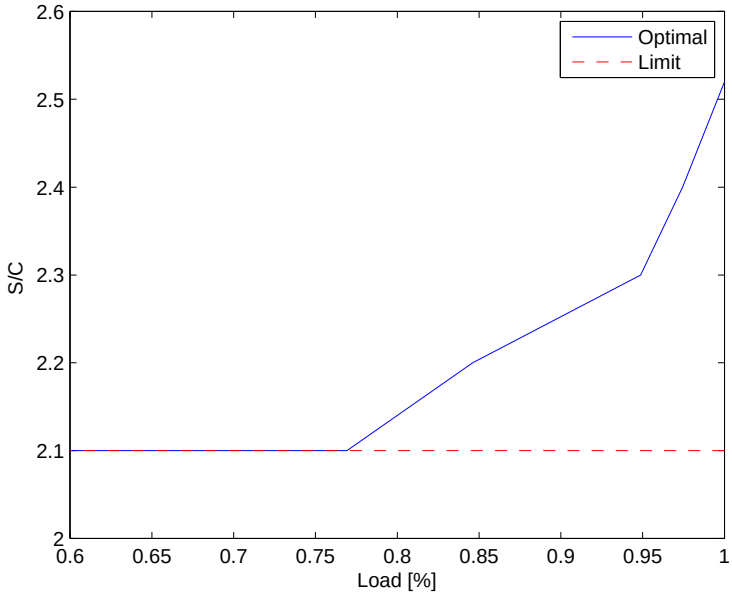

Figure 3.4: Optimum S/C with respect to a load change.

Different algorithms give two different controlled variables, y_2 and y_3. The first method is described by Alstad (2005). This approach gives a suboptimal solution assuming $Hg_u = I$. The second method is a brute-force method.

$$y_2 = -2.976u_1 + 6.514r_{SC} - \lambda_{S6,H_2O} \tag{3.34}$$

$$y_3 = 1.774u_1 - 1.951\lambda_{S6,H_2} - 0.042P_{ST} \tag{3.35}$$

To find which is the best of these controlled variables, the loss is calculated based on the nonlinear model. In Figure 3.5, the economic loss is shown as a function of load changes. The results show that the controlled variable y_2 gives the best results.

Conclusion

The results show that the control structure depends on the CO_2 price. When the cost of CO_2 emissions is low, the optimal operation is found at the lowest possible CO_2 capture rate. The other variables are adapted to obtain the lowest conversion rate. In addition to the controlled variables for regulatory control layers, the controlled variables are those controlled to their active constraints, i.e., r_{SC} (C_8), $T_{PR}(C_{10})$, $T_{LTWGS}(C_{14})$, $\lambda_{CO_2,cap}(C_{19})$, $\dot{n}_{HE2,bp}(C_{21})$, $\dot{n}_{HE3,bp}(C_{23})$, and $\dot{n}_{HE9,bp}(C_{25})$.

When the price of CO_2 emissions is increased to 1.50 €/$kmol$,CO_2 capture rate is no longer active. There are 6 active constraints, T_{SOT}, $T_{PR}(C_{10})$, $T_{LTWGS}(C_{14})$, $\dot{n}_{HE2,bp}(C_{21})$, $\dot{n}_{HE3,bp}(C_{23})$, and $\dot{n}_{HE9,bp}(C_{25})$.

Different algorithms yield different controlled variables for disturbance rejection. The controlled variable given by the maximum gain rule is r_{SC} (C_8) at high CO_2

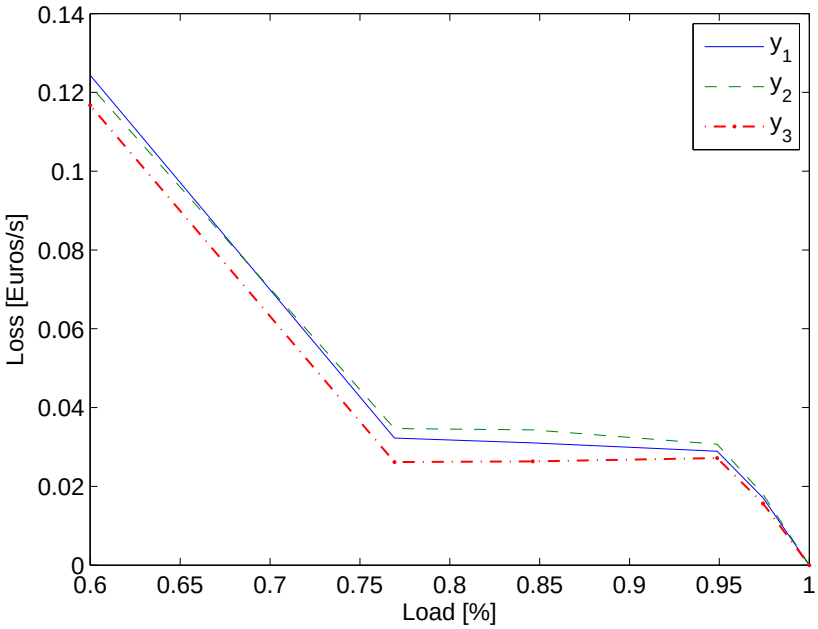

Figure 3.5: Losses due to load changes.

price. The advantage of selecting this variable is that minimal changes of the control structure are required when the operating conditions are changed because this variable is also an optimal active constraint in the case of low CO_2 price and is active in the presence of large disturbances, e.g., load reduced to below 300 MW. The controlled variable y_2 obtained from the null space method gives the minimal loss at high CO_2 price. The weakness of y_3 may be caused by the selection of a local minimum during optimisation.

The operating point and the switch of the control structure are depicted in Figure 3.6. The setpoints of S/C ratio and $T_{LTWGS,in}$ is varied with increased CO_2 price.

3.4.4 Set the production rate

In the HMR power cycle, the bottleneck when the plant is operating at 100% load is the GT capacity. Hence, the production rate is set at the inlet fuel flow rate of the combustion chamber.

In the former sections, a top-down analysis has been performed as a basis for the forthcoming design which starts with the regulatory control layer.

3.4.5 Design regulatory control layer

For the HMR power cycle, the following control loops are selected to achieve satisfactory regulatory control. The variables which are close to the controlled variables, and have direct and significant influence on the controlled variables, are selected

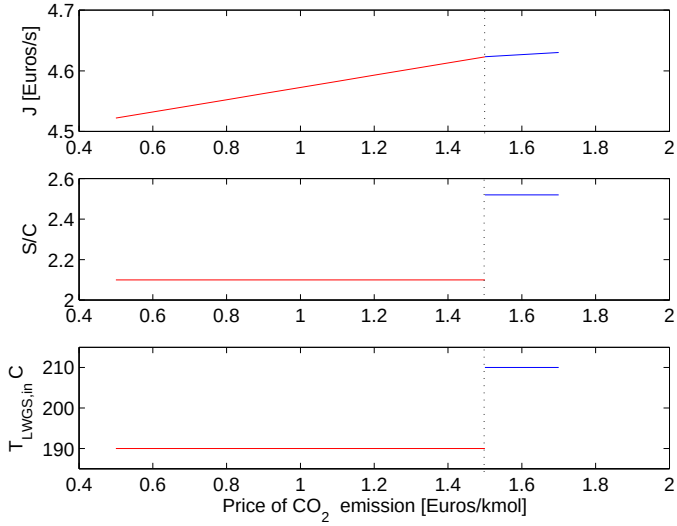

Figure 3.6: The switch of control structures.

to be the corresponding manipulated variables. PI type controllers are used for the simple structure and fast responses.

1. The cooling water to HE8 and HE11 is used to cool down the gas to the design value. These two control loops maintain the heat exchangers at design values and do not allow the other processes to exert significant influences on the temperature. The corresponding constraints are $C_{eq,4}$, and $C_{eq,7}$.
2. The outlet temperature from the cooling water side of HE5 and the MTWGS is controlled to satisfy the constraints $C_{eq,5}$, and $C_{eq,6}$. The manipulated variables are u_3 and u_{10}, respectively.
3. Flow rate proportion (u_9) is used to control the inlet fuel temperature to GT and satisfy the constraints $C_{eq,1}$.
4. The bypass flow rate of HE4, u_{15}, is used to control the desulphurisation inlet temperature. The corresponding constraint is $C_{eq,3}$.
5. The NG flow rate u_4 is used to control the rotation speed ($C_{eq,2}$). To obtain a fast response, a buffer tank is installed at the CC inlet. At steady state, the fuel flow from the buffer tank should be zero ($C_{eq,8}$). A cascade controller using NG to control the fuel flow from the buffer tank, and fuel flow rate from the buffer tank u_5 to control the rotation speed is used. The corresponding constraint is C_7.
6. We assume that VIGV (u_6) is used to control TET. For some combined cycles, TET is kept constant to obtain a high net efficiency of the combined cycle (Bolland, 2009). The corresponding constraint is C_5.
7. The outlet pressure of air compressor u_{17} is used to satisfy the constraint C_{17}.

3.4.6 Design supervisory control layer

The pairing of the supervisory layer follow the same rule as described in the regulatory control layer. A decentralized control structure for this layer is chosen. The control structures in the two above cases are described in the following sections.

Control structure for case 1

In addition to the regulatory control loops, the bypass flow of heat exchangers, HE1, HE2, HE22, HE3, and HE9, is used to control the corresponding outlet temperature. The S/C is controlled by the steam flow rate $\dot{n}_{steam,extr}$ because this variable has a direct effect on the controlled variable and it also gives the largest gain in the relative gain array analysis (RGA). The remaining controlled variable C_{CO_2} is controlled by the air flow rate $\dot{n}_{air,extr}$.

The load may change frequently during operation, and the values are easy to measure. Feedforward controllers can be applied for this control loop. Since the responses from NG and steam flow rate to the controlled variables are relatively fast, in seconds, steady state controllers with polynomial functions can be used to compensate the load change.

The complete control structure is shown in Figure 3.7.

Control structure for case 2

In case 2, the bypass flow rate of heat exchangers, HE2, HE22, HE5, HE3, and HE9, are controlled. SOT is active, and the air flow rate $\dot{n}_{air,extr}$ is used as the manipulated variable. The gain from the air flow rate to T_{SOT} is larger than those for the other variables. The last measurement can be y_1 (S/C) or y_2, i.e., a combination of $\dot{n}_{steam,extr}$, r_{SC}, and λ_{HMR,H_2}. The manipulated variable is $\dot{n}_{steam,extr}$. The complete control structure is shown in Figure 3.8.

All control loops for case 1 and case 2 are outlined in Table 3.9.

3.4.7 Design optimisation layer

The control structure design is based on self optimising control, which gives the best solution when the setpoint remains unchanged. Self-optimising control can reduce the frequency with which to run the optimisation layer. In this study, however, no optimisation layer is investigated for the HMR power cycle.

3.4.8 Validation based on dynamic simulation

In this section, the control type is selected and control performance for each loop is investigated. Finally, the dynamic responses of the whole plant for two different scenarios are studied. These changes in load and concentration are for testing the dynamic response of the system, and do not necessarily represent changes in residential load.

1. The disturbances are the net power load reduced from 100% to 60% during $20s$ ($50s$ to $70s$) and increased to 80% during $20s$ ($600s$ to $620s$), see Figure 3.9.

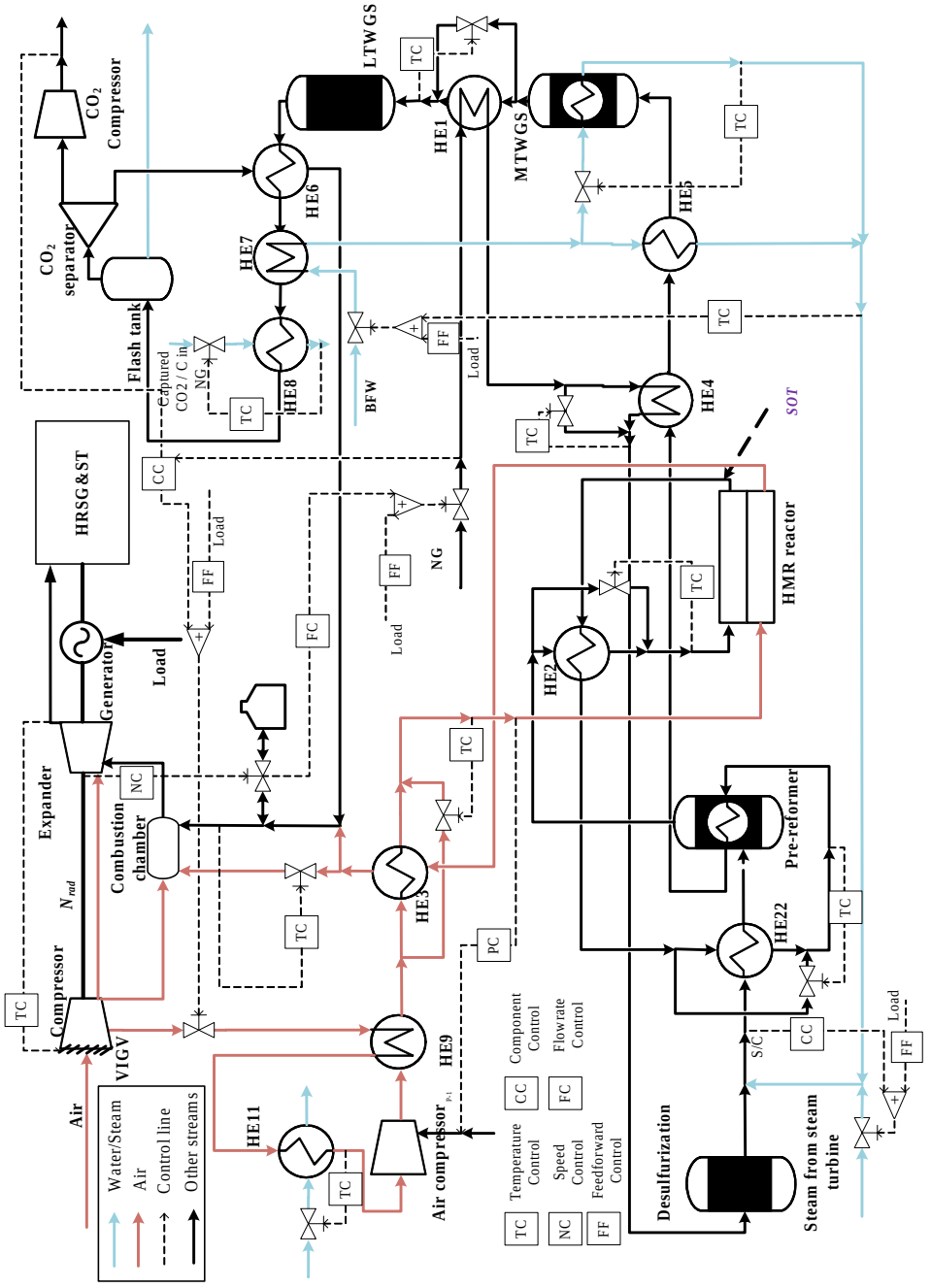

Figure 3.7: The control structure for case 1.

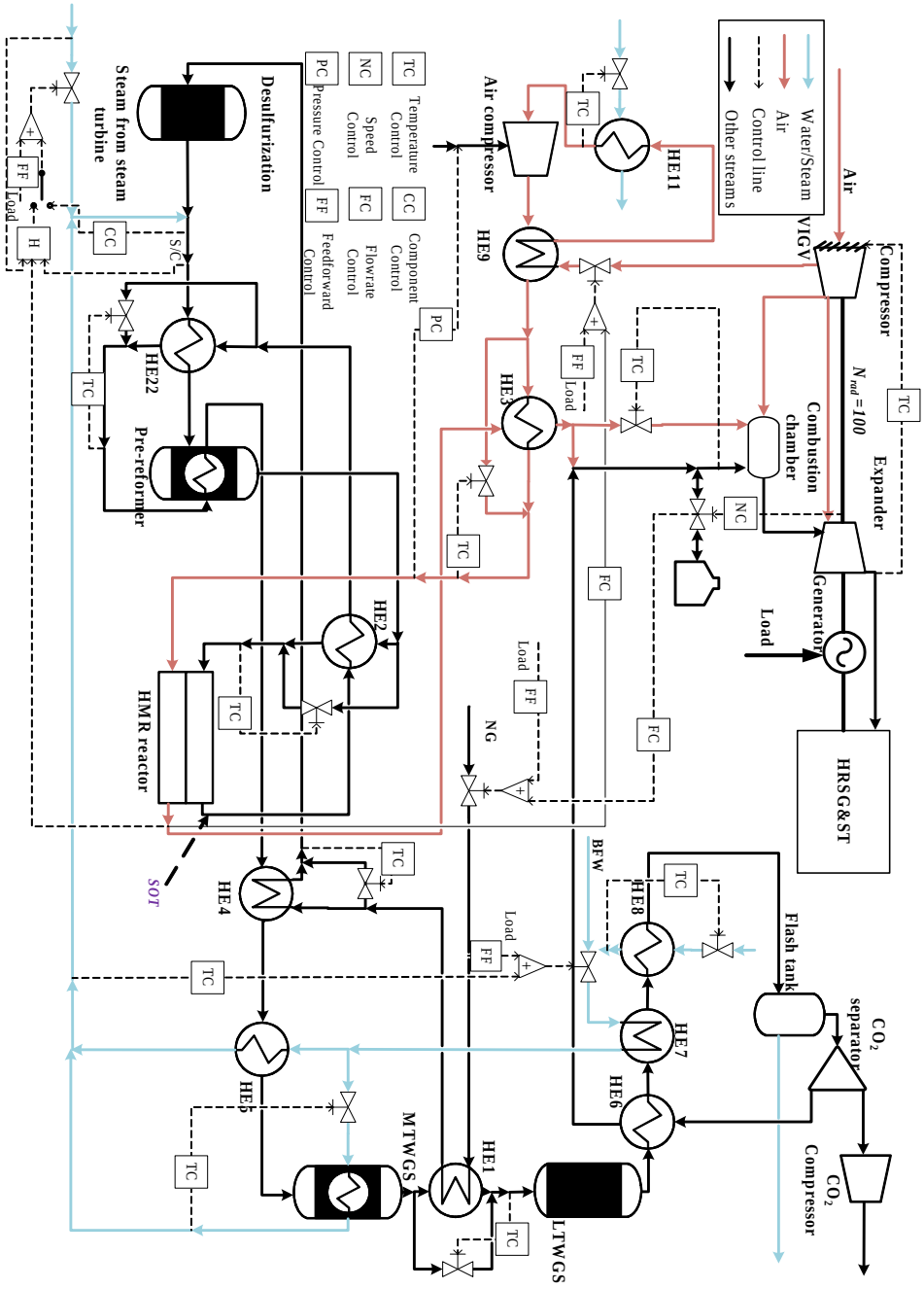

Figure 3.8: The control structure for case 2.

Table 3.9: Control loops for the HMR power cycle.

Regulatory control layer					
Control loop	1	2	3	4	5
Controlled variable	$T_{CC,in}$	N_{rs}	$T_{DS,in}$	$T_{AC,in}$	$T_{MTWGS,c,o}$
Corresponding constraint	$C_{eq,1}$	$C_{eq,2}$	$C_{eq,3}$	$C_{eq,4}$	$C_{eq,5}$
Manipulated variable	u_9	u_5	u_{15}	u_7	u_3
Control loop	6	7	8	9	10
Controlled variable	$T_{HE5,cg}$	T_{FT}	$\dot{n}_{fuel,b}$	T_{TIT}	$P_{HMR,p}$
Corresponding constraint	$C_{eq,6}$	$C_{eq,7}$	$C_{eq,8}$	C_5	C_{17}
Manipulated variable	u_{10}	u_8	u_4	u_6	u_{17}
Supervisory control layer					
Control loop	11	12	13	14	15
Controlled variable	$\dot{n}_{HE1,by}$	$\dot{n}_{HE2,by}$	$\dot{n}_{HE22,by}$	$\dot{n}_{HE3,by}$	$\dot{n}_{HE9,by}$
Corresponding constraint	C_{18}	C_{19}	C_{20}	C_{21}	C_{23}
Manipulated variable	u_{11}	u_{12}	u_{13}	u_{14}	u_{16}
Case	case1		case 2		
Control loop	16	17	16	17	
Controlled variable	$r_{SC,PR}$	C_{CO_2}	$T_{HMRs,o}$	y_2 (3.34)	
Manipulated variable	u_1	u_2	u_2	u_1	

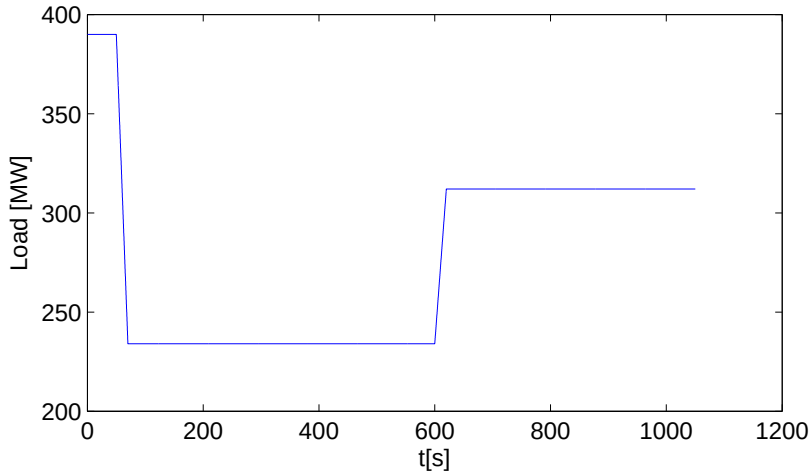

Figure 3.9: Disturbances in the power load.

2. The methane molar concentration is changed in a step-wise manner as shown in Figure 3.10.

Controller selection and tuning

Continuous PI type controllers including integrator wind-up functionality are used in all the control loops. These controllers are tuned for setpoint tracking with fast

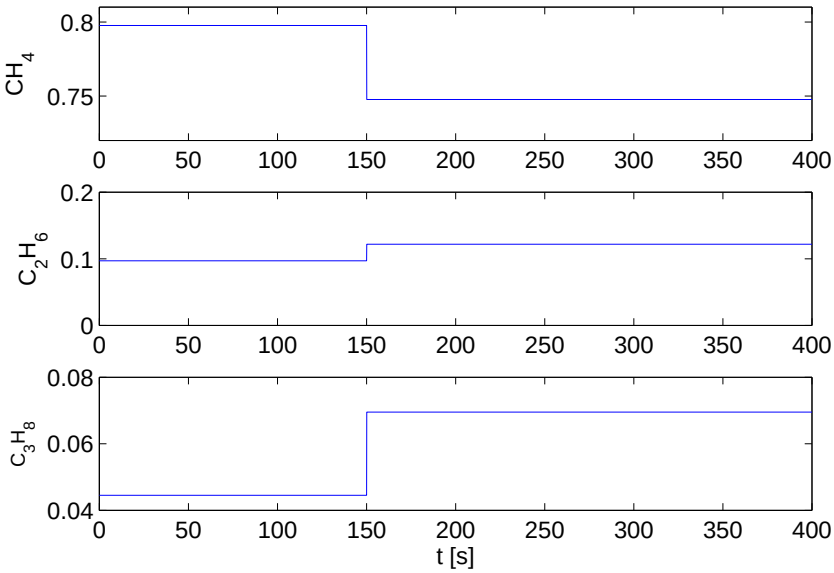

Figure 3.10: Disturbances in the NG molar concentration.

and flat responses, and disturbance rejection. All controllers have been implemented in the power cycle simulator.

The controller tunings are found through the following steps

1. Identify the transfer functions from the inputs and disturbances to the outputs based on perturbations.
2. Design controllers including, e.g., PID, feedforward, low pass filters, and inverse response compensators.
3. Make dynamic validation and tuning based on the nonlinear power cycle model.

The responses of the controlled variables from step changes in the manipulated variables for each control loop will be shown below. The feedforward control uses polynomial functions from curve fitting of steady state data.

1. The SOT control loop.

   A 10% step change of the manipulated variable is applied to tune the controller. The dynamics of the HMR temperature is relatively slow. Hence, a large PI gain is selected to reduce the response time and the overshoot. The simulation results of a well tuned controller are shown in Figure 3.11.

2. S/C ratio and rotation speed control loops.

   The steam flow rate directly affects the S/C ratio. The S/C ratio can be controlled tightly. The results in Figure 3.12 are the responses with respect to a 2% step change in the NG flow rate when all the control loops are closed in the power cycle. To keep the rotation speed of GT stable, the rotation speed controller reduces the fuel flow rate to the original value.

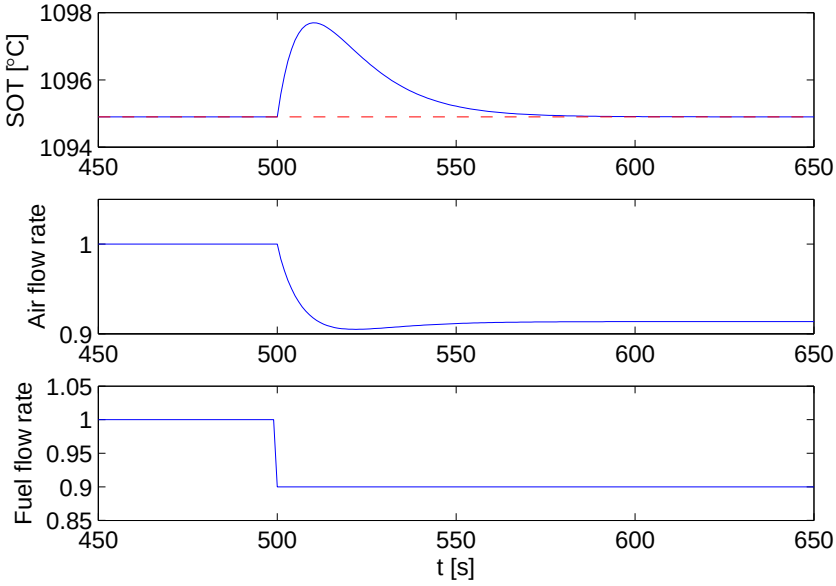

Figure 3.11: Dynamic responses of the HMR reactor with respect to a step change in inlet fuel flow rate on the reforming side.

3. CO_2 capture rate control loops.

   The step response from load change to captured CO_2 rate shows an inverse response (Figure 3.13). The inverse response is due to the storage of a greater amount of carbon in the reactors during transient time. This response can be considered as a difference between two first order responses which is described by the transfer functions G_{l1} and G_{l2}.

$$G_{l1} = \frac{C_1}{1+T_1 s}, G_{l2} = \frac{C_2}{1+T_2 s} \tag{3.36}$$

$$G_l = \frac{C_1}{1+T_1 s} - \frac{C_2}{1+T_2 s} \tag{3.37}$$

$$= k_l \frac{(1-T_z s)}{(1+T_1 s)(1+T_2 s)} \tag{3.38}$$

   There are several ways to control this kind of system to reduce the overshoot by PID controllers. Iinoya and Altpeter (1962) proposed a method using a modified Smith predictor with PI controller to improve the control performance. Figure 3.14 shows the structure when using such a compensator. H_1 is selected as a standard PID controller and H_2 is shown in (3.39).

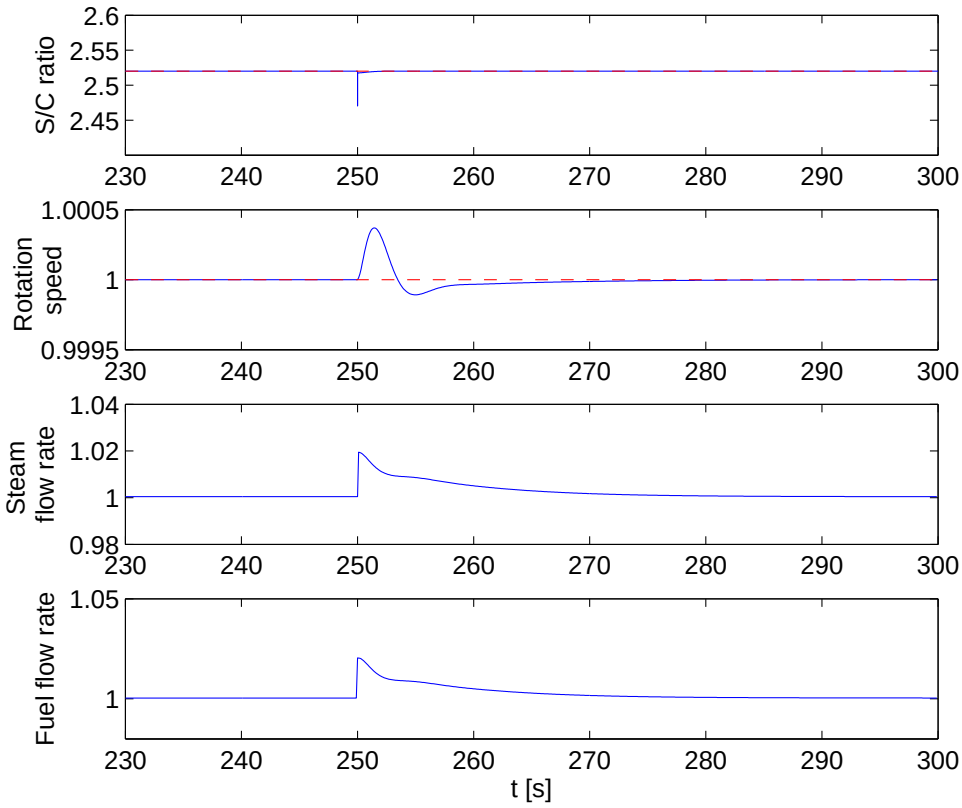

Figure 3.12: Dynamic responses of S/C ratio with respect to a step change of fuel flow rate.

$$H_2 = k\left(\frac{1}{T_2 s+1} - \frac{1}{T_1 s+1}\right) \tag{3.39}$$
$$k = \frac{C_2 T_1 - C_1 T_2}{T_1 - T_2}$$

Zhang et al. (2000) presents another inverse-response compensator based on the Smith predictor. In the paper, H_1 and H_2 are selected in (3.40)

$$H_1 = \frac{(T_1 s+1)(T_2 s+1)}{(C_2 - C_1)(\lambda s+1)^2} \tag{3.40}$$
$$H_2 = \frac{C_2}{T_2 s+1} - \frac{C_1}{T_1 s+1}$$

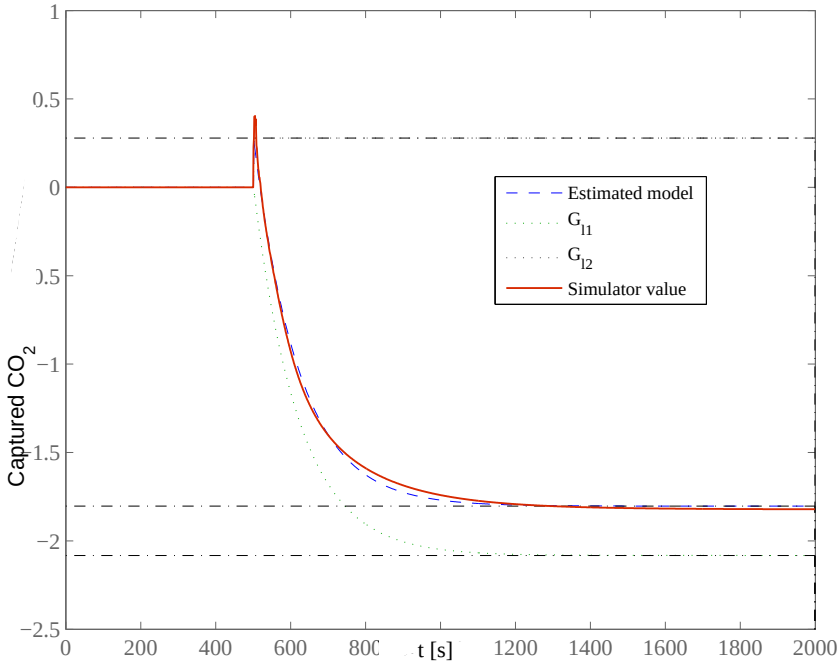

Figure 3.13: The step response of an air flow rate change.

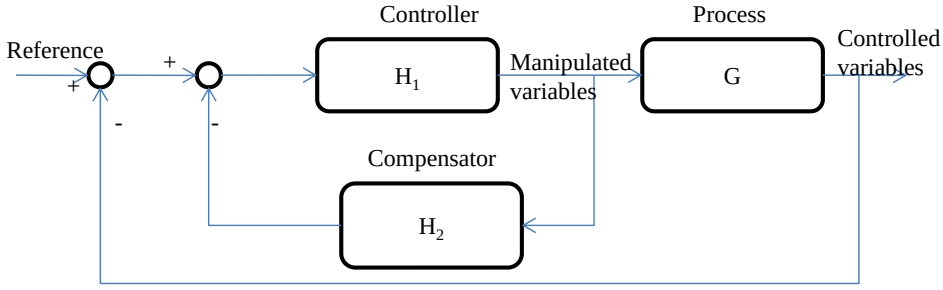

Figure 3.14: Control structure including a compensator for inverse responses.

where λ is a tuning parameter.

A PID controller can also be used to control inverse responses (Waller and Nygardas, 1975). Figure 3.15 shows the control performances of the three different control strategies from a 1.3% step change of the setpoint C_{CO_2}. Figure 3.16 shows step responses to a 15% step change of the inlet NG flow rate. The PID controller and λ in (3.40) are tuned manually. PID controller with a compensator as in Iinoya and Altpeter (1962) using the same PID gains as PID controller gives the similar performance as the controller by Zhang et al. (2000). Since the controller in Zhang et al. (2000) relies on the process model, a mismatch of the linearized model and the process can make

the controller performance worse. The load and operating point changes can give a model mismatch in the power cycle. The PID controller with a Smith predictor is recommended.

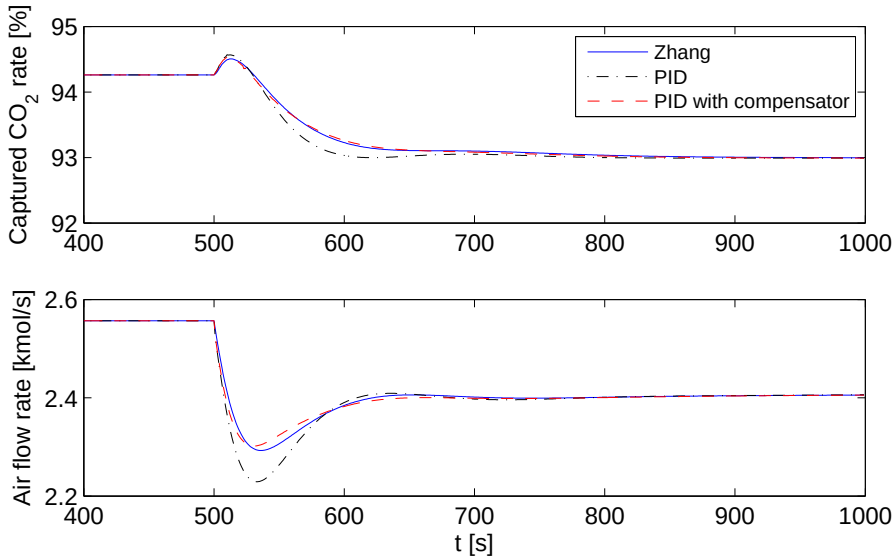

Figure 3.15: Setpoint tracking of different controllers.

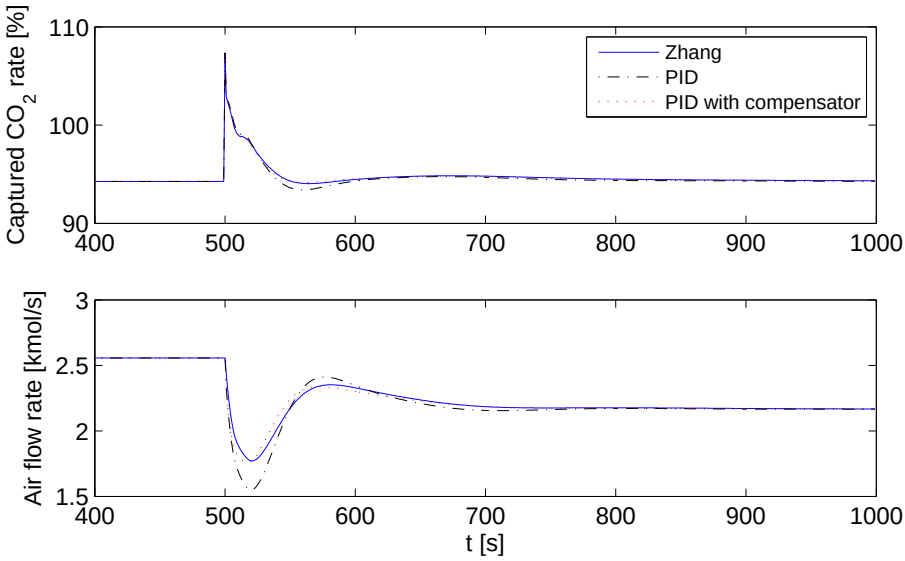

Figure 3.16: The comparison of responses to NG flow rate change.

To compensate the disturbance caused by load changes, the dynamic responses from a load change to captured CO_2 rate is identified. The chosen model structure is a third order transfer function.

$$G_d = k_d \frac{(T_{dz}s + 1)}{(T_{d1}s + 1)(T_{d2}s + 1)(T_{d3}s + 1)} \tag{3.41}$$

Figure 3.17 shows the dynamic response of a load step change and the identified model when all the other control loops are closed. Here we ignore the immediate response within the first two seconds, which is due to the NG and steam flow rate changes. This is impossible to compensate for by the air flow rate, which has a much slower response.

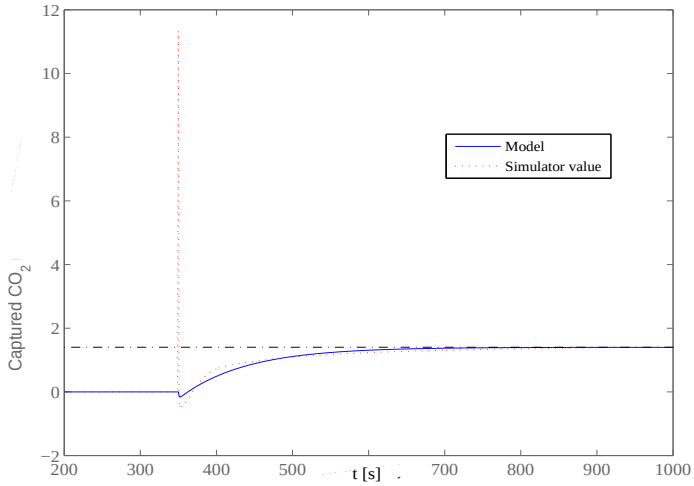

Figure 3.17: Model approximation of the air flow rate to the captured CO_2 rate.

The feedforward controller is given by (3.43)

$$H_{ff} = \frac{G_d}{G_l} \tag{3.42}$$

$$\approx \frac{k_d}{k} \frac{(1 + T_1 s)(1 + T_2 s)}{(T_{d1}s + 1)(T_{d2}s + 1)(T_{d3}s + 1)} \tag{3.43}$$

Since there is a positive pole in the process model, using (3.42) directly cannot give a stable result. The results show that $T_z \approx T_{dz}$. Hence the term $(1 - T_z s)$ in (3.36) is canceled by $(T_{dz}s + 1)$ in (3.41).

This feedforward controller is implemented into the HMR power cycle with all the other control loops closed. Figure 3.18 shows that this controller gives a better control of the captured CO_2 rate with a step load change from 100% to 90%.

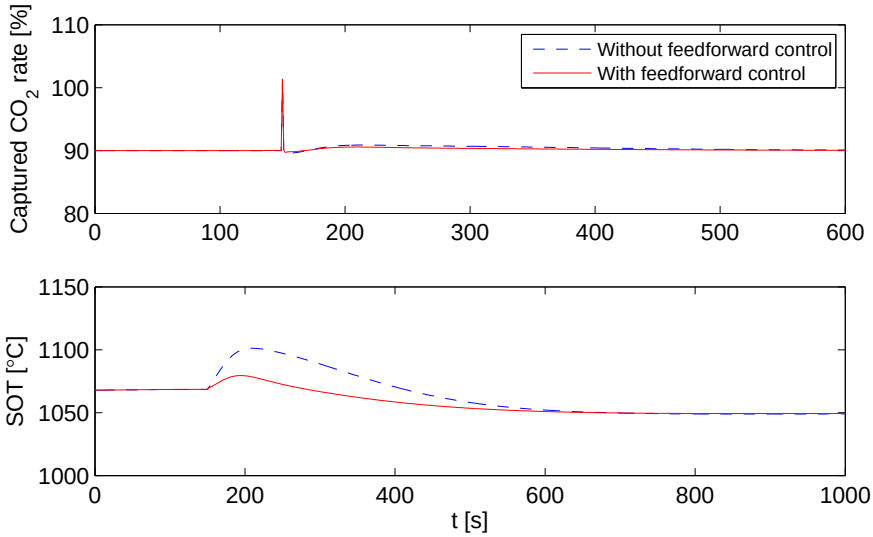

Figure 3.18: Feedforward control of the captured CO_2 rate at a step change in load.

Simulation results of case 1

The dynamic responses of the analysed control loops and variables are depicted in the following figures. Figure 3.19 - 3.22 show the responses from the load changes, while Figure 3.23 - 3.26 present responses from the step change in CH_4 .

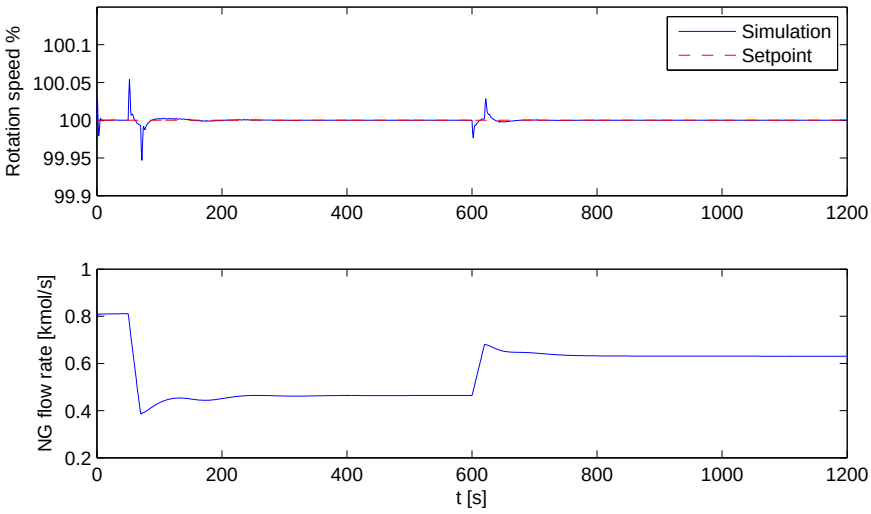

Figure 3.19: Dynamic responses of the NG flow rate, and the rotation speed in case 1.

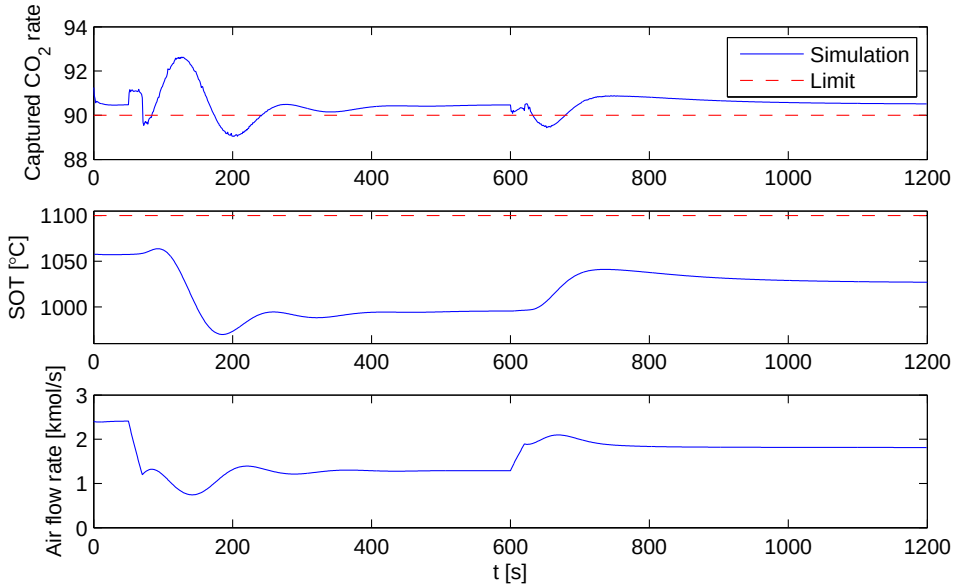

Figure 3.20: Dynamic responses of the captured CO_2 rate, SOT, and the air flow rate in case 1.

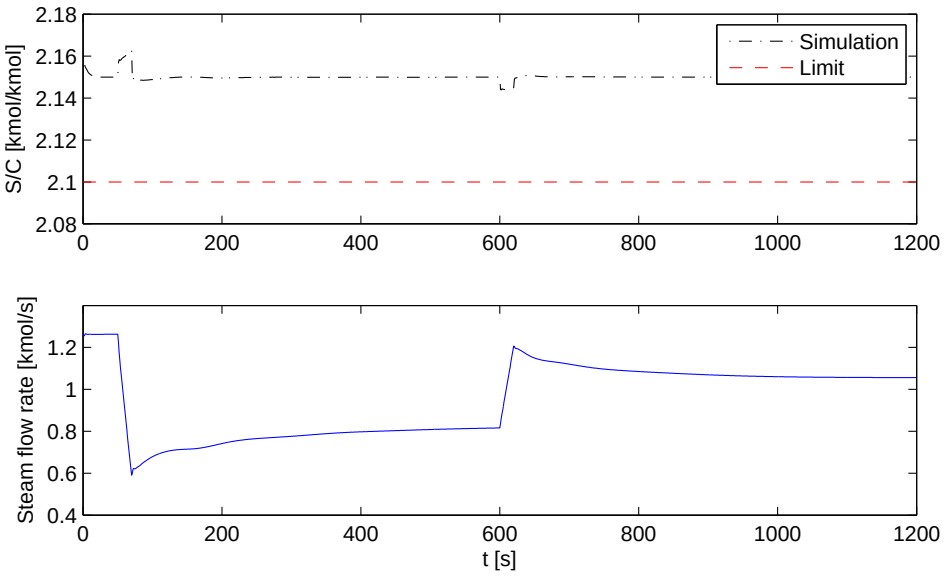

Figure 3.21: Dynamic responses of the S/C ratio, and the steam flow rate in case 1.

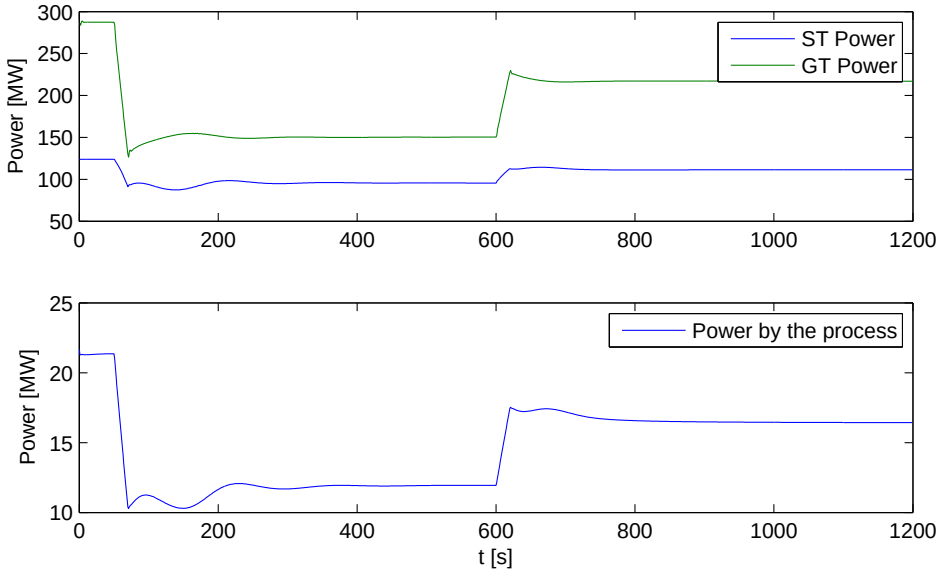

Figure 3.22: Dynamic responses of the outlet power by GT, ST and the auxiliary unit in case 1.

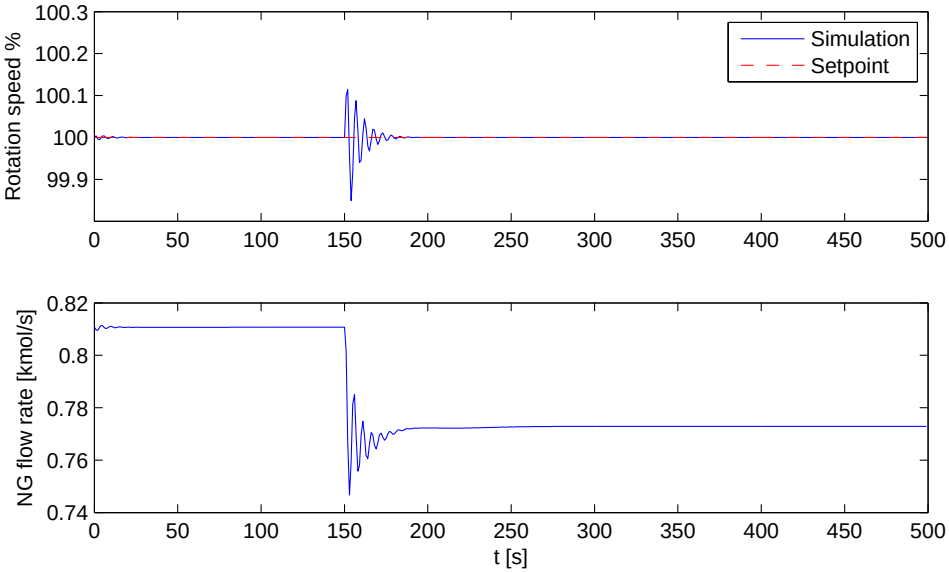

Figure 3.23: Dynamic responses of the NG flow rate, and the rotation speed with in case 1.

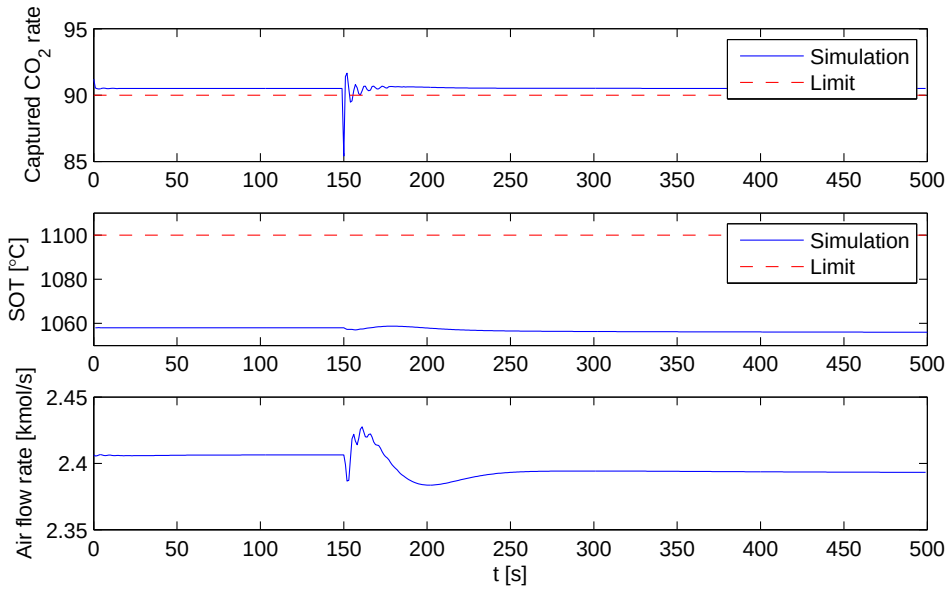

Figure 3.24: Dynamic responses of the captured CO_2 rate, SOT, and the air flow rate in case 1.

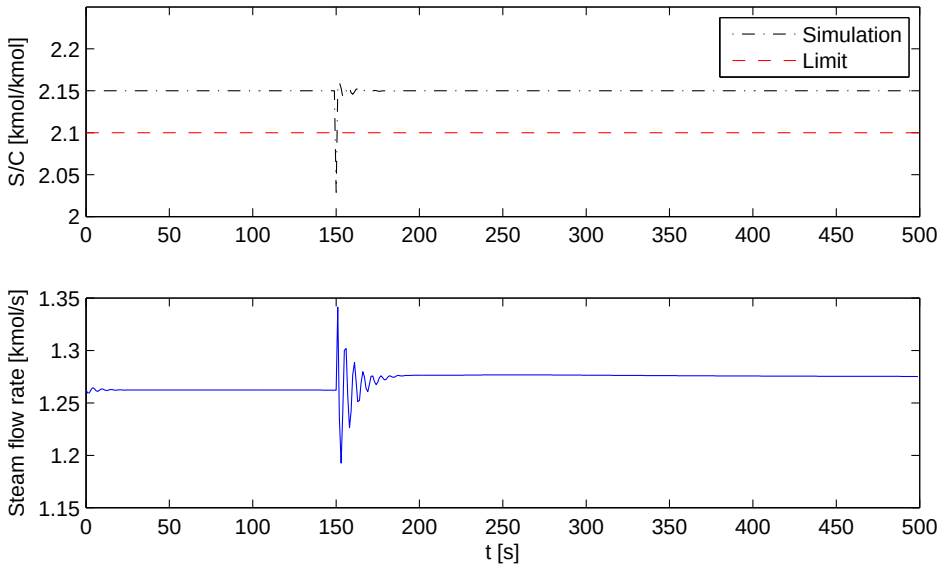

Figure 3.25: Dynamic responses of the S/C ratio, and the steam flow rate in case 1.

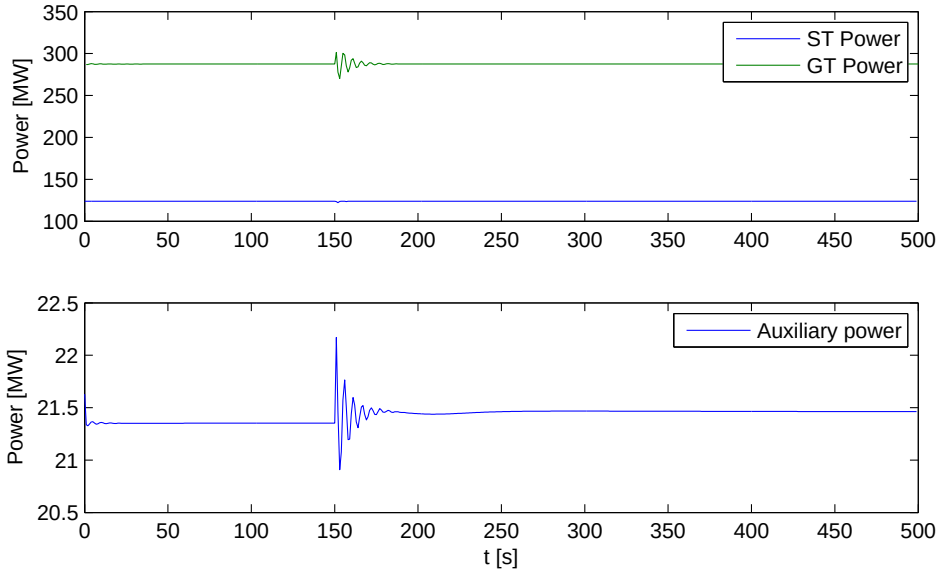

Figure 3.26: Dynamic responses of the outlet power by GT, ST and the auxiliary unit in case 1.

Simulation results of case 2

The following figures depict dynamic responses of selected control loops and variable in case 2. Figure 3.27 - 3.30 show the responses from the load changes. Figure 3.31 - 3.34 show the responses from the step change in CH_4.

All these figures demonstrate rapid response to load changes and exhibit good load-following capabilities.

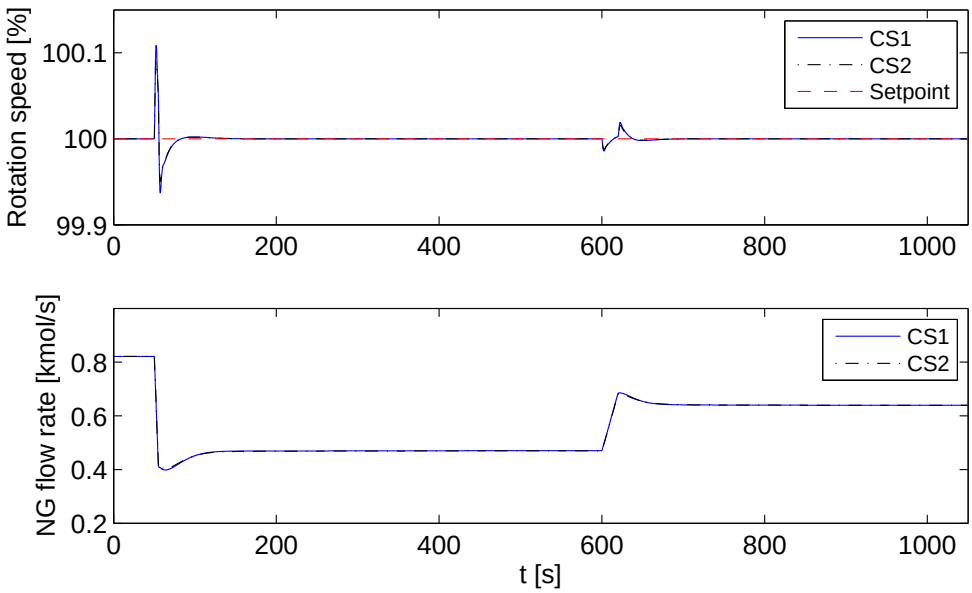

Figure 3.27: Dynamic responses of the NG flow rate, and the rotation speed in case 2.

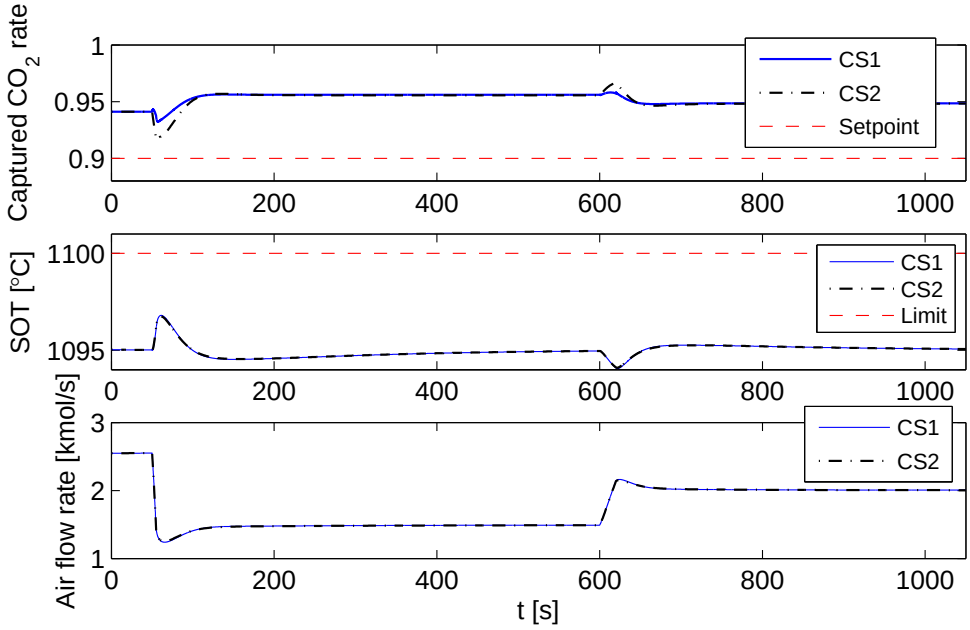

Figure 3.28: Dynamic responses of the captured CO_2 rate, SOT, and the air flow rate in case 2.

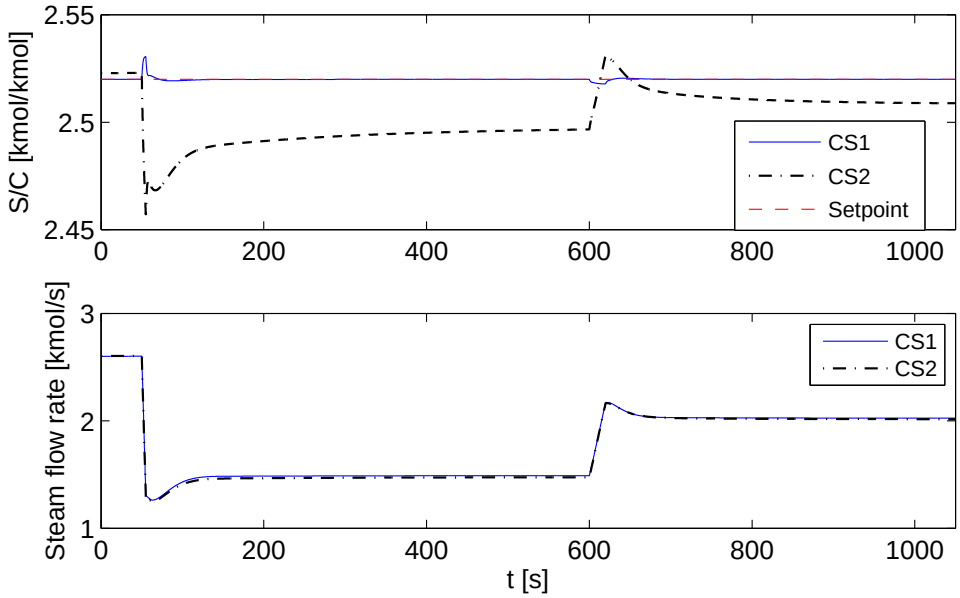

Figure 3.29: Dynamic responses of the S/C ratio, and the steam flow rate in case 2.

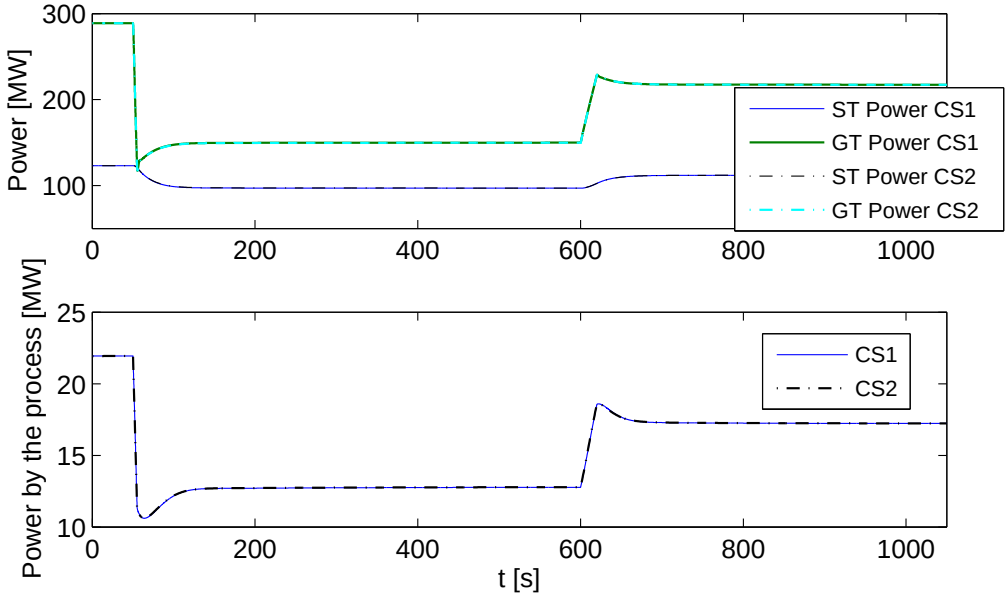

Figure 3.30: Dynamic responses of outlet power by GT, ST and the auxiliary units in case 2.

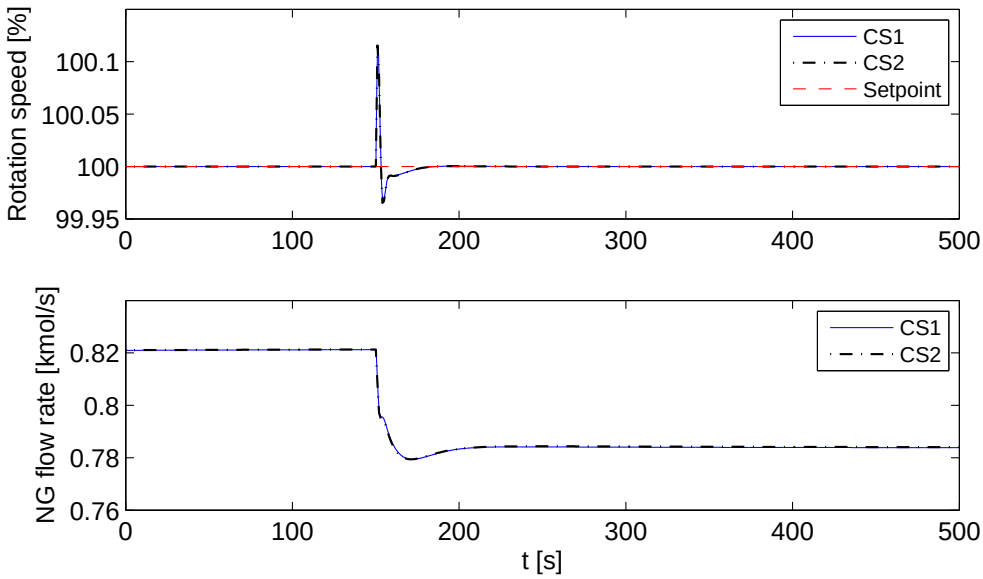

Figure 3.31: Dynamic responses of the NG flow rate, and the rotation speed in case 2.

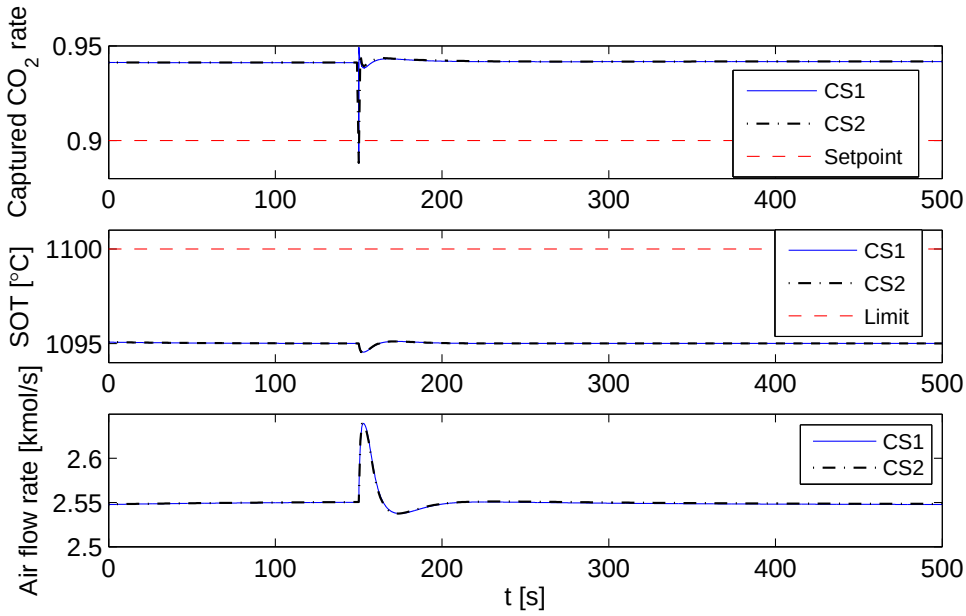

Figure 3.32: Dynamic responses of the captured CO_2 rate, SOT, and the air flow rate in case 2.

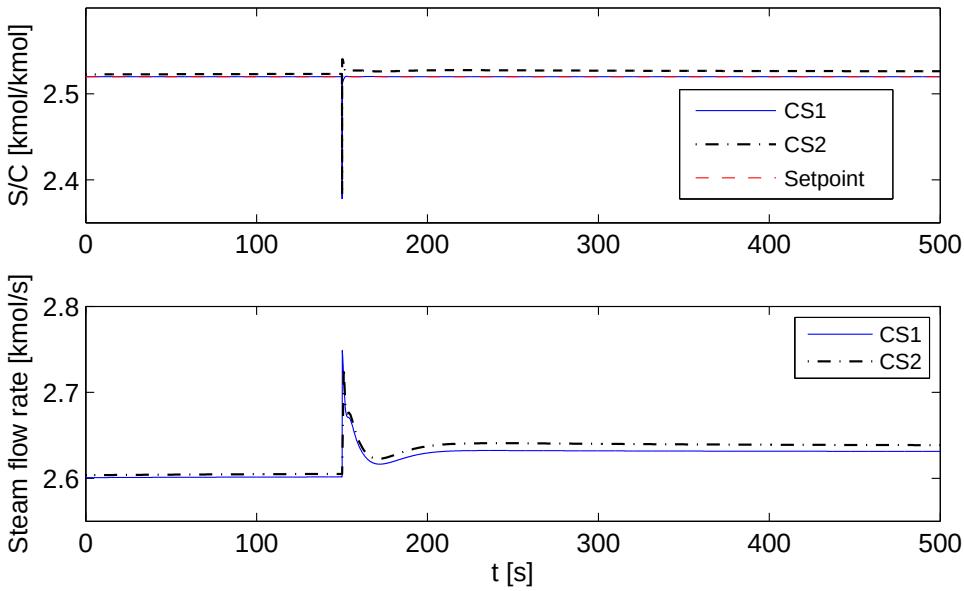

Figure 3.33: Dynamic responses of the S/C ratio, and the steam flow rate in case 2.

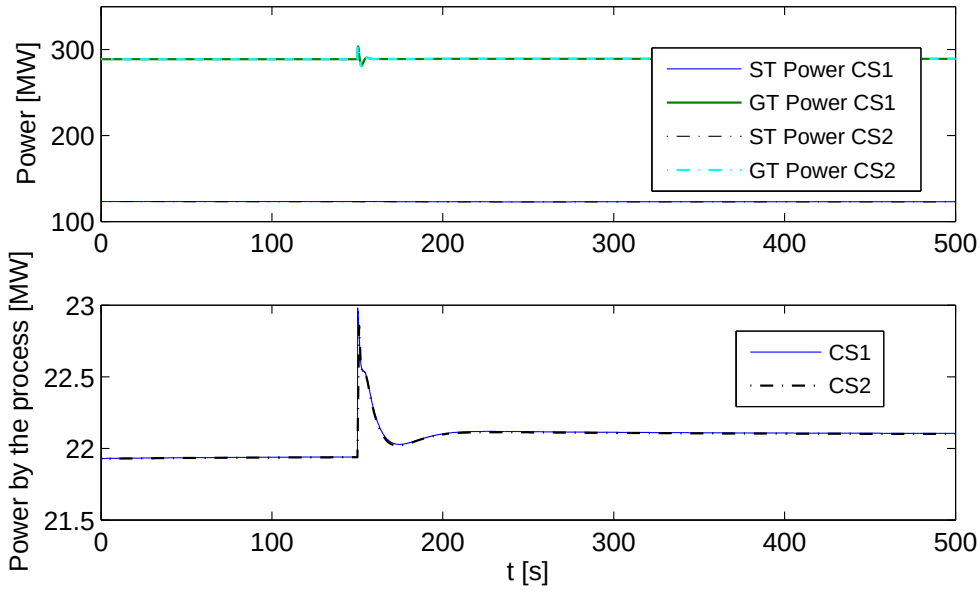

Figure 3.34: Dynamic responses of the outlet power by GT, ST and the auxiliary units in case 2.

3.5 Conclusion

A novel pre-combustion power cycle based on HMR is analysed here, and the control structure is designed in a systematic way.

To determine the control structure, an economic objective is defined, the DoFs and constraints are found, and the possible disturbances are assumed. The system is linearised at a nominal operating point. The controlled variables are selected by self-optimising control. For different algorithms and objective functions we obtain different sets of controlled variables and their setpoints. The best sets are selected based on loss analysis of the nonlinear system.

A traditional control structure is based on process analysis and engineering experiences, and it cannot guaranty the control structure is optimal. The control structure design approach applied in this study treats the whole process in a systematic way, utilize all the available information, and consider the economic profit. The designed control structure, especially when using combination of measurements, can give a small economic loss for the considered disturbances.

The control structure with well-tuned PI controllers and feedforward controllers is simulated for two cases. The results show that the designed control structure can result in a stable system and that PI controllers can make the controlled variables converge to desired values. However, some constraints may be violated during the transient period. The response of captured CO_2 rate in Figure 3.20 and Figure 3.32 show that these variables violate the constraints for large and rapid disturbances. These violations could damage the reactor. To eliminate the disturbance violation, PI controllers with gain scheduling or an advanced controller, such as MPC, can be an option. This is treated in Chapter 4.

Chapter 4

Model predictive control of the HMR power cycle

Model predictive control (MPC) is a well-known advanced technology in process control, and it has been used for many applications since the 1980s (Rossiter, 2003). Previous studies and applications show that MPC has several advantages over a conventional controller, especially when the system has many constraints.

The dynamic simulation in Chapter 3 reveals that constraint violations may be encountered during operation of the HMR power cycle. Therefore, an MPC controller may be used to handle the constraints systematically.

In this chapter, background theory of MPC is first introduced. Then, some selected control loops in the control structure of HMR power cycle is replaced with MPC controllers, and the dynamic simulation results are shown.

4.1 Background theory

MPC has several advantages compared with other traditional control methods (Rossiter, 2003). First, MPC is highly attractive for its ability to handle constraints online in a systematic way. In a plant, each constraint may represent many specifications, e.g., pressure or temperature limits of a reactor. For safety and economic reasons, the controller should maintain the variables inside the constraints. Second, MPC automatically incorporates feedforward control. MPC can hence take action before a disturbance occurs based on the knowledge of future demands. Another major advantage with MPC is that it can handle multivariable systems in a systematic way. This is made by using a model that provides information about the interactions from each input onto each output. Moreover, there are many other advantages including ease of tuning. Since the 1980s, thousands of successful applications of MPC have been reported.

Algorithms for MPC can have various forms. A description of the MPC algorithm as used in this work can be found in many books, e.g., Rossiter (2003), and Rawlings and Mayne (2009). A MPC controller contains a model, cost function, constraints, and an optimiser to calculate the inputs. The Kalman filter (KF) uses the linearised model and measurements to estimate the states. Based on these

states, a prediction model, and constraints on input and output, optimized values for the manipulated variables that track the references are calculated.

The MPC controller uses the receding horizon principle. At each time step i, the controller receives the measurements, estimates the states, and solves an optimisation problem (4.1) over a future interval $[i, ..., i+N-1]$. Generally, only the first step in the resulting optimal sequence for manipulated variables is applied to the real system. This procedure is repeated at the next time step. The optimization problem is expressed by

$$\begin{aligned} \text{Objective function} &: \min J(u, y) \\ \text{System model} &: \dot{x} = f(x, u, v, v_{un}) \\ \text{Output model} &: y = g(x, u, v, v_{un}, w_n) \\ \text{Constraints} &: h(x, u, d) \leq 0 \end{aligned} \tag{4.1}$$

Here, u are manipulated variables, y controlled and uncontrolled outputs, x states, v and v_{un} measured and unmeasured disturbances, and w_n measurement noise.

To track the output reference, we choose the objective function as a function of the control errors $y_{k+i+1} - r_{f,k+i+1}$ and the changes in manipulated variables $\Delta u_{k+i} = u_{k+i} - u_{k+i-1}$

$$\min J_k = \sum_{i=0}^{N-1} \left(y_{k+i+1} - r_{k+i+1}\right)^T Q_j \left(y_{k+i+1} - r_{f,k+i+1}\right) + \Delta u_{k+i}^T R_j \Delta u_{k+i} \tag{4.2}$$

Here, subscript k indicates current step, Q_j and R_j are weights. This can be written as

$$\min J_k = \left(y_{k+1|L} - r_{f,k+1|L}\right)^T Q \left(y_{k+1|L} - r_{f,k+1|L}\right) + \Delta u_{k|L}^T R \Delta u_{k|L} \tag{4.3}$$

where Q and R are block diagonal matrices of which the main diagonal are given by Q_j and R_j, respectively.

The following sections describe some key components in the MPC algorithm applied in this study. A dynamic model of the process is one of the most important components in MPC. Different ways to obtain the model are described in section 4.1.1. To prevent an infeasible solution to the problem, soft constraints are described in section 4.1.2. MPC requires real-time estimates of the system state. State estimation is described in section 4.1.3.

4.1.1 System models

Physical processes are generally nonlinear. MPC can be based on nonlinear models which lead to a nonlinear MPC or a set of approximate linearised models at different operating points to approximate the nonlinear systems. This leads to a linear MPC. For a system with a large number of states and a long prediction and control horizon, nonlinear MPC requires long computational time. Here the linear approach is considered.

There are several ways to obtain the linear models for MPC.

If a mathematical nonlinear model has been already developed, the linearised model (4.4) can be obtained by numerical perturbation of the nonlinear model around an operating point.

$$\begin{aligned} \bar{x}_{k+1} &= A_d \bar{x}_k + B_{du} u_k + B_{dv} v_k + v_{un,k} \\ y_k &= C_d \bar{x}_k + D_{du} u_k + D_{dv} v_k + w_{nk} \end{aligned} \tag{4.4}$$

Here

$$\begin{aligned} f_j(x) &= \frac{f_j(\bar{x}, t+\Delta t) - f_j(\bar{x}, t)}{\Delta t} \\ A_{d,ji} &= \frac{f_j(\bar{x}_i + \Delta x_i, u, v) - f_j(\bar{x}_i, u, v)}{\Delta x_i} \\ B_{du,jk} &= \frac{f_j(\bar{x}, u_k + \Delta u_k, v) - f_j(\bar{x}, u_k, v)}{\Delta u_k} \\ B_{dv,jn} &= \frac{f_j(\bar{x}, u, v + \Delta v_n) - f_j(\bar{x}, u, v_n)}{\Delta v_n} \\ C_{d,mi} &= \frac{g_m(\bar{x}_i + \Delta \bar{x}_i, u, v) - g_m(\bar{x}_i, u, v)}{\Delta x_i} \\ D_{du,mk} &= \frac{g_m(\bar{x}, u_k + \Delta u_k, v) - g_m(\bar{x}, u_k, v)}{\Delta u_k} \\ D_{dv,mn} &= \frac{g_m(\bar{x}, u, v_n + \Delta v_n) - g_m(\bar{x}, u, v_n)}{\Delta v_n} \\ i, j &= 1...nx, \;\; k = 1...nu \\ m &= 1...ny, \;\; n = 1...nv \end{aligned} \tag{4.5}$$

n_u, n_x, n_y, and n_v are the dimensions of the inputs, states, outputs, and measured disturbances, respectively.

The model obtained from linearization may contain states which have little influence on the outputs. For a large system, a reduced order model may give shorter calculation time. Methods for linear system reduction can be classified into two sets, i.e., singular value decomposition based methods, and moment matching based methods. A summary of different methods is described by Antoulas et al. (1999).

For a physical model, the term D_{du} is generally 0 or can be easily eliminated by appropriate scaling of the inputs and outputs.

To minimise the effects of unknown disturbances and noises, the state space model is expressed in the following form

$$\begin{aligned} x_{k+1} &= A x_k + B_u \Delta u_k + B_v \Delta v_k \\ y_k &= C x_k + D_u \Delta u_k + D_v \Delta v_k \end{aligned} \tag{4.6}$$

with

$$x_k = \begin{bmatrix} \Delta \bar{x}_k \\ y_{k-1} \end{bmatrix}, \;\; \Delta \bar{x}_k = \bar{x}_k - \bar{x}_{k-1} \tag{4.7}$$

and

$$A = \begin{bmatrix} A_d & 0_{nx\times ny} \\ C_d & I_{ny\times ny} \end{bmatrix},\ B_u = \begin{bmatrix} B_{du} \\ D_{du} \end{bmatrix} \tag{4.8}$$
$$B_v = \begin{bmatrix} B_{dv} \\ D_{du} \end{bmatrix},\ C = \begin{bmatrix} C_d & I_{ny\times ny} \end{bmatrix}$$
$$D_u = D_{du},\ D_v = D_{dv}$$

When physics-based models are difficult to obtain, black-box models from system identification can be used. System identification is a method to develop linear or nonlinear models from data. Many algorithms are used identifying linear and nonlinear models, e.g., the prediction error method and subspace method. The procedure of identification involves experimental design, model structure selection, selecting a criterion for fit, and model validation. The inputs and outputs of a system to be identified can be selected straightforward from the control structure design. Uncorrelated variables are preferred. The experimental region should be the same as the operating region. The sets for each input which is used to approximate the nonlinear model can be defined based on some grid over the experimental region. For a deterministic system, noise is not present in the signals, and only one experiment is needed for one input set (Ljung, 1998).

The identification could be based on the open loop system or closed loop system. For an open loop system, the physical properties, e.g., the model order, the response time, and the gain, can be observed directly from a step response. Step changes of each input at each operating point give sufficient information for identification of a linear system. Otherwise, periodic inputs, e.g., filtered Gaussian white noise, and random binary signals, are proved to be informative (Ljung, 1998). If the system is unstable or violates the constraints when applying binary inputs, the closed loop approach with simple controllers, e.g., PI, or feedforward in part or all the loops, can be applied. The closed loop system can be identified in three ways, i.e., the direct approach which uses the actual input and outputs from the open loop system, the indirect approach which identifies the system from references to outputs, and the joint input-output approach which considers u and y as the system outputs. The PI controllers can cancel the noise term in the first approach, but for a deterministic system which does not need a noise model, a direct approach may be used.

There are mainly three sets of model structures used in identification applications, i.e., transfer function models, input-output polynomial models, and state space models. Different methods can be used to identify these models

1. Low order models can be identified from analysing the Bode and time plots of step responses. A model up to three order can be easily identified.
2. The prediction error method is one of the most widely used for identifying input-output polynomial models. The principle is to minimize the error between the one step ahead prediction and the experiments data. The algorithm is described by Ljung (1998).
3. The subspace method for used in identifying state space models. The general approach of subspace identification is first to estimate the states by a Kalman filter from inputs and outputs, and then the system matrix can be identified

through a linear least squares problem. More information about subspace identification can be found from Overschee and Moor (1996).

The model used in a general MPC controller cannot handle the direct feedthrough term D_u in (4.6). However, D_u may appear in the linearised models and black-box models. There are several ways to eliminate the direct feedthrough term.

1. Add a small artificial delay to the inputs. The state space model with a input delay can be written as

$$\begin{aligned} \dot{x}_{ud} &= -\begin{bmatrix} 1/T_{ud} & & 0 \\ & \ddots & \\ 0 & & 1/T_{ud} \end{bmatrix} x_{ud} + \begin{bmatrix} 1/T_{ud} & & 0 \\ & \ddots & \\ 0 & & 1/T_{ud} \end{bmatrix} u \\ y_{ud} &= x_{ud} \\ x_{ud} &\in R^{n_u} \end{aligned} \tag{4.9}$$

   The delay time T_{ud} is selected to be less than the sampling time for the model. The input delay model can be augmented to the system models.

2. Treat the inputs as measurable disturbances. (4.4) can be written as

$$\begin{aligned} \bar{x}_{k+1} &= A_d\bar{x}_k + B_{du}u_k + \begin{bmatrix} B_{dv} & 0 \end{bmatrix}\begin{bmatrix} v_k \\ u_k \end{bmatrix} \\ y_k &= C_d\bar{x}_k + \begin{bmatrix} D_{dv} & D_{du} \end{bmatrix}\begin{bmatrix} v_k \\ u_k \end{bmatrix} \end{aligned} \tag{4.10}$$

3. Modify the predictive model. The predictive model is written as

$$\begin{aligned} y_{k|L+1} &= F_{L+1}\Delta u_{k|L+1} + p_{L+1} \\ p_{L+1} &= O_{L+1}x_k + H_{L+1v}\Delta v_{k|L+1} \\ F_{L+1} &= H_{L+1} \end{aligned} \tag{4.11}$$

$$O_{L+1} = \begin{bmatrix} C \\ CA \\ \vdots \\ CA^L \end{bmatrix}, H_{L+1} = \begin{bmatrix} D_u & 0 & 0 & 0 & 0 \\ CB_u & D_u & 0 & 0 & 0 \\ CAB_u & CB_u & D_u & 0 & 0 \\ \vdots & \vdots & \ddots & D_u & 0 \\ CA^{L-1}B_u & CA^{L-2}B_u & \cdots & CB_u & D_u \end{bmatrix}$$

$$H_{L+1v} = \begin{bmatrix} D_v & 0 & 0 & 0 & 0 \\ CB_v & D_v & 0 & 0 & 0 \\ CAB_v & CB_v & D_v & 0 & 0 \\ \vdots & \vdots & \ddots & D_v & 0 \\ CA^{L-1}B_v & CA^{L-2}B_v & \cdots & CB_v & D_v \end{bmatrix}$$

4.1.2 Soft constraints

To prevent the MPC controller from entering the unfeasible region, e.g., the region with constraints violations, soft constraints are used (Kerrigan and Maciejowski,

2000). Define slack variables w_S, and the objective function becomes

$$\begin{aligned}\min J_k &= \left(y_{k+1|L} - r_{k+1|L}\right)^T Q \left(y_{k+1|L} - r_{k+1|L}\right) + \Delta u R \Delta u_{k|L} + w_S^T Q_S w_S \\ &= \begin{bmatrix} \Delta u_{k|L} \\ w_S \end{bmatrix}^T \underbrace{\begin{bmatrix} H & 0 \\ 0 & Q_S \end{bmatrix}}_{\bar{H}} \begin{bmatrix} \Delta u_{k|L} \\ w_S \end{bmatrix} + 2 \begin{bmatrix} f & 0 \end{bmatrix} \begin{matrix} \Delta u_{k|L} \\ w_S \end{matrix} + J_0\end{aligned} \tag{4.12}$$

Here Q_S contains tuning parameters. A larger element value in Q_S gives higher weight to the violation of output constraints.

The constraints become

$$\begin{aligned} D\begin{bmatrix} u & x \end{bmatrix}' &\leq d \\ D_y y + \alpha w_S &\geqslant d_{y,\min} \\ D_y y - \alpha w_S &\geqslant d_{y,\max} \\ w_S &\geqslant 0 \end{aligned} \tag{4.13}$$

α is a tuning parameter. A larger α allows a lower weight in Q_S to obtain the same effect on constraints handling. The condition number of $\bar{H}$ defined by $\left\|\bar{H}\right\| / \left\|\bar{H}^{-1}\right\|$ is then adjusted accordingly. This is an advantage since for some QP solvers, since a low condition number gives high accuracy.

4.1.3 State estimation

MPC requires real-time estimation of the system state when using state space models. In many cases, the complete state vector is not easy to measure, so state estimation is used together with MPC. State estimation determines the underlying behaviour of the system at any point in time by using all possible information, e.g., models, and measurements.

The Kalman filter (KF) is a well-known tool used to solve estimation problems. KF estimation includes a model to predict the behaviour of the system. Measurements are used to update the prediction and find the most likely state values that produce the observed system behaviour. The Kalman filter has proven to be the best solution for linear, unconstrained systems (Simon, 2006). The following outline of the KF estimation is referred from (Simon, 2006).

Consider a dynamic model with process disturbance and noise

$$\begin{aligned} \bar{x}_{k+1} &= A_d \bar{x}_k + B_{du} u_k + B_{dv} v_k + v_{un,k} \\ y_k &= C_d \bar{x}_k + w_{n,k} \end{aligned} \tag{4.14}$$

Here, a discrete-time formulation is used. The noise processes $w_{n,k}$, $v_{un,k}$, are white, zero-mean, uncorrected, and have known covariance matrices Q_{cov} and R_{cov}, respectively

Define

$E[x_k]$: expected value of a random variable x_k
$E[x_k|y_1...]$: the conditional expectation of x_k given $y_1, y_2....$
$E[(x_k - E(x_k))(x_k - E(x_k))^T]$: the variance of a random variable x_k.
A priori estimate $\hat{x}_k^-$: estimation of x before including the measurement y_k at time k

$$\hat{x}_k^- = E[x_k|y_1, y_2, ..., y_{k-1}] \tag{4.15}$$

A posteriori estimate $\hat{x}_k^+$: estimate of x after including the measurement y_k at time k

$$\hat{x}_k^+ = E[x_k|y_1, y_2, ..., y_k] \tag{4.16}$$

The corresponding covariances of the a priori and a posteriori estimates are

$$p_k^+ = E[(x_k - \hat{x}_k^+)(x_k - \hat{x}_k^+)^T] \tag{4.17}$$

$$p_k^- = E[(x_k - \hat{x}_k^-)(x_k - \hat{x}_k^-)^T] \tag{4.18}$$

The Kalman gain and estimated states are calculated by the following steps

1) Initialisation.

The initial values for the states and the covariance matrices are given by

$$\begin{aligned} \hat{x}_0^+ &= E[x_0] \\ P_0^+ &= E[(x_0 - \hat{x}_0^+)(x_0 - \hat{x}_0^+)^T] \end{aligned} \tag{4.19}$$

2) A priori state estimate.

Propagate the state, covariance and outputs through the model.

$$\begin{aligned} \bar{x}_{k+1} &= A_d \bar{x}_k + B_{du} u_k + B_{dv} v_k \\ P_k^- &= A_d P_{k-1}^+ A_d^T + Q_{cov} \\ y_k &= C_d \bar{x}_k \end{aligned} \tag{4.20}$$

Calculate the Kalman gain.

$$K_k = P_k^- C_{dk}^T (C_{dk} P_k^- C_{dk}^T + R_{covk})^{-1} \tag{4.21}$$

3) A posteriori state estimate.

Update the states after the measurements are received at the current time step

$$\hat{x}_k^+ = \hat{x}_k^- + K_k(y_k - \hat{y}_k) \tag{4.22}$$

The posterior covariance estimation can be updated by

$$P_k^+ = (I - K_k A_{dk}) P_k^- (I - K_k A_{dk})^T + K_k R_{covk} K_k$$

4.1.4 Implementation

The MPC controllers with KF are implemented in MATLAB by using function 'quadprog' to solve the quadratic programming problems.

4.2 MPC design for the HMR power cycle

MPC controllers with state estimation are implemented in the HMR power cycle to improve the transient performance and to handle the constraints. Figure 4.1 and Figure 4.2 show the flow sheet of the HMR power cycle with MPC controllers for control structure 1 and 2, respectively. A detailed description of the process can be found in Chapter 2.

The controllers for the GT are replaced by a two input-two output MPC controller (MPC1) in both cases. MPC controllers can estimate the TIT and prevents constraints violation. A control structure for MPC1 is shown in Figure 4.3. TIT is a key variable in the GT. A TIT value beyond the design specification will damage the GT. However, TIT cannot be measured. In some GTs, turbine exhaust temperature (TET) is used as the controlled variable instead. Here, we use a KF to estimate TIT and state constraints to keep the TIT in the range. The controlled variables are the rotation speed N_r and TET. The manipulated variables are $\dot{n}_{NG}$ and variable guide vane angle. All the states in the GT, i.e., the rotation speed, TET, molar flow rate, and pressure ratio are assumed to be measured. MPC1 uses a linear dynamic model which means that it solves a quadratic programming problem online to compute the control input (the fuel flow rate from BT and VIGV).

In control structure 2, a single input single output MPC controller (MPC2) is used to control SOT.

The HMR reactor is the critical part of the power cycle. Precise control of this reactor can increase the high efficiency of CO_2 capture and avoid damage. This reactor has three inputs, i.e., the flow rate of air $\dot{n}_{Air}$, steam $\dot{n}_{Steam}$, and pre-reformed NG $\dot{n}_{NG.PR}$ can be manipulated. The gas turbine uses $\dot{n}_{NG.PR}$ to maintain the rotation speed. From the control structure design in Chapter 3, $\dot{n}_{Steam}$ is manipulated by the S/C ratio. Hence, $\dot{n}_{Air}$ is left to be the degree of freedom for control of SOT.

SOT is one of the most important parameters in this reactor. A higher temperature gives a higher CO_2 capture rate, and the reactor will be damaged if the temperature is beyond 1100 ^{o}C. PI controllers may give such a result, see Figure 3.20. MPC can handle the constraints and thus is used to replace the PI controller.

In MPC2, SOT is the controlled variable, and the air flow rate $\dot{n}_{Air}$ is the manipulated variable. The number of states is 14, and among these states, SOT, is found to be essential to estimate the full states used for control. Power load changes which may be frequent during operation are considered as disturbance. There may also be some unmeasured disturbances, e.g., methane and steam concentration changes or membrane leakage, which are not considered here.

In control structure 1 described in Chapter 3, control of C_{CO_2} is suggested instead of SOT, and S/C instead of a combination of several measurements. To take care of the constraint violation of S/C ratio and C_{CO_2}, different control strategies are tested and compared.

The relation between the air flow rate and steam flow rate to captured C_{CO_2} rate and S/C ratio involves nearly all the components in the plant. It is difficult to calculate a good linear model from linearization because of the large number of states, the different sampling times, and nonlinearities. Hence, black box models

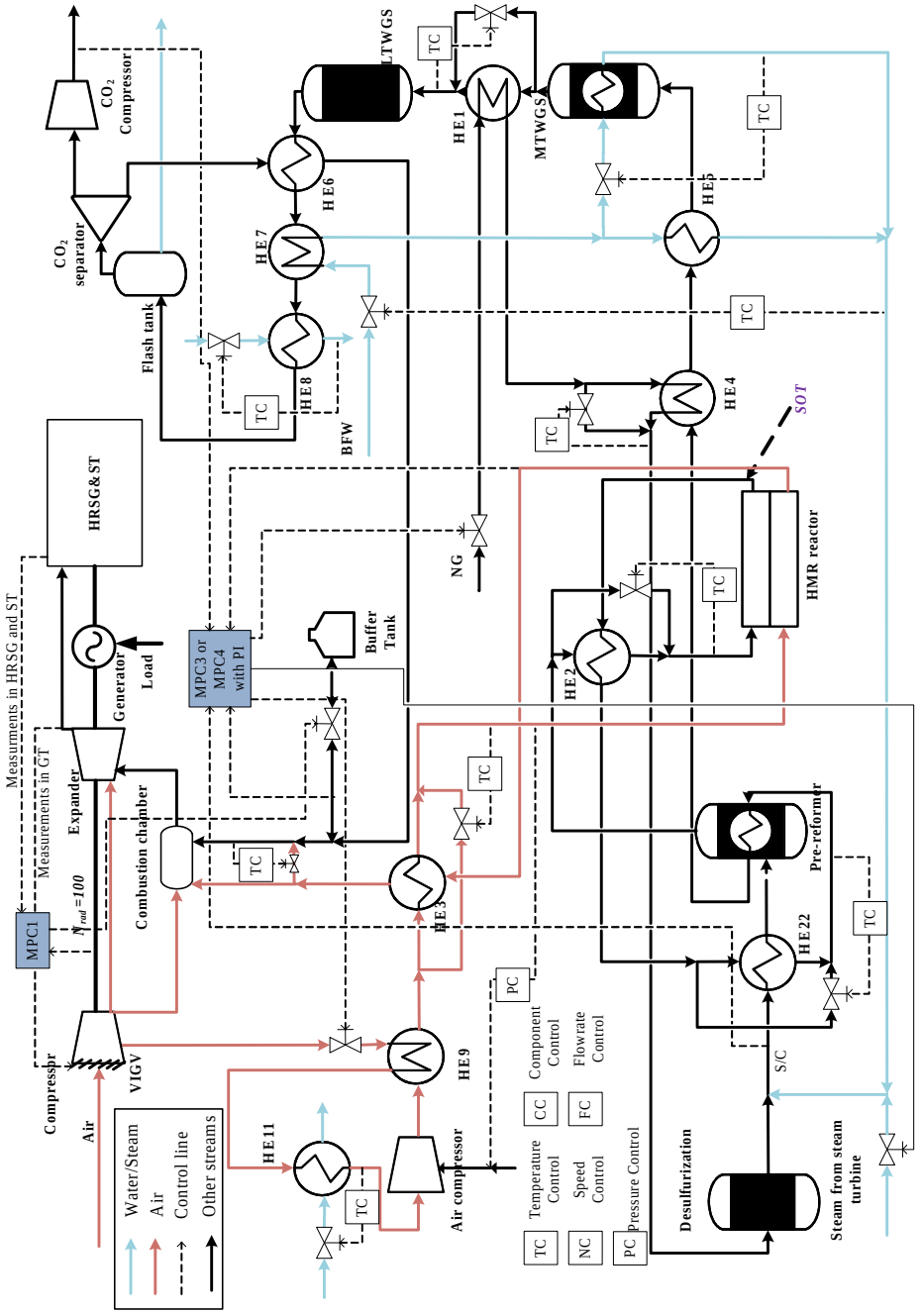

Figure 4.1: Control structure with MPC controllers for the HMR power cycle, case 1.

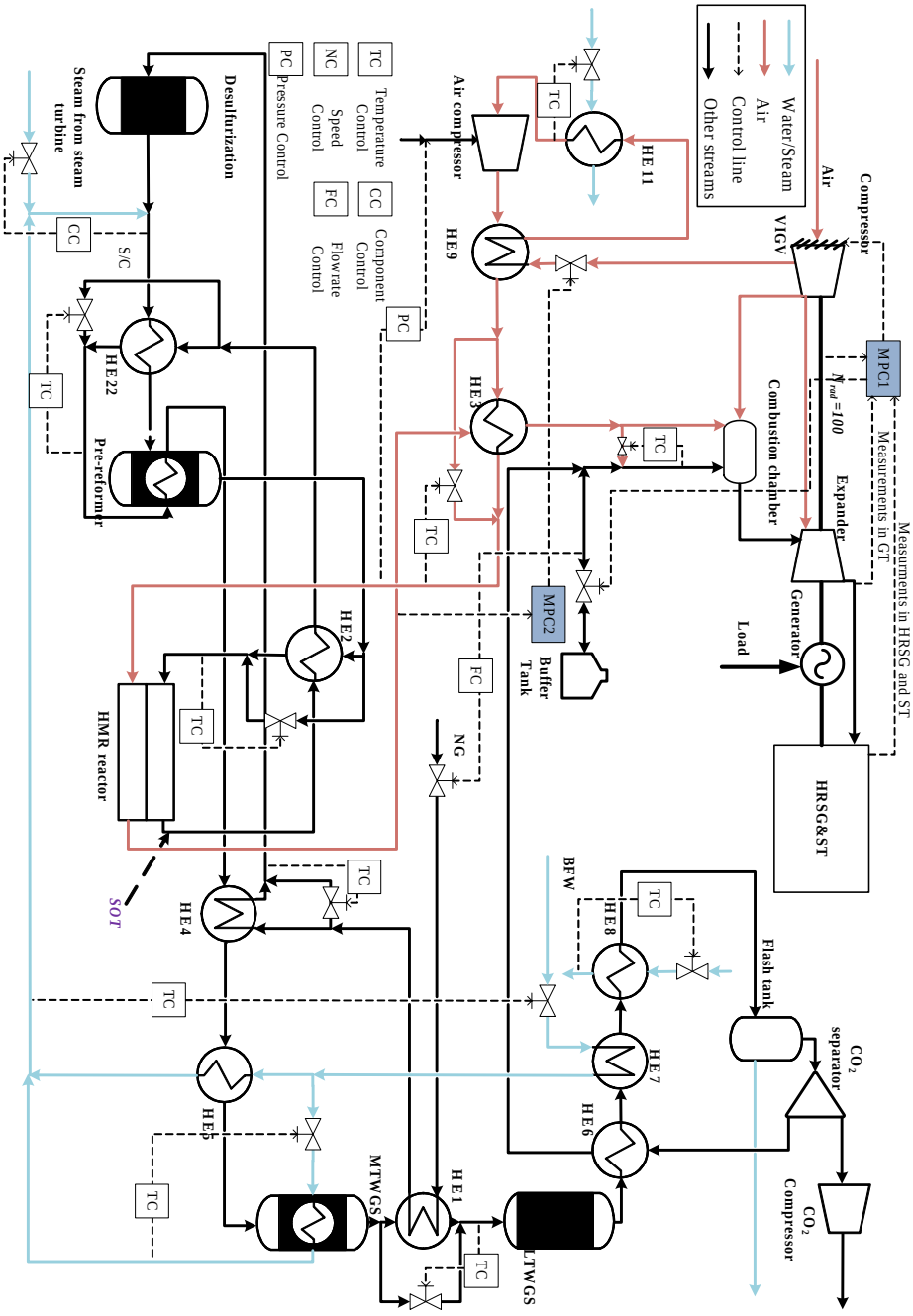

Figure 4.2: Control structure with MPC controllers for the HMR power cycle, case 2.

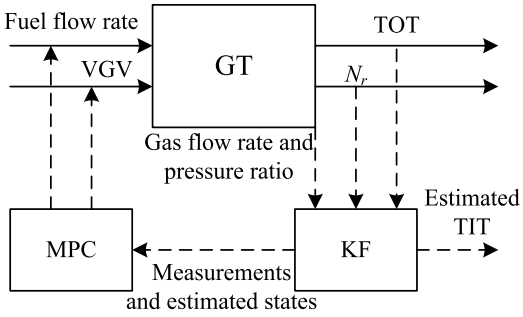

Figure 4.3: MPC controller for the GT.

from system identification are used. The structure of the model can be nonlinear models, or a set of linear models identified at different loads. A nonlinear model requires more experiments and good guesses of the model structure, and a complicated controller. A set of linear models which is easier to implement is applied here. The system is divided into several operating regions by the load, and a linear model is identified based on the step responses inside each region.

The system has several variables which can be used as manipulated variables, i.e., steam flow rate $\dot{n}_S$ and air flow rate $\dot{n}_{Air}$. In addition, manipulating the flow rate of nature gas flow rate $\dot{n}_{NG}$ gives one more freedom to control the dynamic behaviour. The outputs to be controlled are fuel flow rate from the buffer tank, S/C ratio and C_{CO_2}. In addition, SOT, which may violate the constraint, is considered as one output. Assume that one disturbance, load change P_L, can be measured. To obtain more freedom for control, a system with all 3 inputs and 4 outputs is identified and the corresponding MPC (MPC3) is designed. Further, another MPC controller (MPC4) with one manipulated variable ($\dot{n}_{Air}$) and two controlled variables, (C_{CO_2} and T_{SOT}), are developed. The other outputs are controlled by PI controllers as shown in Figure 4.4.

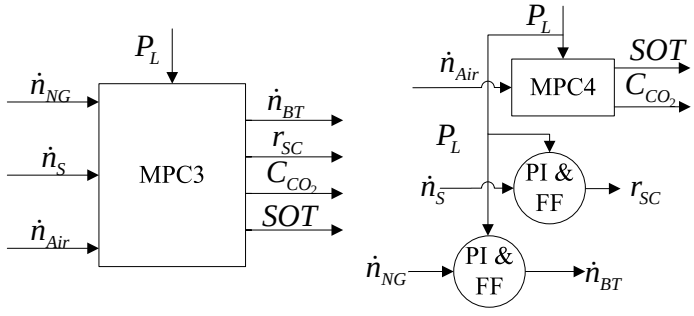

Figure 4.4: Two MPC controllers used in control structure case 1.

The procedure shown in Figure 4.5 is implemented to design the MPC controllers.

First, the whole operating range is divided to n regions by the value of the load. A set of experiments is made where each control input and disturbance is

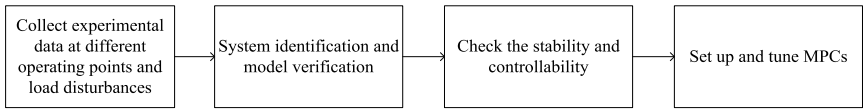

Figure 4.5: Design procedure of MPC controllers.

perturbed, and the output data are collected (Figure 4.6). The perturbations are step changes with maximum amplitude in the operating region to guaranty informative experiment data. The load change may jump from one point for example OP_1 to a nonadjacent point OP_n. Only using the data from OP_1 and OP_n cannot give a good prediction of the dynamic behaviour. Hence, the dynamic data from a number of intermediate points are also collected.

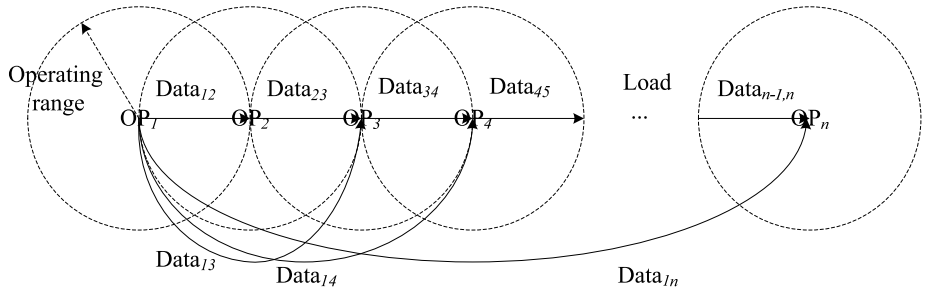

Figure 4.6: Experiment data by different operating points.

Next, the models are identified using the prediction error method. The plots of data used for identification and the outputs from the identified model at the nominal operating point are shown in Figure 4.7. Comparison of a validation set of data and the model are also shown in Figure 4.7. The first upper four rows of plots show the dynamic responses of outputs, i.e., fuel flow rate from buffer tank, S/C ratio and C_{CO_2} and SOT. The three inputs and load changes are shown in the last row. The plots show that the identified model captures the main dynamics of the system and gives a good estimation.

Identification of the other models follows the same procedure and the orders of the models are selected to give at least 95% of the output variation which is calculated by (4.23). Here, y_{md} is the output calculated by the identified model, and y_{data} is the output from the nonlinear simulation model.

$$\alpha = 1 - \frac{\|y_{md} - y_{data}\|}{\|y_{data} - mean(y_{data})\|} \tag{4.23}$$

The identified models are input-output models and are converted to state space models. The number of states is reduced by singular value decomposition. All the identified models are stable, controllable and observable.

The MPC controllers are tuned in the final step of the design procedure.

During online operation, the MPC controller switches between the various models depending on the operating point. The decision variable is the load. At a load change, a new model is selected from a database containing the models based on the

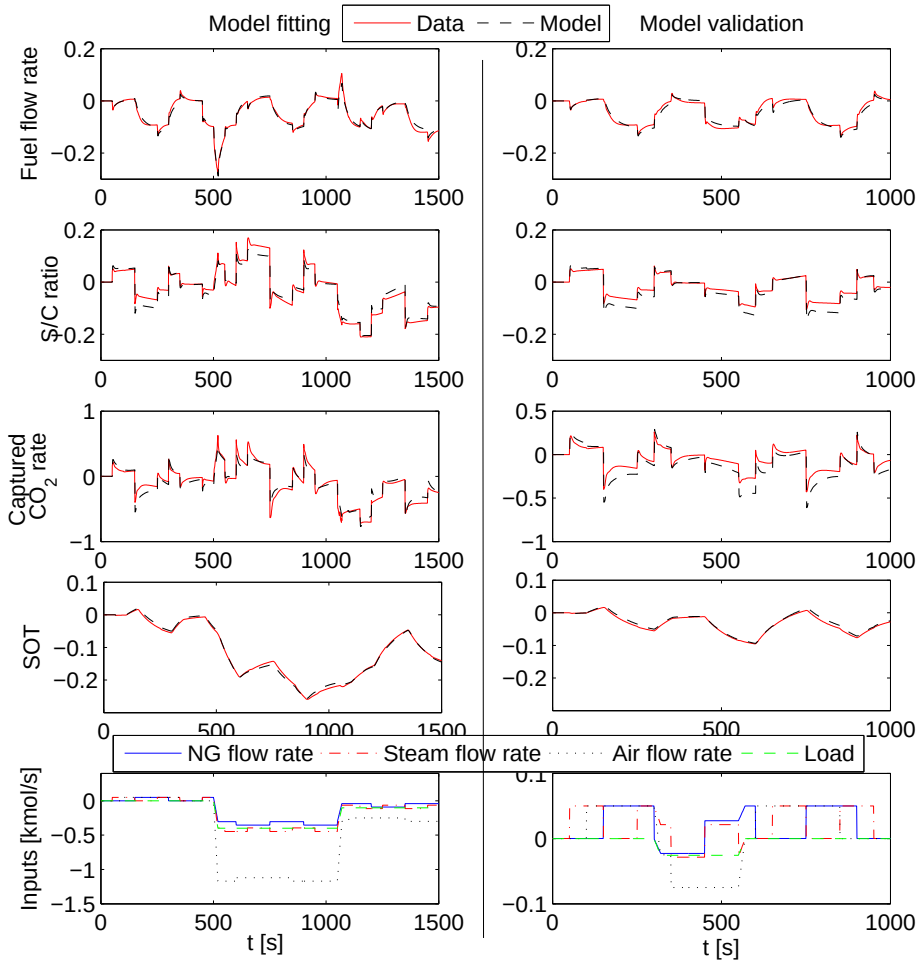

Figure 4.7: Model identification and validation.

amplitude of the load change and the current operating point as shown in Figure 4.8.

4.2.1 Tuning of MPC controllers

This section describes tuning of the MPC controllers.

1. Control of the combined cycle (MPC1).

   The parameters for MPC including KF are shown in Table 4.1. The rotation speed is the most important variable and it should be tightly controlled to the setpoint. Hence, a large weight is applied on this variable in the MPC. The

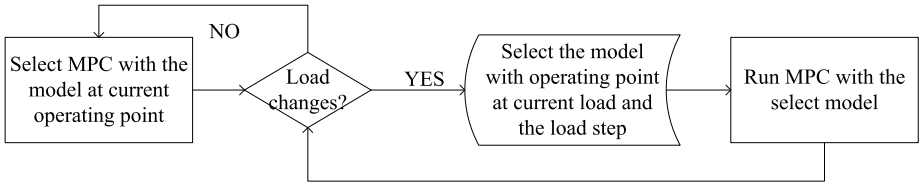

Figure 4.8: Model selection of the MPC controllers.

weight on the state constraint for TIT is important for avoiding constraint violation. Because of the model error, a large weight on the measurements is applied in the KF.

Table 4.1: MPC parameters for the SOT control loop.

Parameter	Value	Description
t_s	$0.2s$	Sampling time
Q_j	$diag$[100 1]	Weight on each measurement
R_j	$diag$[1 1]	Weight on each input
Q_S	10	Weight on the state constraint TIT
R_{cov}	50	Weight on the Kalman gain
t_P	$10s$	Prediction horizon

Two single input-single output PI controllers and two MPC controllers, i.e., MPC with one single model and multiple models, are compared in Figure 4.9. To investigate the control performance, the load is reduced from 100% to 60% during a period of 10 seconds. The dynamic responses of the rotation speed, TET, TIT, fuel flow rate to CC, and VIGV are depleted in this figure. The plots show that all the controllers can give good setpoint tracking. The PI controllers control each variable independently and give a tighter control of TET than the MPC, which give a smoother control of the rotation speed. Moreover, since MPC can estimate TIT, it can handle the constraint on this variable. The figure also indicates that MPC with multiple models by using the method described in section 4.2 can give a more accurate estimation of TIT than MPC with one model. Hence, this approach is suggested for the system.

2. Temperature control of the HMR reactor (MPC2).

   The MPC parameters are shown in Table 4.2. A large weight of the measurement in MPC gives tight control of SOT. Further, large weight to the constraints can avoid constraints violation. A linear model is made by perturbation. The linearised model can give an accurate estimation of the states, and a higher weight of the model (Q_{cov}) is used to reduce the effect by measurement noise.

   Step changes of inlet NG and steam flow rate are used to compare the MPC with the PI controllers from control structure design in Chapter 3, see Figure 4.10. A 30% flow rate change corresponds to a 30% load change. The plots

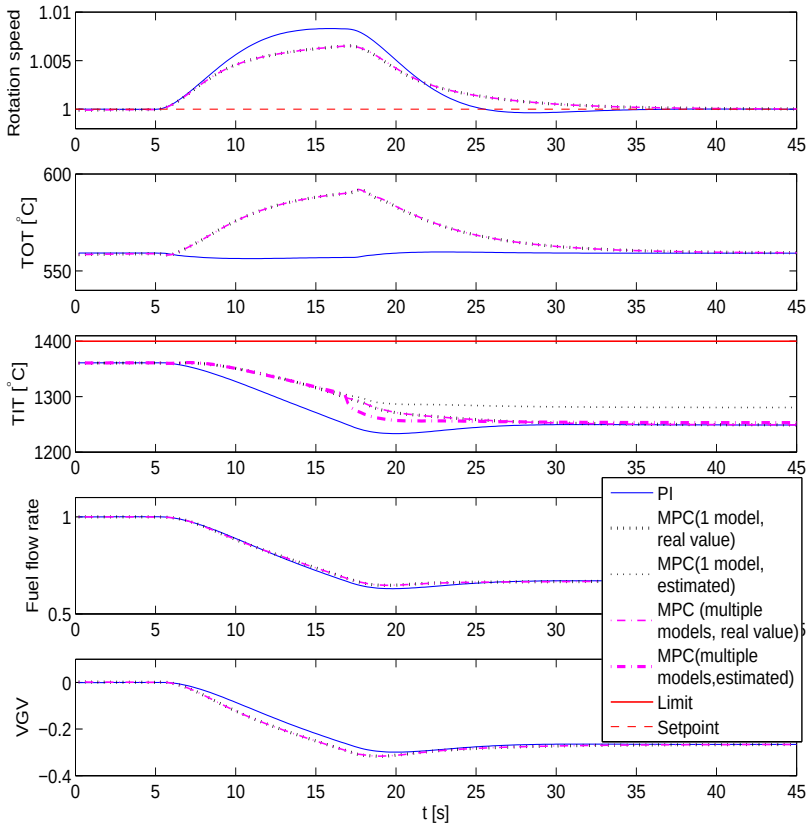

Figure 4.9: Comparison between the MPC and PI controllers for the GT.

Table 4.2: MPC parameters for the SOT controller.

Parameters	Value	Description
t_s	$1s$	Sampling time
Q_j	10	Weight on the measurement
R_j	1	Weight on the input
Q_S	100	Weight on the constraints
R_{cov}	0.5	Weight on the Kalman gain
t_P	$80s$	Prediction horizon

show that both controllers can give good performance. However, the MPC controller handles the constraints better. In this simulation, the disturbance is not measured, and the MPC controller may violate the constraints for unmeasured disturbance.

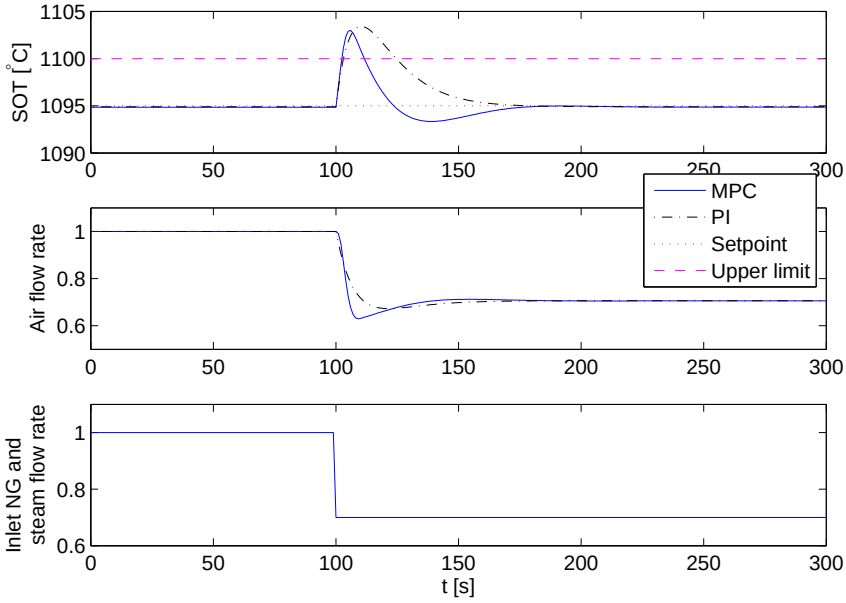

Figure 4.10: Comparison between the MPC and PI controller for the SOT.

3. Control of C_{CO_2} (MPC3 and MPC4).

   To handle the inverse responses in the air to captured CO_2 rate loop, a long prediction horizon is used. The lower limit for prediction horizon is where the sum of the impulse response coefficients has the same sign as the process gain (Bequette, 2003). A slightly longer horizon than the lower limit value is chosen in this study. The parameters of the controller are shown in Table 4.3.

Table 4.3: MPC parameters for the C_{CO_2} controllers.

Parameters	MPC3	MPC4	Description
t_s	$2s$	$2s$	Sampling time
Q_j	[100 100 100 0]	[100 0]	Weight on each measurement
R_j	[1 1 1]	1	Weight on each input
Q_S	10	10	Weight on the state constraint TIT
R_{cov}	1	1	Weight on the Kalman gain
t_P	$80s$	$80s$	Prediction horizon

The performance of the controllers with respect to a step change in the S/C

ratio from 2.15 to 2.52 at 50s and a step change of captured CO_2 rate from 90.5% to 92% at 350s are shown in Figure 4.11. These reference changes may occur during operation point changes, see Chapter 3. MPC3 gives a slower and smoother response than PI control. Moreover, the PI controller and MPC4 may result in constraint violation, e.g., captured CO_2 rate from 100s to 200s. In MPC4, the S/C reference change is an unmeasured disturbance, and the controller cannot give a dynamic response as good as MPC3.

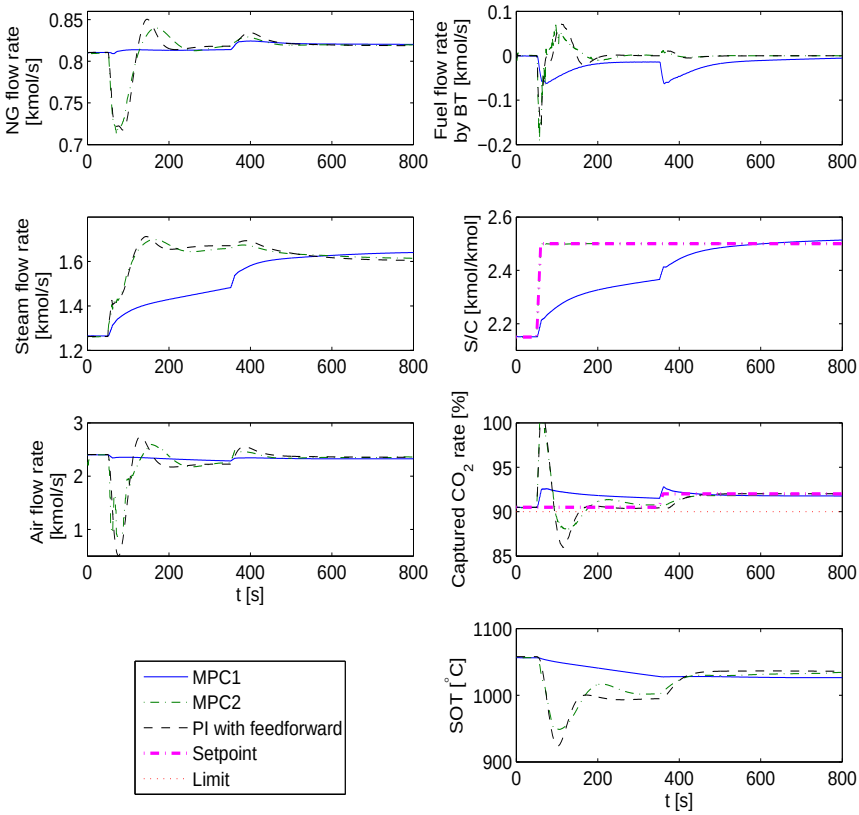

Figure 4.11: Comparison between the MPC and PI controllers with respect to S/C and captured CO_2 rate reference changes.

4.3 Simulation of the HMR power cycle

Simulation results of the HMR power cycle with MPC controllers is presented in this section.

The same load disturbances as Chapter 3, e.g., the net power load reduced from 100% to 60%, and then, increased to 80%, are applied to the whole system. Comparison between the MPC and PI controllers for control structure case 1 and case 2 as described in Chapter 3 is studied. Figure 4.12 and 4.13 show dynamic

responses for some important variables. Here, discrete time PI controllers with the same sampling time as the MPC controllers are used.

The performances of MPC3, MPC4, and PI with feedforward in control structure case 1 are shown in Figure 4.12. Captured CO_2 rate has a large overshoot due to inverse response and may below 90% when using PI controllers, whereas the MPCs give a smoother response and handle the constraint much better. A faster response of the S/C rate is observed in the case with MPC4 and PI controllers than with the MPC3. The slow dynamics are due to the trade-off between the fast response and constraint handling. The dynamic responses from MPC3 are smoother than those of MPC4 and PI. Moreover, the S/C ratio and NG flow rate from BT is controlled by PI in MPC4. Hence, MPC4 can give as tight control as PI controllers.

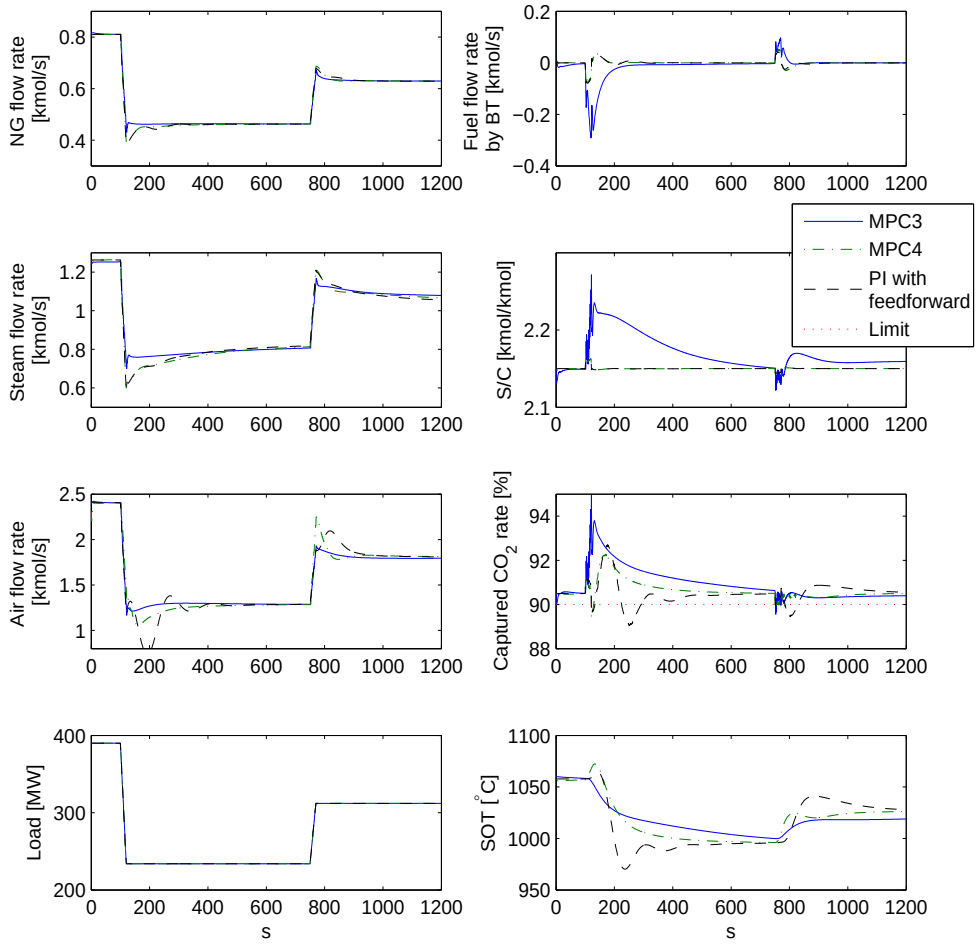

Figure 4.12: Comparison between the MPC and PI controllers with respect to load changes, case 1.

The MPC controllers in control structure 1 can significantly improve the dynamic performance of SOT as shown in Figure 4.13. The MPC controller gives a tighter setpoint tracking and prevents constraint violation.

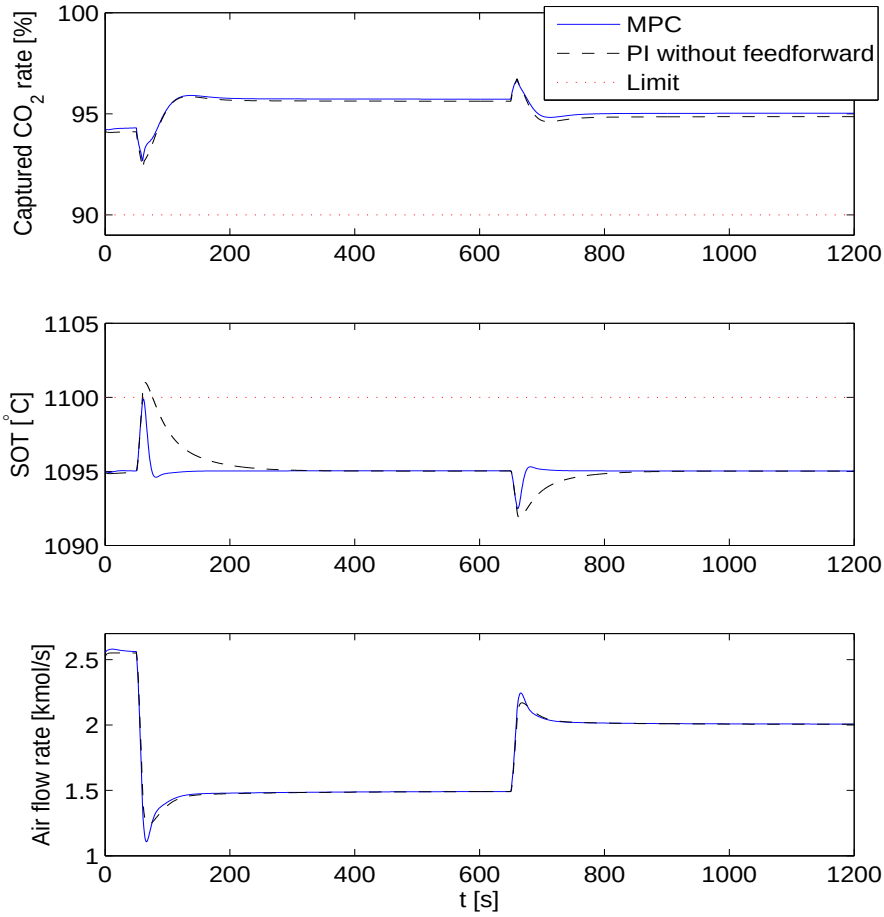

Figure 4.13: Comparison between the MPC and PI controllers with respect to load changes, case 2.

4.4 Conclusion

This chapter discusses MPC controllers with state estimation for the HMR power cycle. Because of the large number of states in the simulation model, the different response times, and the nonlinearities, a centralised MPC may be not practical for this study. Instead, decentralised MPCs together with PI controllers are used. Hence, some PI control loops presented in Chapter 3 are replaced by MPC controllers to handle the constraints.

With a higher CO_2 emission tax, SOT is a critical variable that should be controlled, since it may violate the constraints transiently. An MPC with a linearised model controlling SOT is implemented here. For lower CO_2 emission tax, it becomes more important to handle the constraints for C_{CO_2}, SOT, and S/C. MPC controllers with identified black-box models are designed to find the best solution for controlling the captured CO_2 rate.

The results show that because of the nonlinearities, the MPC controllers give a better dynamic behaviour than PI with feedforward control for given disturbances. PI with feedforward control are easy to implement and do not require much information about the system. However, they may give large overshoot or constraint violation. MPC controllers can overcome these drawbacks and provide a smoother dynamic performance. Hence, for the HMR power cycle studied here, MPC controllers are recommended above PI controllers.

Chapter 5

Benchmarking the HMR power cycle with an ATR power cycle

This chapter describes benchmarking the HMR power cycle with an ATR power cycle. First, dynamic model of the ATR power cycle which is comparable to the HMR power cycle and the model in Chapter 2 is derived. Second, some simulation results of the model are presented. Then, the control structure is designed based on the procedure described in Chapter 3. The comparison of the two power cycles is made towards the end.

5.1 Modelling and simulation of the ATR power cycle

A distributed ATR model is modified from the work by Beyer (2011). A smaller number of grid blocks to discrete the model is used in this study. The other process units use the same models and structures as described in Chapter 2.

5.1.1 A model of an ATR reactor

The ATR reactor can be divided into two parts: a combustion chamber and a catalyst bed. The mixed steam and methane from upstream first goes into the combustion chamber. Part of the methane is partially oxidized and the released heat provides energy for the SMR reactions. The outlet gas from combustion chamber goes into the catalyst bed and the natural gas is reformed to syngas.

The CC model is assumed to contain ideal gases, no heat loss, no pressure loss, homogeneous mixture, total oxygen consumption, and an instant reaction. The model is described by total mole and energy balances

$$\begin{aligned} \dot{n}_{out,i} &= \dot{n}_{in,i} + r_{POX,i} \\ \frac{dT}{dt} &= \dot{n}_{in} H_{in} + r_{POX} \Delta H_r \end{aligned} \tag{5.1}$$

Here, $\dot{n}_{out,i}$ and $\dot{n}_{in,i}$ are the outlet and inlet molar flow rate of each component i. $r_{POX,i}$ is the consumed and generated molar flow by the reactions. H is the

enthalpy, and ΔH_{react} is the enthalpy of reaction. The calculation of H_{in} and H_{react} can be found in Appendix A.

The model of the catalyst bed is a distributed model along the reactor. The conservation of mass and energy are described by

$$\frac{\partial c_i}{\partial t} = -\frac{1}{A\epsilon}\frac{\partial \dot{n}_i}{\partial z} + \frac{1-\epsilon}{A\epsilon}\sum_j r_{SMR,j} \tag{5.2}$$

$$\left(\sum_i \epsilon c_i c_{p,i} + (1-\epsilon)\rho_{cat} c_{p,cat}\right) A\frac{\partial T}{\partial t} = -\frac{\partial\left(\dot{n}_i c_{p,i} H_i\right)}{\partial z} + (1-\epsilon)\sum_j r_{SMR,j}\Delta H_{r,j}$$

Boundary conditions are

$$\left.\frac{\partial \dot{n}_i}{\partial z}\right|_L = 0 \tag{5.3}$$

$$\left.\frac{\partial\left(\dot{n}_i c_{p,i} H_{in}\right)}{\partial z}\right|_L = 0$$

Here, c_i is the molar concentration for each component, A is the cross section area, ϵ is the void fraction, $r_{SMR,i}$ is the reaction rate by steam reforming, z is the axial position and the value is from 0 to L, c_p is the heat capacity, j presents each reactions, and ρ_{cat} is the catalyst density.

The model (Nord et al., 2009) was implemented in MATLAB and verified against a steady state values from a paper by Nord et al. (2009). The parameters of the dynamic model were tuned to match the steady state operating points. Dynamic responses were validated based on available literature data. This distributed model with a reduced discretization grid (from 80 to 10 grid blocks) is used in the current ATR power cycle. This reduction in grid blocks only has a minor influence on the model behavior. Further, it reduces CPU time significantly.

5.1.2 Dynamic responses of the ATR power cycle

The dynamic responses from changes in the NG flow rate, the steam flow rate, the air flow rate at time 50s, are shown in Figure 5.1 - 5.3, respectively. This is the same as the scenario shown in Chapter 2.3.

When keeping the other inputs constant, a decrease of the NG flow rate gives the following effect on the process

- Increase of outlet temperature. This can be explained by a higher O/C ratio, which results in a higher temperature in the combustion chamber at this operating point.
- Increased fuel flow rate from the BT to maintain the net power output.
- Increased CO_2 capture rate because of a higher SOT and the increased conversion of methane.
- Increased S/C ratio.

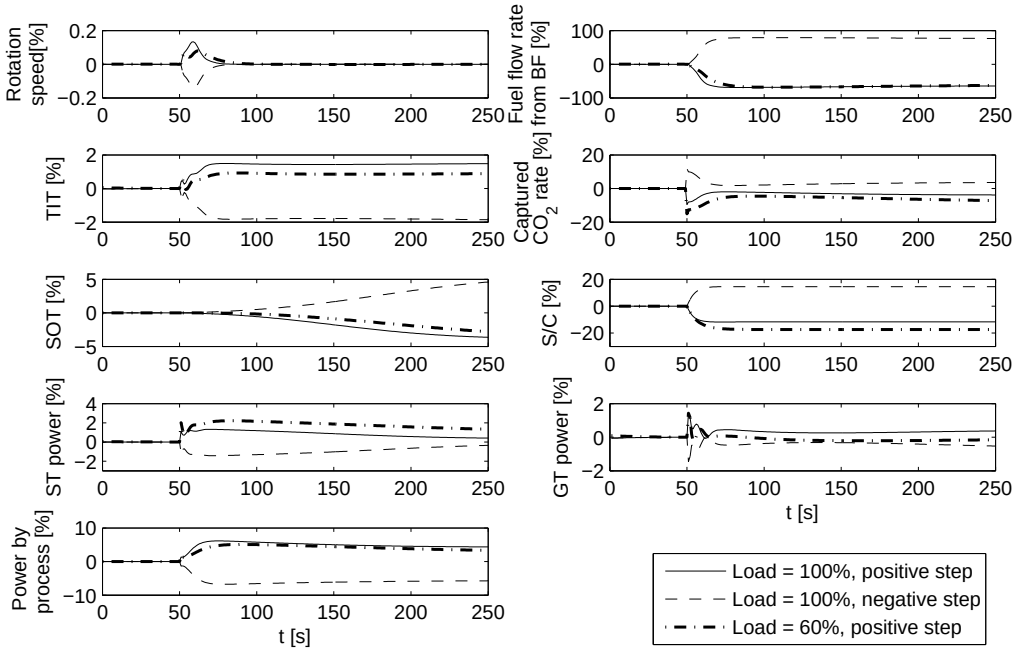

Figure 5.1: Dynamic responses from 10% NG flow rate changes at $50s$.

- Less power consumption in the process. Less CO_2 is captured and less energy is required to compress CO_2.
- Less power by the ST at first, because lower power required in the process leads to less flow rate through the GT and a decreased energy flow into the HRSG. Then the power from the ST is slowly increased because the slowly increased SOT generates more steam in the syngas cooler.

Compared to the HMR power cycle

- The ATR power cycle has different dynamic responses of the rotation speed because of the different PI gains of shaft controller.
- The ATR power cycle has similar dynamic responses of the captured CO_2 rate, SOT, and the power by the process.
- The gains to the fuel flow rate from the BT, the GT power, and the TIT are larger in the ATR power cycle. This is because, with 10% changes, the NG flow rate change in the ATR power cycle is larger than the flow rate in the HMR power cycle.
- The dynamic responses of the power by the ST is different due to the different operating condition for the HRSG and ST model. The ST in the HMR power cycle operates at maximum capacity. While in the ATR power cycle, the ST power is less than maximum power output with the same configuration. Thus, the ST power can be varied at 100% load in contrast with the HMR power cycle.

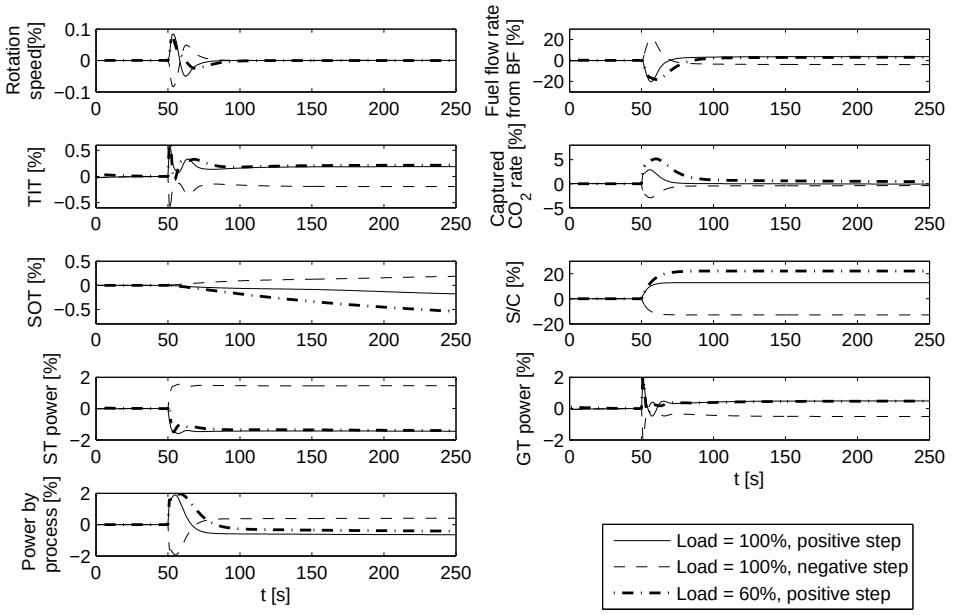

Figure 5.2: Dynamic responses from 10% steam flow rate changes at 50s.

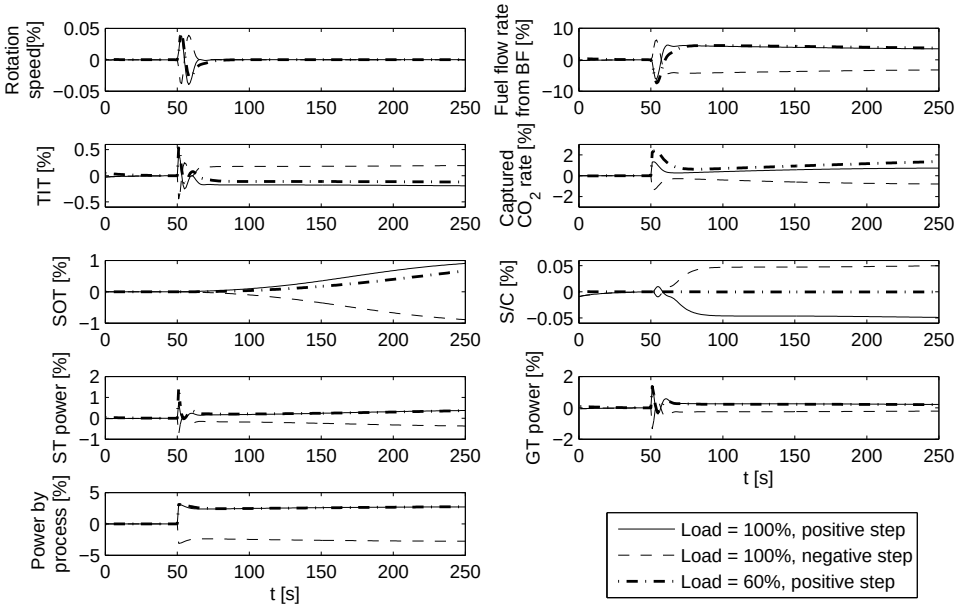

Figure 5.3: Dynamic responses from 10% air flow rate changes at 50s.

- The responses of the S/C ratio are much faster in the ATR power cycle. There are two steam streams which flow into the reformers in the HMR power cycle. The extracted steam from the ST can give a fast response. While the steam from the BFW is used to control the outlet temperature of the MTWGS. Thus the flow rate varies with the outlet stream of the HMR and has slower dynamics.

An increase of the inlet steam flow rate gives

- Increased S/C ratio.
- Very small influence on the steam reforming reactions, because at this operating point the temperature dominate the reaction rate compared to concentrations.
- Less power by the ST, because more steam is extracted from the HRSG.
- More power by the GT to compensate the decreased power by the ST.

Compared to the HMR power cycle

- The ATR power cycle has different dynamic responses of the rotation speed because of the different PI gains of shaft controller.
- The ATR power cycle has similar dynamic responses of the SOT.
- The gains to the S/C ratio is larger in the ATR power cycle. This is due to the larger steam flow rate changes in the ATR power cycle. There are two steam streams flow into reformers in the HMR power cycle. With 10% changes in extracted steam, the total steam change is relatively lower than in the ATR power cycle.
- The dynamics of power by the process, TIT and GT power is different in the ATR power cycle. The power by the process in the HMR power cycle contains the power by the air compressor and CO_2 compressor. While in the ATR power cycle, there are one more compressor, the fuel compressor. Further, the work done by the air compressor in the HMR power cycle varies with different operating points of the GT.

A decrease of the inlet air flow rate gives

- Reduced power by the air compressor.
- Reduced power by the ST. The reason is the same as a decreased NG flow rate.
- Decreased SOT and captured CO_2 rate, because of the decreased O/C.
- No significant changes in S/C ratio.

Compared to the HMR power cycle

- The ATR power cycle has different dynamic responses of the rotation speed because of the different PI gains of shaft controller.
- The gains to the S/C ratio, SOT, and the captured CO_2 rate is smaller in the ATR power cycle. This is due to the SOT influences the steam flow rate from the BFW which influences the SOT in turn.

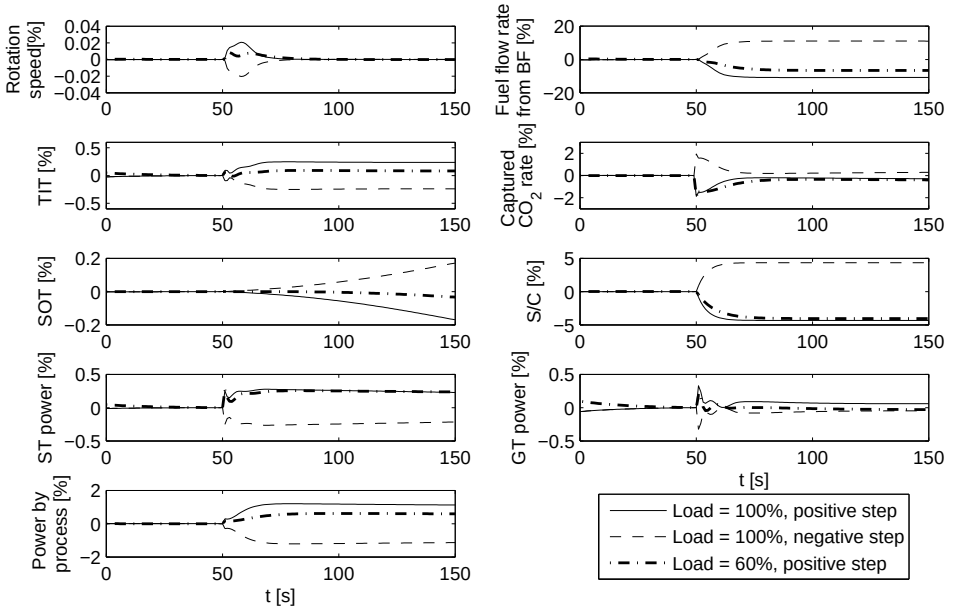

Figure 5.4: Dynamic responses from 10% CH_4 concentration changes at 50s.

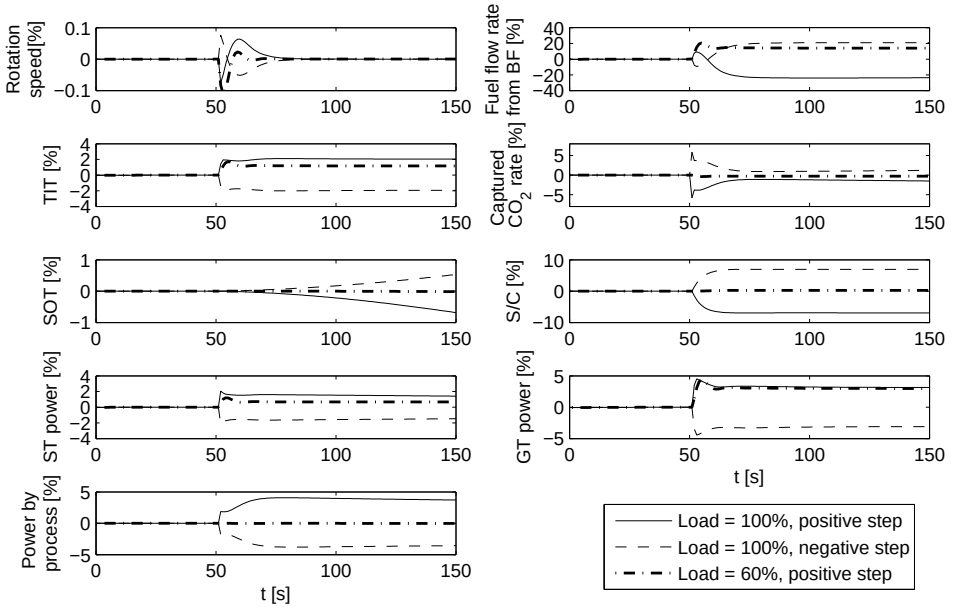

Figure 5.5: Dynamic responses from 10% load changes at 50s.

Figure 5.4 - 5.5 shows the responses from disturbances in CH_4 concentration in NG and load, respectively. There are a 1% CH_4 decrease and 0.5% increases of C_2H_6 and C_3H_8 at time 50s, and 10% load decrease at time 200s.

When all the inlet flow rates are constant, the decrease of CH_4 concentration and the increases of C_2H_6 and C_3H_8 concentration in NG give

- A surplus of fuel to the GT because of larger carbon content in the fuel.
- Decreased SOT, because a larger carbon content results in lower O/C ratio.
- Decreased CO_2 capture rate due to the decreased SOT.
- Decreased S/C ratio because of the increased carbon content in the fuel.
- Increase of power consumed by the CO_2 compressor.

The same as the HMR power cycle, the dynamic responses from CH_4 are similar to the responses from the NG flow rate changes in the ATR power cycle.

A decrease of the load gives

- Increased surplus of fuel to the GT.
- Decreased TIT to reduce the power generated by the GT.
- Decreased power by the ST and the GT.
- No significant influence on the fuel conversion process because of the constant inlet fuel, steam, and air.

The dynamic responses in the ATR power cycle are similar as the HMR power cycle except the responses of the ST power due to different operating point of the ST model.

5.2 Control structure design of the ATR power cycle

The control structure is designed in the same way as for the HMR power cycle as described in Chapter 3.

5.2.1 Operating objectives and constraints

Similar to the HMR power cycle, the following operating objective is defined

$$J = w_{fuel}\dot{n}_{fuel} + w_{air}\dot{n}_{air} + w_{CW}\dot{n}_{CW} - w_p P_{net} + w_{CO_2}\dot{n}_{CO_2} \quad (5.4)$$

$$\text{where } P_{net} = P_{GT} + P_{ST} - W_{AC} - W_{CO_2C} - W_{CW} - W_{FuelC} - W_{MDEA} - W_{BFW} - W_{UA}$$

Here, w are the prices for each input and output factor, $\dot{n}_{fuel}$, $\dot{n}_{air}$, $\dot{n}_{water}$, and $\dot{n}_{CO_2}$ are the molar flow rates of NG, air, water, and CO_2 emission. P_{GT}, and P_{ST} are the electric power generated by the GT and ST, respectively. W_{AC}, W_{CO_2C}, W_{CW}, W_{FuelC}, W_{MDEA}, W_{BFW}, and W_{UA} are the electric work of the air compressor for ATR, CO_2 compressor, cooling water pumps, fuel to combustion chamber pump, MDEA plant pump to recycle sorption, BFW pumps, and other auxiliary power.

The objective functions may be simplified. The inlet air and water are assumed to be under normal conditions (ambient temperature and pressure), so no cost is

assumed for these two resources. Further, W_{CW}, W_{MDEA}, W_{BFW}, and W_{UA} are neglected because they are very small compared to other work components.

Here, we consider the case of constant net electricity production, which is the general case when the plant is connected to an electric grid. This gives

$$J = w_{fuel}\dot{n}_{fuel} + w_{CO_2}\dot{n}_{CO_2} \tag{5.5}$$

with a net power production constraint

$$P_{net} = P_{GT} + P_{ST} - W_{CO_2C} - W_{AirC} - W_{FuelC} = const \tag{5.6}$$

P_{net} and the price for natural gas and CO_2 emissions are the same as the values in the HMR power cycle.

Table 5.1 shows the equality constraints and Table 5.2 shows the inequality constraints which may be encountered during operation. The values in these tables originate from several sources as included in the last column of the tables.

Table 5.1: The equality constraints in the ATR power cycle.

Constraint	Variable	Constraint value	Description
$C_{eq,1}$	The inlet fuel temperature of CC, $T_{CC,in}$	200 $°C$	Design specification for the GT
$C_{eq,2}$	Rotation speed, N_{rs}	3000 rpm	Design specification for the GT
$C_{eq,3}$	Inlet temperature for desulphurisation $T_{DS,in}$	400 $°C$	Design specification for desulphurisation to obtain the best catalyst activity
$C_{eq,4}$	Outlet steam fraction for syngas coolers, $\lambda_{sync,o}$	100 %	Temperature where all the water is vaporised
$C_{eq,5}$	Inlet temperature for flash tank, T_{FT}	30 $°C$	Design specification for flash tank
$C_{eq,6}$	Outlet flow rate for the buffer tank, $\dot{n}_{fuel,b}$	0 $kmol/s$	Fuel flow rate is 0 at steady state
$C_{eq,7}$	Air pressure	16.8 bar	Air pressure to ATR
$C_{eq,8}$	Fuel pressure	20 bar	Fuel pressure to CC

5.2.2 Identification of degrees of freedom and disturbances

The variables in Table 5.3 are selected for optimization. This is done under the assumption that the variables in HRSG and ST are well controlled and the DoFs and constraints are not considered here.

The same important disturbances and the range as the HMR power cycle are considered as in Chapter 3.

Table 5.2: The inequality constraints in the ATR power cycle.

Constraint	Variable	Constraint value	Description
C_1	VIGV angle	$-30° < \alpha < 60°$	Design specification for the GT Eichhorn Colombo et al. (2010)
C_2	GT fuel flow	$67\% < \dot{n}_{NG} < 100\%$	Design specification for the GT Kiameh (2002)
C_3	Extracted steam flow rate from ST	$0.8 < \dot{n}_{Steam} < 2.3\ kmol/s$	Design specification for HRSG Thermoflow Inc. (2011)
C_4	Extracted air flow rate from GT	$0 < \dot{n}_{air,extr} < 20\%$	Air extraction from GT Smith et al. (2002)
C_5	Turbine inlet temperature to GT	$T_{TIT} < 1400°C$	Design specification for the GT Chiesa et al. (2005)
C_6	Inlet S/C ratio for pre-reformer	$0.5 < r_{SC,PR} < 2$	Avoid carbine formation
C_7	Inlet temperature for pre-reformer	$350 < T_{PR,in} < 550°C$	Design specification for the PR reactor
C_8	Inlet temperature for ATR	$500°C < T_{ATR,in}$	Design specification for the ATR reactor
C_9	Temperature in ATR	$500 < T_{ATR,in} < 1200°C$	Design specification for the ATR catalyst
C_{10}	Inlet temperature for HTWGS	$350 < T_{HWGS}$	Design specification for MTWGS
C_{11}	Inlet temperature for LTWGS	$190 < T_{LTWGS} < 210°C$	Design specification for LTWGS
C_{12}	CO_2 capture rate	$C_{CO_2} > 90\%$	Design objective
$C_{13} - C_{19}$	Bypass flow rate of heat exchangers	$0 < \dot{n}_{HX,bp} < 100\%$	Bypass flow rate for heat exchangers HRSG1, HRSG2, HRSG3, HRSG4, HE2, HE3, HE4
C_{20}	TET	$550 < T_{TET} < 650°C$	TET, specified by HRSG

Table 5.3: DoFs for optimization of the ATR power cycle.

DoF	Variable	Description
u_1	$\dot{n}_{NG}$ $[kmol/s]$	NG flow rate
u_2	$\dot{n}_{NG,BT}$ $[kmol/s]$	NG flow rate from buffer tank
u_3	$\dot{n}_{Steam}$ $[kmol/s]$	Extracted steam flow rate from HRSG and ST
u_4	$\dot{n}_{Air}$ $[kmol/s]$	Additional air to ATR
u_5	$\dot{n}_{BFW}$ $[kmol/s]$	BFW flow rate
u_6	α [°]	VIGV angle
u_7	$\dot{n}_{CW}$ $[kmol/s]$	Cooling water to HE5 and HE6 for cooling syngas
u_8 $-u_{14}$	$\dot{n}_{by}$ $[kmol/s]$	Bypass flow rate of heat exchangers HRSG1, HRSG2, HRSG3, HRSG4, HE2, HE3, HE4
u_{15}	P_{AC} [MW]	Power by air compressor
u_{16}	$P_{Fuel,C}$ [MW]	Power by fuel compressor

5.2.3 Primary controlled variables

The controlled variables for the ATR power cycle are selected based on self-optimising control as described in Chapter 3.

First, all the equality constraints should be controlled. In the ATR power cycle, there are seven equality constraints (Table 5.1). Seven DoFs are used to satisfy these constraints. Since constraint C_5 is difficult to measure in practice, the turbine exhaust temperature (TET) is selected as the controlled variable. TET is controlled to a calculated optimised value as function of the load. Thus, TET is an equality constraint which can be controlled by VIGV and inlet fuel flow rate. Assume that the extracted air flow rate from the GT is proportional to the load and is not used for control as described by Nord et al. (2009). Then, seven DoFs, u_3, u_4, u_9, u_{10}, u_{11}, u_{12}, and u_{13}, are left for optimisation.

The process is optimised with the objective function (5.5). The nominal optimal operating point is given in Table 5.4.

For both cases when the cost of CO_2 is 0.72 and 1.50 €/$kmol$, the results show that six constraints (C_7, C_{11}, C_{12}, C_{15}, C_{16},and C_{17}) are active and one DoF can be used to minimise the effects of uncertainty and disturbances.

Candidate controlled variables are shown in Table 5.5. One or a combination of measurements from the candidate set is selected as the controlled variable(s). The measurement errors are assumed to be $1°C$ for temperatures, $0.1kmol/s$ for flow rates, and 1 MW for power. In the following, two methods for selecting CVs described in section 3.3.3 are applied, see step 1 and 2 below.

1.Maximum gain analysis

Table 5.6 shows the selected scaled gain with respect to the input (steam flow rate) and the two disturbances. The variable with the maximum gain is the S/C ratio $r_{SC,ATRi}$. Hence we can use $y_1 = r_{SC,ATRi}$ as the last controlled variable. The optimal setpoint from optimization is 1.29.

The optimal S/C ratio when the load is reduced is shown in Figure 5.6. This variable is not active in the range 60% to 100%.

Table 5.4: Optimal operation for the ATR power cycle.

Nominal operation	Value
Objective function (5.5) [€/s]	5.58/5.68
NG price [€/$kmol$]	5.56
Price of CO_2 emissions [€/$kmol$]	0.72/1.50
Active constraints	6
DoF for self-optimising control	1
LHV [MW]	927
Load [MW]	390
GT power output [MW]	305
ST net output [MW]	125
Auxiliary power including CO_2 compressor [MW]	40
Net efficiency (the ratio between load and LHV of NG) [%]	42
S/C [$kmol/kmol$]	1.29
O/C [$kmol/kmol$]	1.08
SOT [$°C$]	952
Captured CO_2 rate [%]	90
TIT [$°C$]	1367

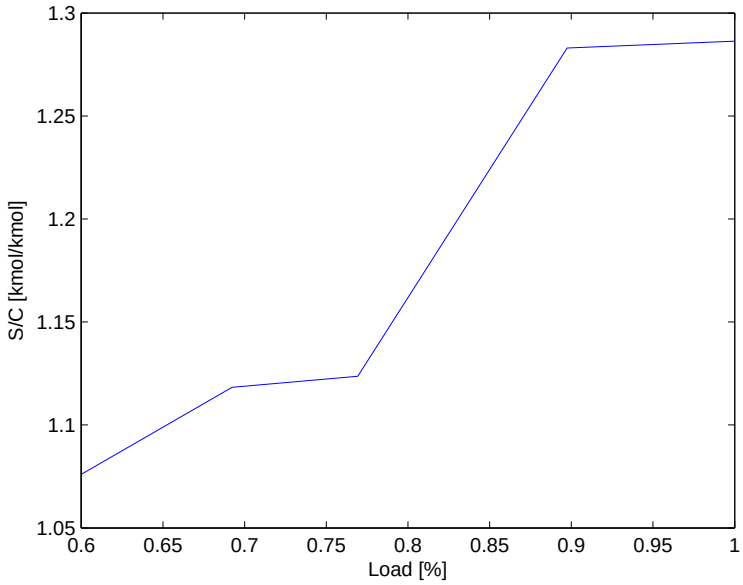

Figure 5.6: Optimum S/C with respect to the load.

2. Null space method with measurement selection

The minimal number of controlled variables is 3 ($= n_d + n_u$). We want to find the combination of three controlled variables that provides the minimal loss in the presence of specified disturbances and uncertainties.

Table 5.5: Candidate controlled variables.

Variable	Unit	Description
u	-	All of the inputs used in the optimisation
C_{CO_2}	$kmol/kmol$	Captured CO_2 rate
r_{SC}	$kmol/kmol$	Steam to carbine ratio at the pre-reformer inlet
λ_{S16,H_2O}	$kmol/kmol$	Syngas outlet H_2O concentration at the ATR reactor
λ_{S16,H_2}	$kmol/kmol$	SOH, syngas outlet H_2 concentration at the ATR reactor
λ_{S16,CH_4}	$kmol/kmol$	Sweep gas outlet CH_4 concentration at the ATR reactor
λ_{S21,H_2O}	$kmol/kmol$	Outlet O_2 concentration at the LTWGS reactor
λ_{S21,H_2}	$kmol/kmol$	Outlet O_2 concentration at the LTWGS reactor
λ_{S21,CH_4}	$kmol/kmol$	Outlet O_2 concentration at the LTWGS reactor
$\dot{n}_{S16,H_2O}$	$kmol/s$	Syngas outlet H_2O flow rate at the ATR reactor
$\dot{n}_{S16,H_2}$	$kmol/s$	SOH, syngas outlet H_2 flow rate at the ATR reactor
$\dot{n}_{S16,CH_4}$	$kmol/s$	Sweep gas outlet CH_4 flow rate at the ATR reactor
$\dot{n}_{S21,H_2O}$	$kmol/s$	Outlet O_2 flow rate at the LTWGS reactor
$\dot{n}_{S21,H_2}$	$kmol/s$	Outlet H_2 flow rate at the LTWGS reactor
$\dot{n}_{S21,CH_4}$	$kmol/s$	Outlet O_2 flow rate at the LTWGS reactor
P_{GT}	MW	Power generated by the combined cycle
P_A	MW	Power consumed by compressors and pumps

Table 5.6: Selected maximum scaled singular value for candidate controlled variables.

Measurement	$r_{SC,ATR,in}$	$T_{LTWGS,o}$	λ_{S21,H_2}	λ_{S21,H_2O}	$T_{ATR,o}$	λ_{S16,H_2O}
Scaled gain G	3.08	3.05	2.79	2.46	2.12	2.10

Two different controlled variables were found dependent on the value of disturbances. y_2 was found with a load disturbance of 10% and y_3 was with 40%.

$$y_2 = -0.0029T_{S7} - 0.8964\dot{n}_{S16,H_2} + +\dot{n}_{S21,H_2} \tag{5.7}$$

$$y_3 = -0.0009T_{S7} - 1.2332\dot{n}_{S16,H_2} + \dot{n}_{S21,H_2} \tag{5.8}$$

To find which is the best of these controlled variables, the loss is calculated based on the nonlinear model. In Figure 5.7, the economic loss is shown as a function of load changes. The results show that the controlled variable y_1 gives the best results in terms of lowest loss.

The losses due to the changes in CH_4 molar fraction are shown in Table 5.7.

Table 5.7: Optimal values for disturbance two.

Measurement	Optimal	Single measurement y_1	Combined measurements y_2
J	5.27	5.28	5.30
S/C	1.43	1.43	1.24

The controlled variables are the same with the CO_2 price. The optimal operation is found at the lowest possible CO_2 capture rate at two designed cases, which

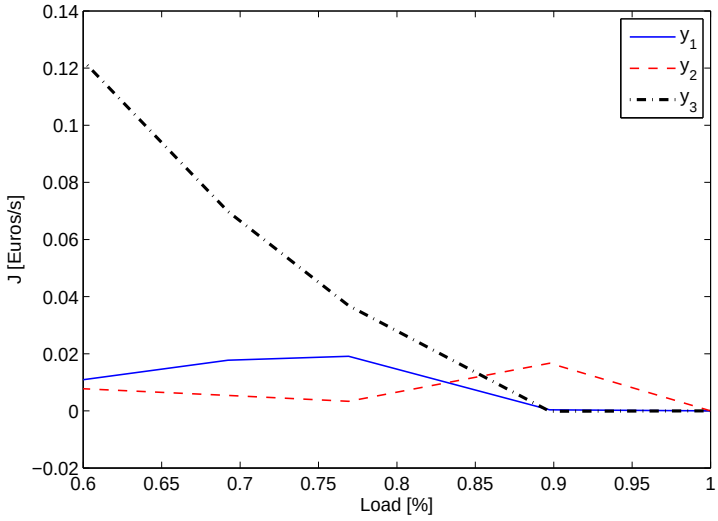

Figure 5.7: Losses due to load changes.

is different than the HMR power cycle. This is reasonable because the objective function includes a trade off between price of NG and CO_2 emission. The ATR power cycle has a lower thermal efficiency, which requires a higher NG flow rate than the HMR power cycle. If the CO_2 emission is further increased, different optimal operating points similar to the HMR power cycle can be found for the ATR power cycle.

The other variables are adapted to obtain the lowest conversion rate. In addition to the controlled variables for regulatory control layers, the controlled variables are those controlled to their active constraints, i.e., $T_{PR,in}$ (C_7), $T_{LTWGS}(C_{11})$, $\lambda_{CO_2,cap}(C_{12})$, $\dot{n}_{HRSG3,bp}(C_{15})$, $\dot{n}_{HRSG4,bp}(C_{16})$, $\dot{n}_{HE2,bp}(C_{17})$, and $r_{SC,ATR,in}$ (from self-optimization).

5.2.4 Set the production rate

In the ATR power cycle, the bottleneck when the plant is operating at 100% load is the GT capacity. Hence, the production rate is set at the inlet fuel flow rate of the combustion chamber.

In the former sections, a top-down analysis has been performed as a basis for the forthcoming design which starts with the regulatory control layer.

5.2.5 Design regulatory control layer

At this design step, pairing of the manipulated variables and controlled variables is made.

1. The cooling water to cooling down stream to FT is controlled to a design value (u_7). The control loop does not allow the other processes to exert significant

influences on the temperature. The corresponding constraint is $C_{eq,5}$.

2. The outlet steam fraction of syngas coolers is controlled to satisfy the constraints $C_{eq,4}$. The manipulated variable is u_5.
3. Flow rate proportion (u_{14}) is used to control the inlet fuel temperature to GT and satisfy the constraints $C_{eq,1}$.
4. The bypass flow rate of HRSG1 (u_8) is used to control the inlet temperature for desulphurisation. The corresponding constraint is $C_{eq,3}$.
5. The NG flow rate (u_1) is used to control the rotation speed ($C_{eq,2}$). To obtain a fast response, a buffer tank is installed at the CC inlet. At steady state, the fuel flow from the buffer tank should be zero ($C_{eq,6}$). A cascade controller using NG to control the fuel flow from the buffer tank, and fuel flow rate from the buffer tank (u_2) to control the rotation speed is used. The corresponding constraint is $C_{eq,6}$.
6. We assume that VIGV (u_6) is used to control TET. For some combined cycles, TET is kept constant to obtain a high net efficiency for the combined cycle. The corresponding constraint is C_{20}.
7. The power to air and fuel compressors (u_{15} and u_{16}) are used to control the corresponding outlet pressure (C_{eq7} and $C_{eq,8}$).

5.2.6 Design supervisory control layer

In addition to the regulatory control loops, the bypass flow of heat exchangers HRSG2, HRSG3, HRSG4, HE2, and HE3 is used to control the corresponding outlet temperature. The $r_{SC,ATRin}$ is controlled by the steam flow rate $\dot{n}_{steam}$, because this variable has a direct effect on the controlled variable and it also gives the largest gain in the RGA analysis. The remaining controlled variable C_{CO_2} is controlled by the air flow rate $\dot{n}_{air}$.

The load may change frequently during operation, and the values are easy to measure. Feedforward controllers can be applied for this control loop. Since the responses from NG and steam flow rate to the controlled variables are relatively fast, in seconds, steady state controllers with polynomial functions can be used to compensate the load change.

The complete control structure is shown in Figure 5.8. And all control loops are specified in Table 5.8.

5.2.7 Design optimisation layer

Likewise as for the HMR power cycle, no optimisation layer is designed for the ATR power cycle.

5.2.8 Validation based on dynamic simulation

In this section, first controller type is selected and control performance for each loop is investigated. Then, the dynamic responses of the whole plant are studied.

To compare the performance, the disturbances for the ATR power cycle are selected the same as those in the HMR power cycle.

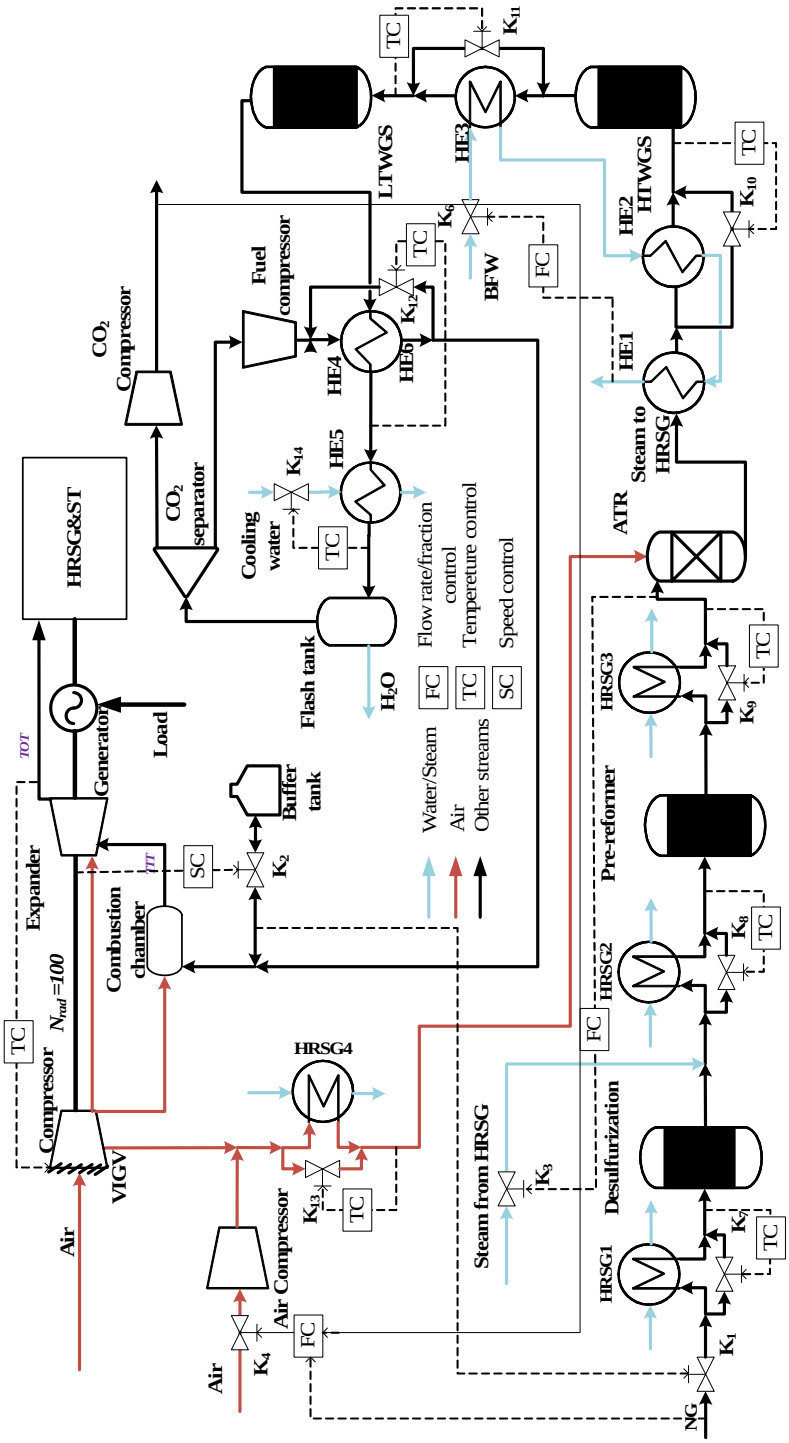

Figure 5.8: The control structure for the ATR power cycle.

Table 5.8: Control loops for the ATR power cycle.

Regulatory control layer				
Control loop	1	2	3	4
Controlled variable	$T_{CC,in}$	N_{rs}	$T_{DS,in}$	$\lambda_{syn,o}$
Corresponding constraint	$C_{eq,1}$	$C_{eq,2}$	$C_{eq,3}$	$C_{eq,4}$
Manipulated variable	u_{14}	u_1	u_8	u_5
Control loop	5	6	7	8
Controlled variable	T_{FTin}	$\dot{n}_{fuel,b}$	P_{AC}	$P_{fuel,C}$
Corresponding constraint	$C_{eq,5}$	$C_{eq,6}$	$C_{eq,7}$	$C_{eq,8}$
Manipulated variable	u_7	u_2	u_{15}	u_{16}
Supervisory control layer				
Control loop	9	10	11	12
Controlled variable	$T_{PR,in}$	$T_{LTWGS,in}$	$T_{ATR,NGin}$	T_{ATR_Airin}
Corresponding constraint	C_7	C_{11}	C_{15}	C_{16}
Manipulated variable	u_9	u_{13}	u_{10}	u_{11}
Control loop	13	14	15	16
Controlled variable	$T_{HWGS,in}$	T_{TET}	C_{CO_2}	$r_{SC,ATRin}$
Corresponding constraint	C_{17}	C_{20}	C_{12}	-
Manipulated variable	u_{12}	u_6	u_4	u_3

Controller selection and tuning

Continuous PI type controllers including integrator wind-up functionality are used in all the control loops. The controllers are tuned for setpoint tracking with fast and flat responses, and disturbance rejection. All controllers have been implemented in the power cycle simulator. The feedforward control uses polynomial functions from curve fitting of steady state data.

1. The air to captured CO_2 rate control loop.

   The open loop dynamic responses are shown in Figure 5.9. Inverse responses and large overshoot are observed. Hence, a low PI gain is used. The objective of this control loop is to maintain the captured carbon rate at 90%. This value is based on long time observation. The values at high frequency are of limited interest here. A low pass filter hence can be added before the PI controller to capture the interested dynamics and to reduce the effects by high frequency changes. The cutoff frequency of the filter is found based on the identified transfer function from step changes. Figure 5.10 shows the Bode plot and the selected cutoff frequency. The dash-dotted line and dotted line in Figure 5.9 show the closed loop responses without filter and with filter when a 10% step changes of load is applied.

2. Steam to S/C ratio control loops.

   The open loop and closed loop responses from the steam flow rate to S/C ratio and the combined measurements are shown in Figure 5.11. The figure shows that the loop from the steam flow rate to a single measurement with inlet S/C ratio has a simpler dynamic response than combined measurements. Hence, the structure which uses S/C ratio as a controlled variable is suggested.

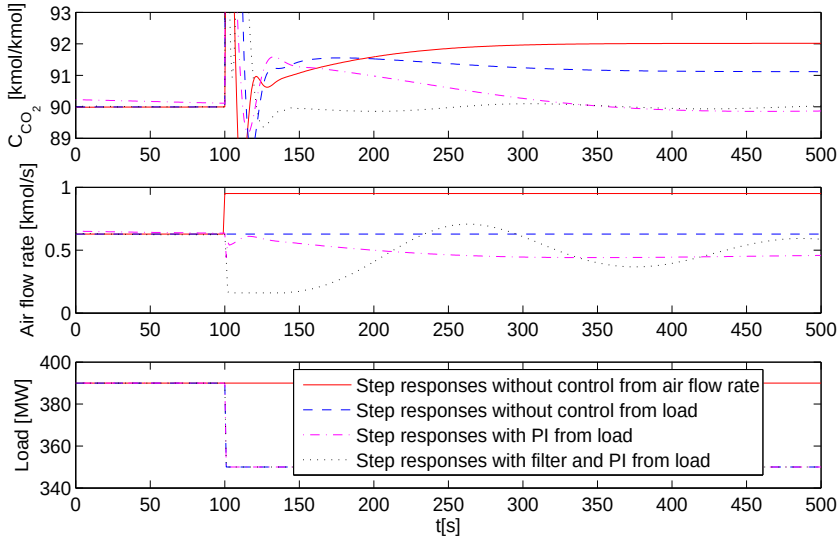

Figure 5.9: Dynamic responses of the air to the captured CO_2 rate control loop.

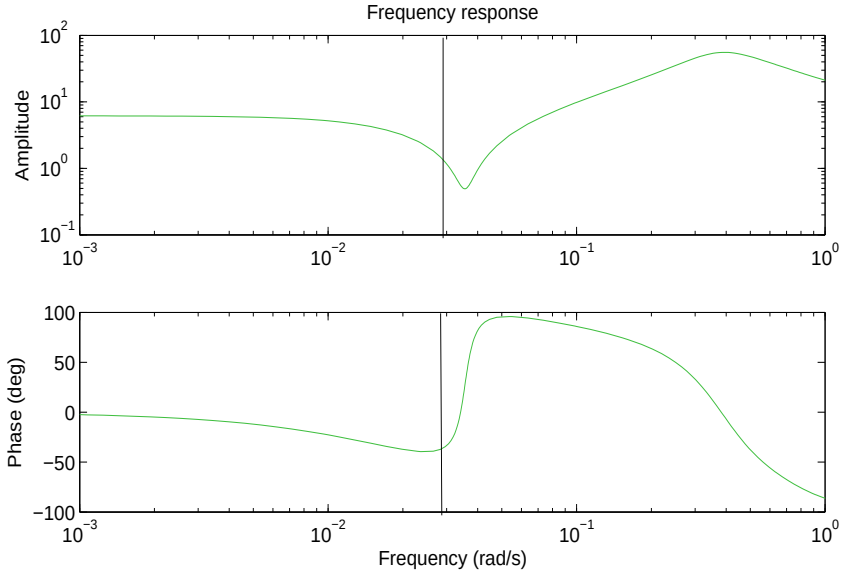

Figure 5.10: Frequency responses of the air to the captured CO_2 rate control loop.

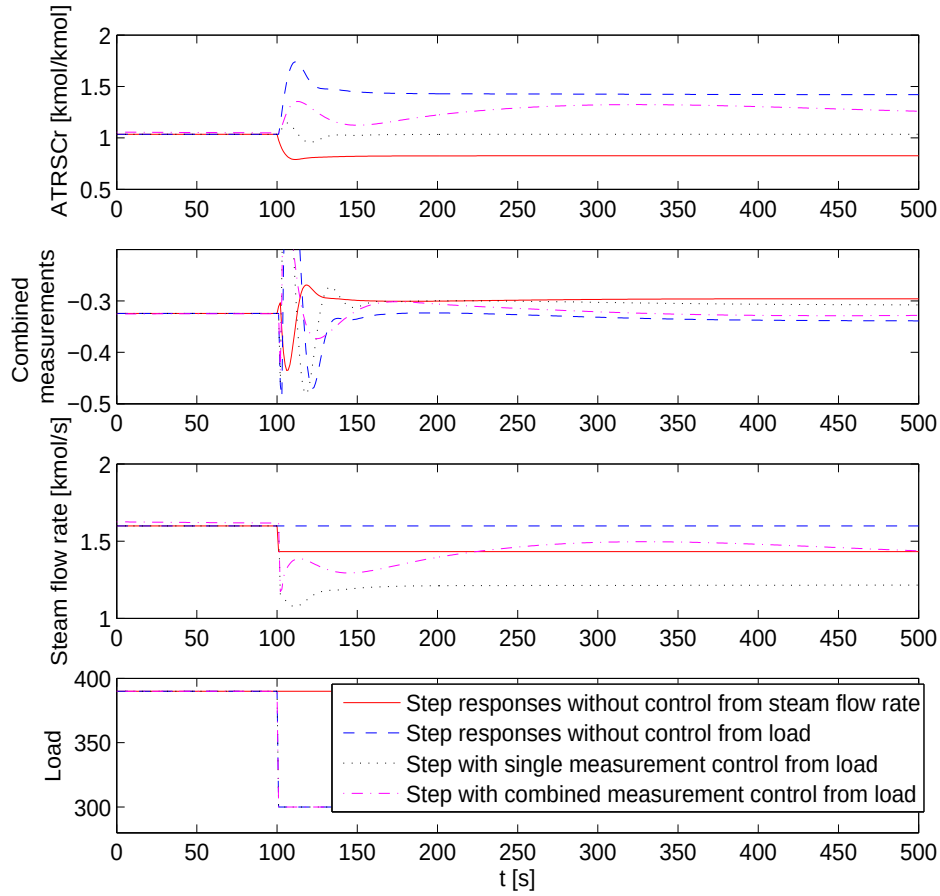

Figure 5.11: Dynamic responses of the steam to S/C ratio control loop by a load step change.

Simulation results

The dynamic responses of the selected control loops and variables are depicted in following figures. Figure 5.12 - 5.15 show the responses from the load changes, while Figure 5.16 - 5.19 present responses from the change of CH_4 molar fraction.

All these figures demonstrate rapid response to load changes and exhibit good load-following capabilities.

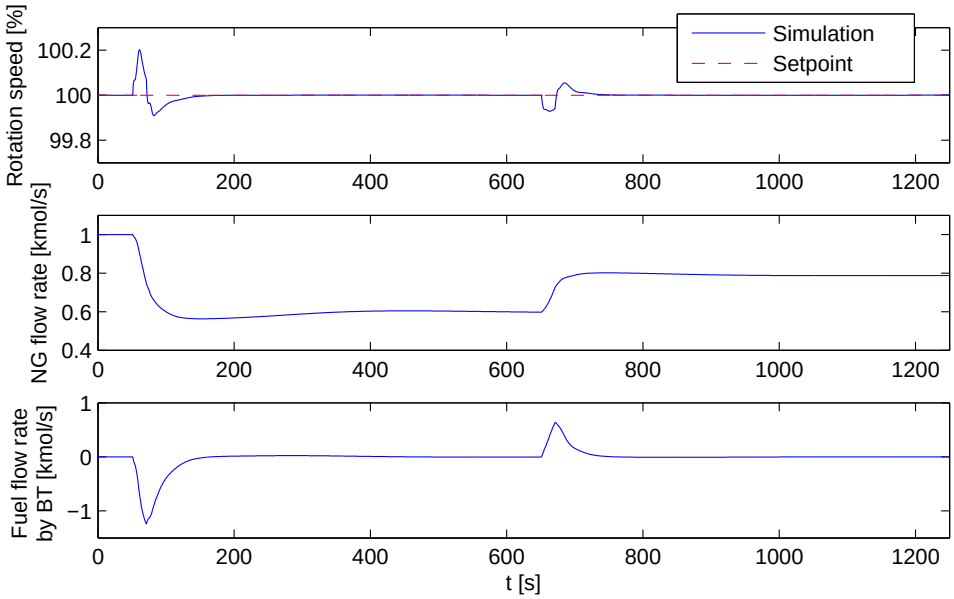

Figure 5.12: Dynamic responses of the NG flow rate, and the rotation speed from load disturbances.

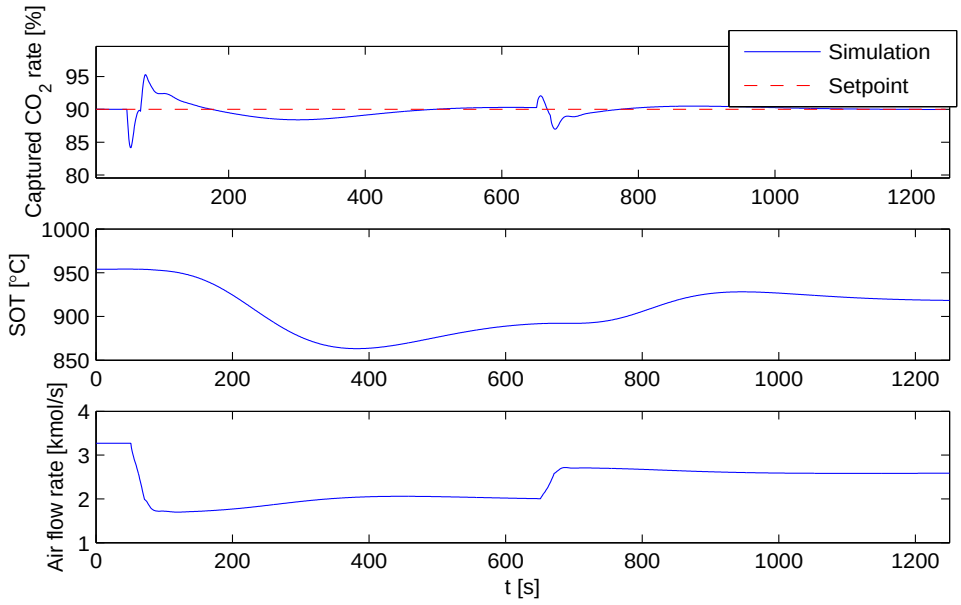

Figure 5.13: Dynamic responses of the captured CO_2 rate, SOT, and the air flow rate from load disturbances.

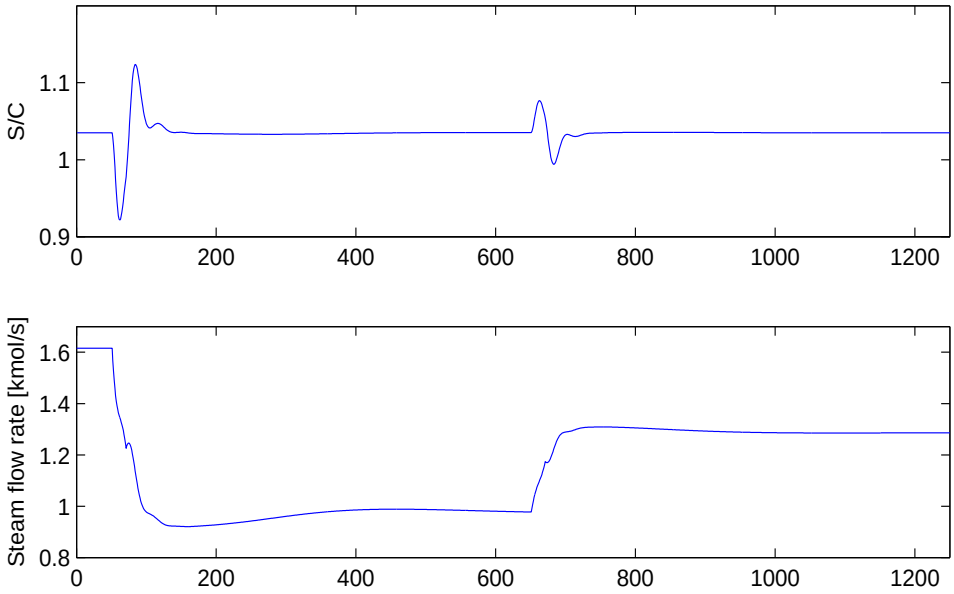

Figure 5.14: Dynamic responses of the S/C ratio, and the steam flow rate from load disturbances.

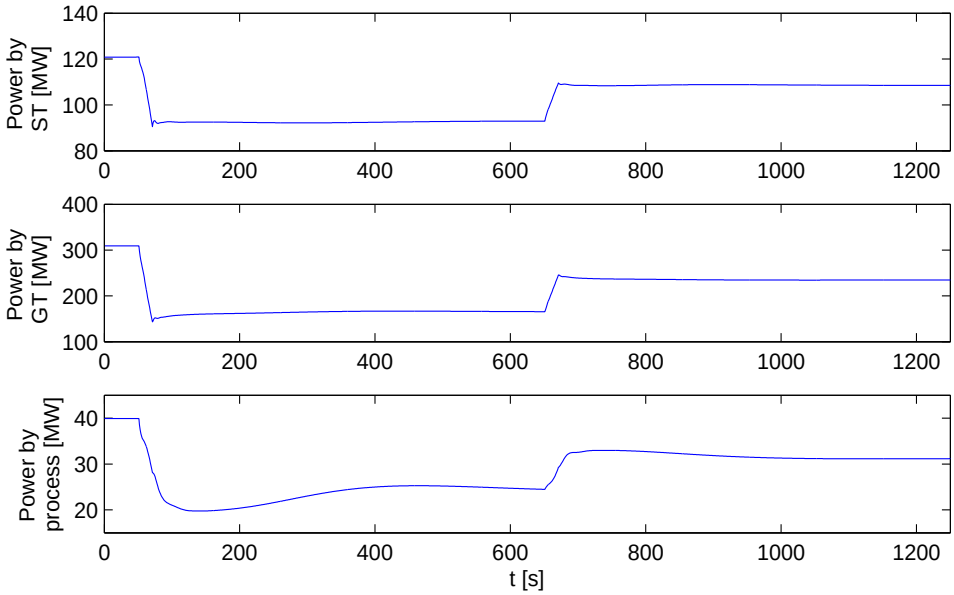

Figure 5.15: Dynamic responses of the outlet power by GT, ST and the auxiliary unit from load disturbances.

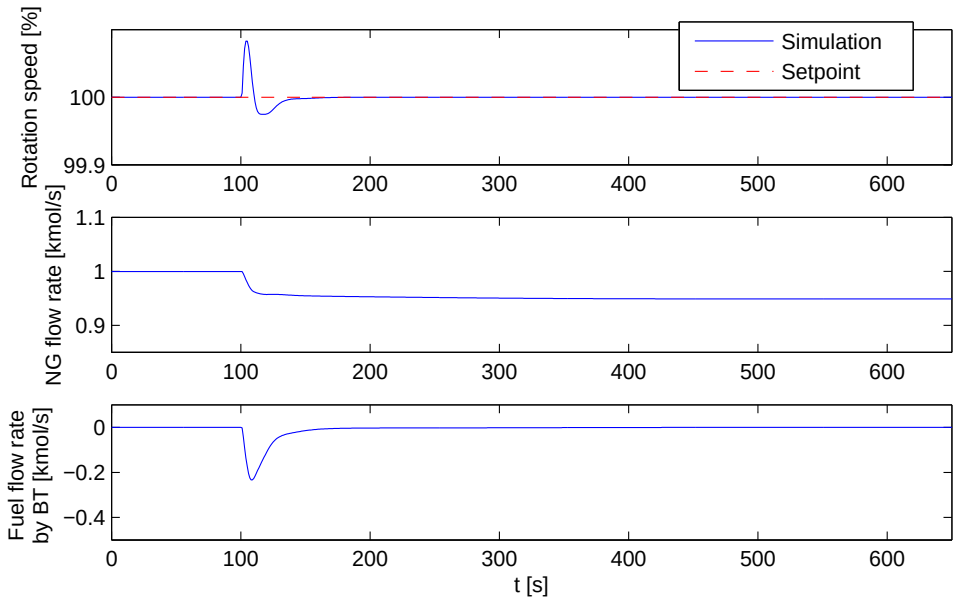

Figure 5.16: Dynamic responses of the NG flow rate, and the rotation speed from NG concentration disturbances.

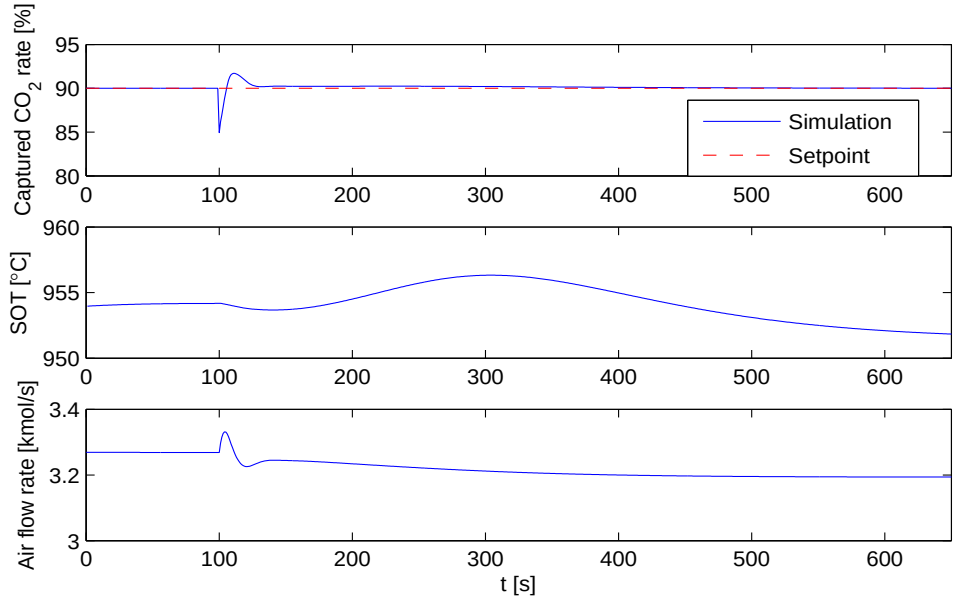

Figure 5.17: Dynamic responses of the captured CO_2 rate, SOT, and the air flow rate from NG concentration disturbances.

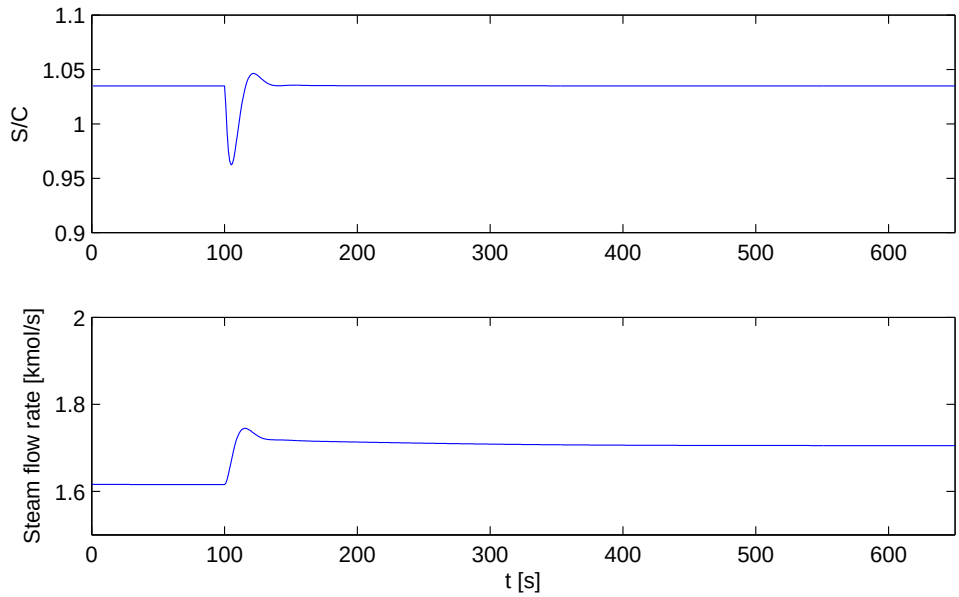

Figure 5.18: Dynamic responses of the S/C ratio, and the steam flow rate from NG concentration disturbances.

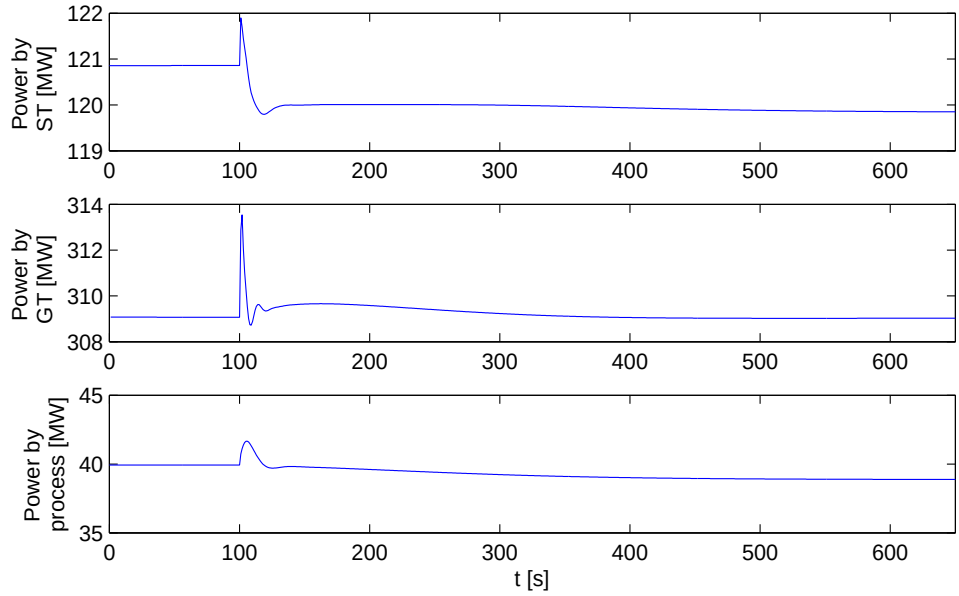

Figure 5.19: Dynamic responses of outlet power by GT, ST and the auxiliary unit from NG concentration disturbances.

5.2.9 Discussion

The HMR and ATR power cycles are two different pre-combustion power cycles for reduction of CO_2 emission. Both processes use steam reforming and WGS processes to convert hydrocarbons to H_2 and CO_2. The HMR process includes combustion of hydrogen which is separated from the steam reforming reaction to provide the heat, while an ATR process uses partial oxidation of hydrocarbons to generate the heat. Different reactions and different operating conditions results in different process design and control structure design to achieve high efficiency.

The main differences are

- There are two sources of air in the ATR power cycle. One source of air is extracted from the GT, and the other is from compressed air at atmosphere. In the HMR power cycle, only the extracted air from the GT is fed into the conversion processes.
- The NG is preheated by HRSG in the ATR power cycle, while in the HMR power cycle NG is preheated by syngas coolers.
- The fuel pressure after CO_2 separation is much lower than the GT requirement in the ATR power cycle. Hence, a compressor is added to compress the fuel.
- The pressure in the ATR reactor is around $16bar$, while the pressure in the ATR reactors are around $24bar$.
- A HTWGS reactor is used in the ATR power cycle instead of MTWGS in the HMR power cycle.
- Two different GT inlet fuel temperatures are used in the two processes.
- The steam generated from syngas coolers in the ATR power cycle is directly fed into HRSG and ST. This steam is used for steam reforming in the HMR power cycles.

Different manipulated variables, and constraints are found

- The range for the S/C ratio for the ATR rector is much wider than for the HMR reactor. Coke formation may result when the S/C ratio is blow 2.1 in the HMR reactor, while in the ATR reactor this occurs at 0.6.
- The fuel inlet temperature to CC in the HMR power cycle is designed as $400°C$ while the temperature for the ATR power cycle is $200°C$.
- A higher temperature is required for the HTWGS reactor in the ATR power cycle as compared to the MTWGS reactor in the HMR power cycle.
- The ATR reactor can tolerate a much higher temperature (Nord et al., 2009) than the HMR reactor.
- There are two sources of air in the ATR power cycles which gives more freedom for control than for the HMR power cycle.
- There is less freedom to control the S/C ratio in the ATR power cycle than the HMR power cycle which has another source from BFW.
- The fuel compressor and air compressor give more freedom to control the pressure in the ATR power cycle.

The main differences between the steady state and dynamic responses of these two power cycles are

- The HMR power cycle has higher efficiency(51.8%).
- The optimal S/C ratio for the ATR power cycle (1.3) is much lower than in the HMR power cycle (2.1).
- The ATR power cycle has a wider operating range and a simpler control structure.
- Both power cycles have much slower responses than gas power cycles without CO_2 capture. This slow response is due to slow thermal dynamics of reactors.
- The two power cycles have similar dynamics.

5.3 Conclusion

Dynamic models of an ATR based pre-combustion gas power cycle have been studied, and the control structure is designed in a systematic way.

A new mathematical model based on first principles of the whole power cycle is developed. Dynamic responses are studied. The ATR based power cycle has different response times and nonlinearities as comparable to the HMR power cycle. Plant-wide control structure design is used to minimize an economic objective with respect to different disturbances.

The power cycle with well-tuned PI controllers and feedforward controllers is simulated. The results show that the selected control structure can result in a stable system and that the PI controllers can make the controlled variables converge to desired values.

The results are used to benchmark dynamic responses and control structures of the HMR power cycle. The dynamic responses of the two systems have lots in common. The main differences are due to different syngas generators, different operating conditions, and process structure. The designed control structures for both systems give rapid response to load changes and exhibit good load-following capabilities. The ATR power cycle has one optimal point with the selected CO_2 prices, such that the same control structure can be used for different operating conditions. In comparison, the HMR power cycle has two optimal points and more active process constraints, e.g., constraints on SOT and S/C. The control structure of the ATR power cycle has a lower complexity as compared to the HMR power cycle.

Chapter 6

Conclusion and recommendations for further work

This chapter first provides a summary of the achieved results, and then some practical issues when implementing such kind of power cycles are discussed. In the end, possible directions for future work are given.

6.1 Conclusion

The operability analyses of two pre-combustion power cycles are studied in this thesis. Both power cycles are analysed through dynamic simulations and systematic control structure design.

In Chapter 2, a dynamic model of the HMR power cycle based on first principles is described. The purpose of this model is to study dynamics, control and ultimately develop an overall robust operational strategy. Simulation results from the model are shown. The simulations show that both the steady state and dynamic behaviour of the plant depend strongly on the flow rates of feed streams. Most of the responses are not strictly linear because of the shaft speed controller, and the nonlinear reactor, GT and ST models.

Because of the complexity of the system and the nonlinearities of the dynamic responses, a systematic approach to control structure design is essential. In Chapter 3, the control structure design procedure proposed by Skogestad and Postlethwaite (2005) is applied to the power cycle. To determine the control structure, an economic objective is chosen, the DoFs and constraints are found, and the possible disturbances are assumed. The system is linearised at a nominal operating point. The controlled variables are selected by self-optimising control. For different algorithms and objective functions we obtain different sets of controlled variables and their setpoints. The best sets are selected based on loss analysis of the nonlinear system. The control structure with well-tuned PI controllers and feedforward controllers is simulated for two cases. The results show that the designed control structure can result in a stable system and that PI controllers can make the controlled variables converge to desired values. However, some constraints may be violated during the transient period. PI controllers with gain scheduling or an ad-

vanced controller, such as MPC, can be an option. Therefore MPC controllers are designed in Chapter 4. Some PI control loops presented in Chapter 3 are replaced by MPC controllers to handle the constraints. The results show that because of the nonlinearities, the MPC controllers give a better dynamic behaviour than PI with feedforward controllers for given disturbances. PI with feedforward controllers are easy to implement and do not require much information about the system. However, they may give large overshoot or constraint violation. MPC controllers can overcome these drawbacks and give a smoother dynamic performance. Hence, for the HMR power cycle studied here, MPC controllers are recommended above PI controllers.

Dynamic models and control structure design of an ATR based pre-combustion gas power cycle which follow the same methods as the analysis of the HMR power cycle have been studied in Chapter 5. The performance of these two power cycles are compared. The ATR based power cycle has different response times and nonlinearities as comparable to the HMR power cycle. Results with well-tuned PI controllers and feedforward control show that the selected control structure can give good performance. The results are used to benchmark dynamic responses and control structures of the HMR power cycle. The dynamic responses of the two systems have lots in common. The main differences are due to different syngas generators, different operating conditions, and process structure. The designed control structures for both systems give rapid response to load changes and exhibit good load-following capabilities. The ATR power cycle has one optimal point with the selected CO_2 prices, such that the same control structure can be used for different operating conditions. In comparison, the HMR power cycle has two optimal points and more active process constraints, e.g., constraints on SOT and S/C ratio. The control structure of the ATR power cycle has a lower complexity as compared to the HMR power cycle.

The analyses above show that although the pre-combustion power cycle have a relative complex flow diagraph, the dynamic performance can be well controlled by traditional controllers. Moreover control design at an early process design phase can provide more information on operability and influence the process design itself, e.g., design the capacity of the buffer tanks and heat exchangers. The control structures are found by an economic objective and different structures may hence be found for different prices and costs.

The systematic approach for control structure design has been successfully implemented on two different power cycles. Hence, this approach is recommended for control design for other similar power cycles.

6.2 Practical implementation issues

In this study, two novel power cycles based on future technologies are studied, which means that some technologies, e.g., the HMR reactor and the hydrogen GT (Kanniche et al., 2010), are not available at the present time. Moreover, many practical issues should be considered when implementing these power cycles. This include the following considerations.

- Although the processes for syngas generation and CO_2 separation is similar

to those in the chemical industry, the configuration and operating mode is different due to the frequently changed power load which the chemical processes should follow (Damen et al., 2011).

- Any gas leakage (CO_2, H_2, NG) will be dangerous.
- Membrane leakage and catalyst degradation may reduce the efficiency and influence the dynamics of the whole plant.
- Operating with the high pressure and temperate gases will be dangerous.
- Storage of the hydrogen and CO_2 will be costly.
- Start up and shutdown the whole plant will be expensive and time consuming.
- CO_2 corrosion may be observed (Damen et al., 2011).
- In practice, the operating point most of the time will be at part load. This will reduce the efficiency significantly.
- Operational experience of the CO_2 separation units can be found in (Seibert et al., 2011).

6.3 Further work

Further work and possible future directions are

- The dynamic models in this thesis is developed to capture the main dynamics for designed inputs and disturbances. The model can be extended to capture more dynamics and a broader set of disturbances or failures. The following extensions can be considered
  - An HMR model which can involve membrane leakage.
  - A detailed CO_2 capture plant which gives variable capture rate.
  - The models for HRSG and ST can be replaced by physics based models.
  - Include dynamic pressure changes in the models.
- The dynamic models presented in this thesis are based on literature, and verified based on design values, available experimental data and some available detailed mathematical models. It is an obvious need to further verify the performances based on real power plant data.
- This thesis mainly focused on one of the most efficient and one of the most common studied power cycles. The other power cycles can be analysed in the same pattern.
- Nonlinear MPC controllers for captured CO_2 rate may be an option even though linear MPC for selected components works well. The major challenge is to find a fast and accurate nonlinear model.
- The optimal operating point may be different for different load changes as shown in Figure 3.5. Therefor, site-wide optimization as shown in Figure 3.1 is an interesting topic.

- The designed control structure is based on the assumption that there are only two important disturbance i.e., load changes and inlet CH_4 fraction. Other disturbances, e.g., hydrogen membrane leakage, and more comprehensive disturbance patterns, e.g., using data from real plants, could be further considered.
- For GT, start up and shut down may be frequent. Moreover, the behaviours during these operations are different than during normal and part load operations (Eichhorn Colombo et al., 2010). A control structure to handle start up and shut down of the HMR cycle needs thus to be developed.
- The objective function for control structure design in this study is based on static economic losses. Since the load changes during operation are frequent, an objective function which involves dynamic performances can be used. The control structure can be further developed based this objective.

Appendices

Appendix A

Calculation of heat capacity and enthalpy

Hyperbolic functions are used to approximate heat capacity at constant pressure.

$$Cp = C_1 + C_2 \left[\frac{C_3/T}{\sinh(C_3/T)}\right]^2 + C_4 \left[\frac{C_5/T}{\cosh(C_5/T)}\right]^2 \tag{A.1}$$

Further, heat capacity of liquid water is calculated as

$$Cp = C_1 + C_2 T + C_3 T^2 + C_4 T^3 + C_5 T^4 \tag{A.2}$$

The values of parameters are

Table A.1: Constants for calculating heat capacity.

Symbol	C_1	C_2	C_3	C_4	C_5	$T_{\min}$	$T_{\max}$
H_2O	33360	26790	2610.5	8900	1169	100	2000
CO	29110	8770	3085.1	8460	1538.2	60	1500
CO_2	29370	34540	1428	26400	588	50	5000
H_2	27620	9560	2466	3760	567.6	250	1500
CH_4	33300	79930	2086.9	41600	991.96	50	1500
C_2H_6	40330	134220	1655.5	73220	752.87	60	1500
C_3H_8	51920	192450	1626.5	116800	723.6	200	1500
C_4H_{10}	71340	243000	1630	150330	730.42	200	1500
O_2	29100	10040	2526.5	9360	1153.8	50	1500
N_2	29110	8610	1701.6	100	909.79	50	1500
Ar	20790	0	0	0	0	100	1500
H_2S	33290	26090	913.4	−17980	949.4	100	1500
H_2O (liquid)	276370	−2090.1	8.125	−0.014	0	0	250

Enthalpy is calculated as follows

$$E = E_{form} + \int_{T_0}^{T} Cp(T)dT \tag{A.3}$$

$$\approx E_{form} + (T - T_0)(Cp + Cp_0)/2 \tag{A.4}$$

$$\approx E_{form} + (Cp_0 + Cp + (Cp_{1/3} + Cp_{2/3}) * 3) * (T - T_0)/8 \tag{A.5}$$

Here
$C_{p1/3}$ $[kJ/kmol/K]$ is the heat capacity at temperature $(T - T_0)/3$.
$C_{p2/3}$ $[kJ/kmol/K]$ is the heat capacity at temperature $2(T - T_0)/3$.
(A.5) is only used in the GT model.

Appendix B

Parameter values

This section includes parameter values. Most of the parameters are given from background information and a few are tuned by comparing the model outputs to a stationary high fidelity Aspen plus model. Parameters which influence model dynamics have been chosen to give reasonable transient behavior. It has, however, not been possible to gain exact quantitative information on these properties because no such real power plant exists today.

There are eleven heat exchangers in the process. The parameters for each heat exchanger are shown in Table B.1. The flow configuration for all heat exchangers is counter-current.

Table B.1: Parameters for heat exchangers.

Symbol	Flow configuration	U $[kJ/m^2/s]$
$HE1$	$HGHG$	300
$HE2$	$HGHG$	300
$HE3$	$HGHG$	300
$HE4$	$HGHG$	300
$HE5$	$HGBL$	485
$HE6$	$HGLG$	95
$HE7$	$HGCW$	430
$HE8$	$HGCW$	430
$HE9$	$HGHG$	300
$HE11$	$HGCW$	430

The subscription $HGHG$ means the fluid at the two sides of the heat exchanger are pressurized gas, $HGLG$ pressurized gas vs. low pressure gas, $HGBL$ pressurized gas vs. boiling liquid, $HGCW$ pressurized gas vs. boiler feed water.

The reaction models using the following parameter values

Table B.2: Parameters for WGS reaction.

Parameter	Pre-exponential factor	Activation energy	Unit
Q_H	0.0412	65.9×10^3	$kmol/ms/s/m$
k_H	$e^{-82/R} * e^{40000/(RT)}$		-
$k_{1,SMR}$	4.225×10^{15}	240.1×10^3	$kmol.bar^{1/2}/kgcats$
$k_{2,SMR}$	1.955×10^6	67.13×10^3	$kmol/kgcats$
$k_{3,SMR}$	1.02×10^{15}	243.9×10^3	$kmol.bar^{1/2}/kgcats$
$K_{CH_4,SMR}$	6.65×10^{-4}	-38280	bar^{-1}
$K_{CO,SMR}$	8.23×10^{-5}	-70650	bar^{-1}
$K_{H_2O,SMR}$	1.77×10^5	88680	-
$K_{H_2,SMR}$	6.12×10^{-9}	-82900	bar^{-1}
$K_{1,SMR}$	$e^{-26830/T+30.114}$		bar^2
$K_{2,SMR}$	$e^{4400/T-4.036}$		-
$k_{1,MTWGS}$	4×10^3	51×10^3	$J/mol/kgcat$
$k_{2,MTWGS}$	2.4×10^4	78×10^3	J/K
$k_{1,LTWGS}$	1.8×10^3	61×10^3	$J/mol/kgcat$
$k_{2,LTWGS}$	4×10^4	34×10^3	-
k_{Cb}	1×10^4	1×10^4	$kmol/s$

Stoichiometry matrices for the reactions are

$$C_{r1} = \begin{bmatrix} -2 & 1 & 0 & 3 & 1 & -1 & 0 & 0 & 0 & 0 & 0 & 0 \\ -2 & 1 & 0 & 2 & 2 & 0 & -1 & 0 & 0 & 0 & 0 & 0 \\ -2 & 1 & 0 & 1 & 3 & 0 & 0 & -1 & 0 & 0 & 0 & 0 \end{bmatrix} \tag{B.1}$$

$$C_{r2} = \begin{bmatrix} -1 & 1 & 0 & 3 & -1 & 0 & 0 & 0 & 0 & 0 & 0 & 0 \\ -1 & -1 & 1 & 1 & 1 & 0 & 0 & 0 & 0 & 0 & 0 & 0 \\ -2 & 0 & 1 & 4 & -1 & 0 & 0 & 0 & 0 & 0 & 0 & 0 \end{bmatrix} \tag{B.2}$$

$$C_{r3} = \begin{bmatrix} 2 & 0 & -2 & 0 & 0 & 0 & 0 & 0 & -1 & 0 & 0 & 0 \end{bmatrix} \tag{B.3}$$

$$C_{r4} = \begin{bmatrix} -1 & -1 & 1 & 1 & 0 & 0 & 0 & 0 & 0 & 0 & 0 & 0 \end{bmatrix} \tag{B.4}$$

$$C_{r5} = \begin{bmatrix} 2 & 0 & 0 & -2 & 0 & 0 & 0 & 0 & -1 & 0 & 0 & 0 \\ 1 & 0 & 1 & -1 & 0 & 0 & 0 & 0 & -1 & 0 & 0 & 0 \\ 0 & -2 & 2 & 0 & 0 & 0 & 0 & 0 & -1 & 0 & 0 & 0 \end{bmatrix} \tag{B.5}$$

The other parameters for each process unit are listed in Table B.3. The data used for inlet streams of the power cycle, i.e., water, air, and NG are shown in Table B.4. The flow rate can be varied for different operations. The design values for each stream provided by STATOIL are listed in Tables B.5 - B.6.

Table B.3: Parameter values for each process unit.

Parameter	Value	Unit	Description
α_{bp}	20	%	Bypass flow rate proportion for each heat exchanger
w	0.0015	m	Width of a single channel for the membrane reactor
l	1.75	m	Length of the monolith module stack
A	9.9	m	Cross section of the membrane reactor
A_{mem}	15241	m^2	Total membrane surface area
V	17.32	m^3	Volume of the membrane reactor
m_m	45000	kg	Reactor mass for the membrane reactor
$c_{p,m}$	0.75	$kJ/K/kg$	Heat capacity of the support material for membrane reactor
U	300	$kJ/s/m^2$	The overall heat transfer coefficient for the membrane reactor
m_{cat}	500	kg/m^3	Catalyst density for the membrane reactor
V_{HE5}	5	m^3	Volume of HE5
ΔH_{vap}	32011	$kJ/kmol.$	Enthalpy changes of water evaporation at $32bar$
V_{MTWGS}	106	m^3	Volume for MTWGS
V_{LTWGS}	45	m^3	Volume for LTWGS
$m_{rc,MTWGS}$	106000	kg	Mass for MTWGS
$m_{rc,LTWGS}$	45000	kg	Mass for LTWGS
$c_{p,rc,MTWGS}$	900	$J/K/kg$	Heat capacity of the catalyst and wall for MTWGS
$c_{p,rc,LTWGS}$	830	$J/K/kg$	Heat capacity of the catalyst and wall for LTWGS
V_{MTWGS}	106	m^3	Volume for MTWGS
V_{LTWGS}	45	m^3	Volume for LTWGS
$m_{rc,MTWGS}$	106000	kg	Mass for MTWGS
$m_{reac,LTWGS}$	45000	kg	Mass for LTWGS
$c_{p,rc,MTWGS}$	900	$J/K/kg$	Heat capacity of the catalyst and walls for MTWGS
$c_{p,rc,LTWGS}$	830	$J/K/kg$	Heat capacity of the catalyst and walls for LTWGS
π	16.4	-	Pressure ratio for compressor
$\dot{n}_{air,C}$	22.5	$kmol/s$	Inlet air flow rate for compressor
η_C	0.88	$-$	Isentropic efficiency for compressor
T_{TIT}	1230	$°C$	Turbine inlet temperature
$\dot{n}_{air,T}$	24.5	$kmol/s$	Inlet air flow rate for turbine
η_T	0.91	$-$	Isentropic efficiency for turbine
h_{HRSG}	-543880	$kJ/kmol$	Enthalpy of inlet stream for HRSG
P_{ST}	124	MW	Power generated by ST
V_{CC}	40	m^3	CC reactor volume
N	3000	rpm	Shaft rotational speed
η_{Mech}	0.99	-	Mechanical efficiency
P_{tot}	285	MW	Design value for GT power output

Table B.4: Data for inlet streams.

Variable	Unit	NG	Water	Air
T	$°C$	30	25	25
p	bar	30	1	1
Molar fraction	%			
H_2O		0	100	1.02
CO		0	0	0
CO_2		2.92	0	0.3
H_2		0	0	0
CH_4		79.76	0	0
C_2H_6		9.68	0	0
C_3H_8		4.45	0	0
C_4H_{10}		2.58	0	0
O_2		0	0	20.73
N_2		0.61	0	77.29
Ar		0	0	0.92
H_2S		0	0	0

Table B.5: Design values for the HMR power cycle 1: fuel streams.

Symbol	T $[°C]$	p $[bar]$	$\dot{n}$ $[kmol/s]$	From unit	To unit	Content
$S26$	30	30	0.81	-	HE1	NG
$S27$	180	29.9	0.81	HE1	HE4	
$S28$	400	29.8	0.81	HE4	Desulphurisation	
$S3$	333	29.8	2.8	Desulphurisation	HE22	Mixed NG and Steam
$S3\_1$	600	29.7	2.8	HE22	PR	
$S4$	567	28.6	3.17	PR	HE2	Pre-reformed NG
$S5$	750	25	3.17	HE2	HMR	
$S6$	1038	24.8	24.8	HMR	HE2	Syngas
$S7$	836	24.7	3.76	HE2	HE22	
$S7\_1$	555	24.6	3.76	HE22	PR	
$S8$	430	24.3	3.76	PR	HE4	
$S9$	342	24.3	3.76	HE4	HE5	
$S9\_1$	250	24.2	3.76	HE5	MTWGS	
$S11$	250	23.7	3.76	MTWGS	HE1	
$S12$	202	23.1	3.76	HE1	LTWGS	
$S13$	215	23.1	3.76	LTWGS	HE6	Mainly H_2, CO_2, H_2O
$S14$	134	23.1	3.76	HE6	HE7	
$S15$	90	23.1	3.76	HE7	HE8	
$S16$	25	23	3.76	HE8	FT	
$S19$	25	23	3.63	FT	CO_2 separator	Mainly H_2, CO_2,
$S20$	25	23	0.13	FT	-	H_2O
$S21$	27	23.5	2.72	CO_2 separator	HE6	Mainly H_2
$S22$	155	23.5	2.72	HE6	CC	

Table B.6: Design values for the HMR power cycle 2: steam and air steams.

Symbol	T [$°C$]	p [bar]	$\dot{n}$ [$kmol/s$]	From unit	To unit	Content
$S19\_1$	25	1.2	0.9	CO_2 separator	CO_2 compressor	CO_2
$S19\_2$	38	150	0.9	CO_2 compressor	-	
$S24$	155	23.5	0	BT	CC	Fuel from BT
$S31$	310	10	2.45	GT	HE9	GT extracted air
$S34$	173	10	2.45	HE9	HE11	
$S63$	50	10	2.45	HE11	Air compressor	
$S61$	152	24	2.45	Air compressor	HE9	
$S62$	290	24	2.45	HE9	HE3	
$S18$	750	23.9	2.45	HE3	HMR	
$S13$	1038	23.5	2.95	HMR	HE3	O_2 depleted air
$S29$	706	23.5	2.95	HE3	CC	
$SH1$	579	1	24.5	GT	HRSG	Turbine exhaust gas
$SH2$	364	32.4	2	HRSG	HE22	Extracted steam
$S37$	30	32	0.91	-	HE7	BFW
$S40$	126	32	0.91	HE7	HE5	
$S41$	240	31.9	0.91	HE5	HE22	
$S48$	15	1	4.21	-	HE11	Cooling water
$S49$	25	1	4.21	HE11	-	
$S51$	15	1	2.81	-	HE8	Cooling water
$S52$	45	1	2.81	HE8	-	

Appendix C

Evaluation of the dynamic model for each process unit

The dynamic model of the HMR power cycle is developed in Matlab/SIMULINK. Several strategies are implemented to increase the robustics of the models.

1. The minimal cell number or discretization grid which can capture the main dynamics is used for each process units to reduce the state number.
2. The states are scaled to make the values around 1.
3. The numerical solution method is ode15s. ode15s is a variable order solver based on the numerical differentiation formulas. It uses the backward differentiation formulas that are usually less efficient. It is used when the problem is stiff, or when solving a differential-algebraic problem (Shampine et al., 1999).

An Aspen plus model has been provided for this study by STATOIL. This model is a steady state model which includes all the units in the SIMULINK model and a detailed HRSG and ST model.

Six cases as listed in Table C.1 are used to tune and verify the SIMULINK model.

Table C.1: Six operating points for validation.

Cases	1	2	3	4	5	6
Air flow rate $[kmol/hr]$	2.5	2.55	2.45	2.5	2.5	2.5
S/C ratio $[kmol/kmol]$	2.0	2.0	2.0	1.9	2.1	2.5

In the following sections, some important variables are selected to demonstrate the difference between SIMULINK model and Aspen plus model.

C.1 Pre-reformer

Comparison between the Aspen plus and SIMULINK models are shown in Table C.2. The differences are relatively large, This is because the Aspen plus using a different design, which are

1. The model uses three sub models, one WGS reactor, and two heat exchangers, while the SIMULINK model uses one model to approximate the monolith reactor.

2. The Aspen model is a design model which means the area and catalyst weight can be adjusted to the desired output values, while these values are constant in SIMULINK model.

Table C.2: Comparison between the SIMULINK and Aspen plus, pre-reformer.

Symbol	$T_{S4}[°C]$	$T_{S8}[°C]$	$\dot{n}_{S4}[kmol/hr]$	λ_{S4,H_2O}
Mean difference	6.8	4.8	0.004	0.002
Symbol	$\lambda_{S4,CO}$	λ_{S4,CO_2}	λ_{S4,H_2}	λ_{S4,CH_4}
Mean difference	0	0.001	0.001	0.001

The dynamic responses with respect to two input step changes are shown in Figure C.1 and C.2. The temperature is scaled by T_{S3}. The molar fraction is unscaled, and the other variables are scaled by the design values. The time constant of PR is large because the large quantity of catalyst and the weight of reactor results in large heat capacity.

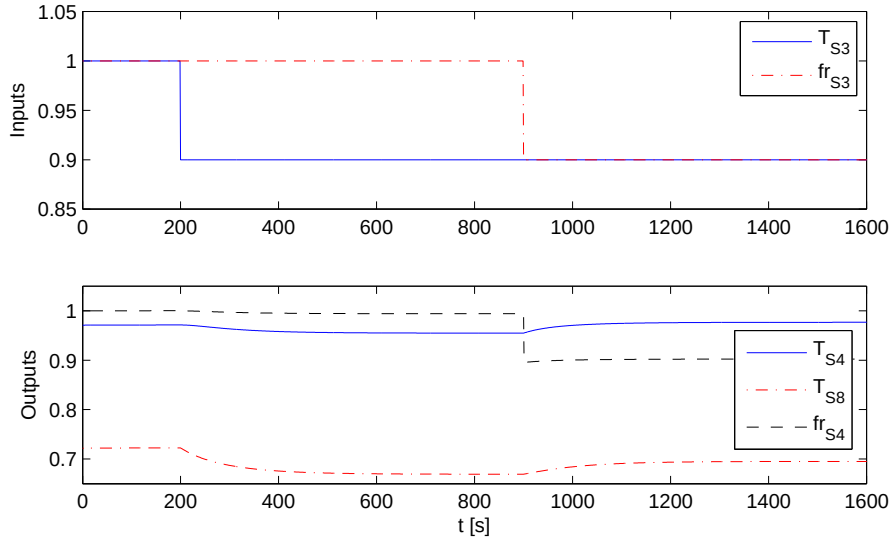

Figure C.1: Input changes and dynamic responses of temperature and flow rates.

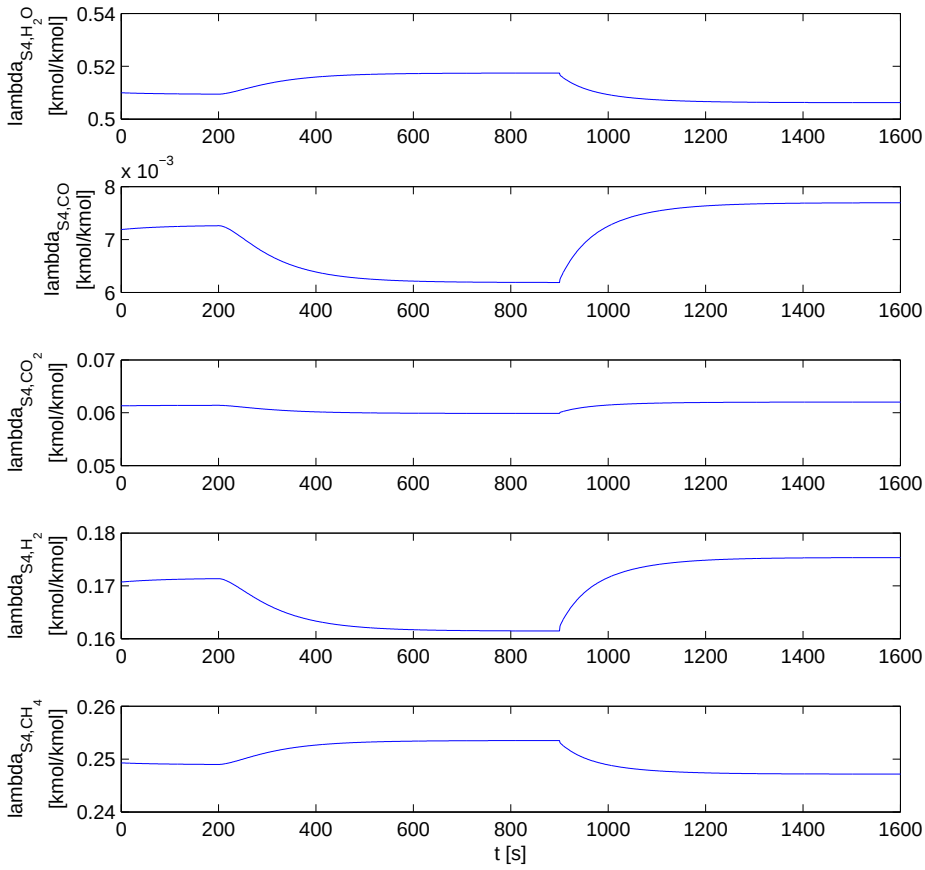

Figure C.2: Changes in molar fraction in the pre-reformer.

C.2 Hydrogen membrane reformer

Comparisons between Aspen plus model and SIMULINK model are shown in Table C.3.

The differences are caused by different model structures. Aspen plus model includes 4 models, e.g., the steam reforming reactor, the hydrogen separation, heat exchange and the sweep gas reactor, to approximate the monolith reactor. Further, the catalyst weight for SIMULINK model is constant, which gives different conversion rate for different inlet flows. The conversion rate is constant for different cases in Aspen plus model.

The dynamic responses for the HMR with respect to three input step changes, i.e., the inlet fuel temperature, the inlet fuel flow rate, and the inlet air flow rate are shown in Figure C.3 - C.5. The temperature is scaled by T_{S5}. The molar fraction is unscaled, and the other variables are scaled by design values. The responses of

Table C.3: Comparison between the SIMULINK and Aspen plus, HMR.

Variables	$T_{S6}[^{\circ}C]$	$\dot{n}_{S6}[kmol/hr]$	λ_{S6,H_2O}	$\lambda_{S6,CO}$
Mean difference	3.3	0.019	0.005	0.003
Variables	λ_{S6,CO_2}	λ_{S6,H_2}	λ_{S6,CH_4}	$T_{S13}[^{\circ}C]$
Mean difference	0.003	0.006	0.001	3.4
Variables	$\dot{n}_{S13}[kmol/hr]$	λ_{S13,H_2O}	λ_{S13,H_2}	λ_{S13,O_2}
Mean difference	0.011	0.001	0.003	0.001

the outlet flow rate, outlet molar fraction are nonlinear due to the fast velocity of the gas. An instant change of the inlet flow rate gives an instant change of the outlet concentration. Then the temperature and molar fractions are changing slowly because of the slowly varying reaction rate in the reactor.

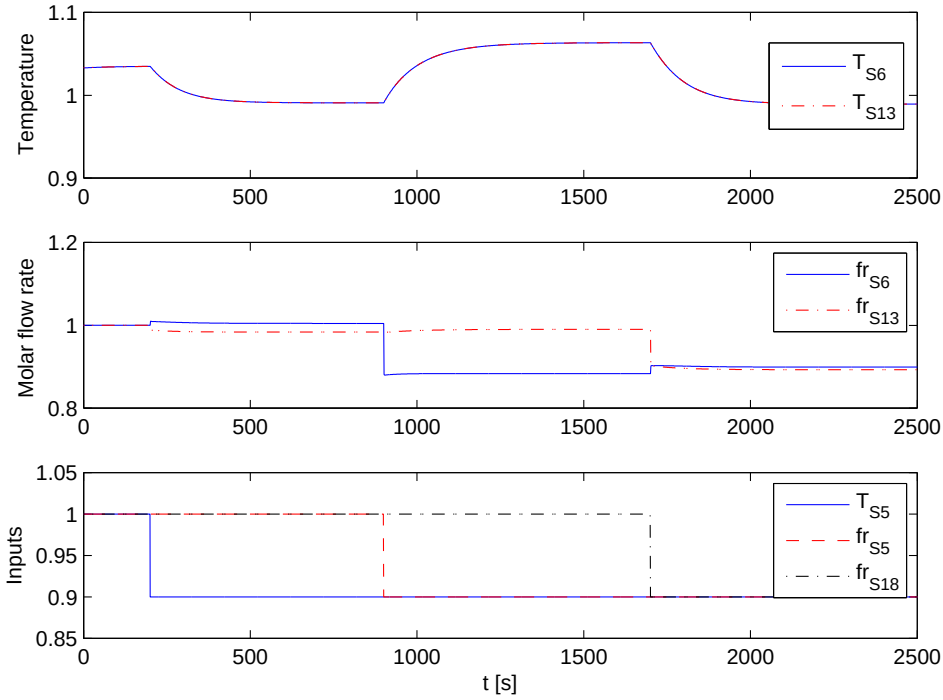

Figure C.3: Input changes and the responses of flow rate and temperature.

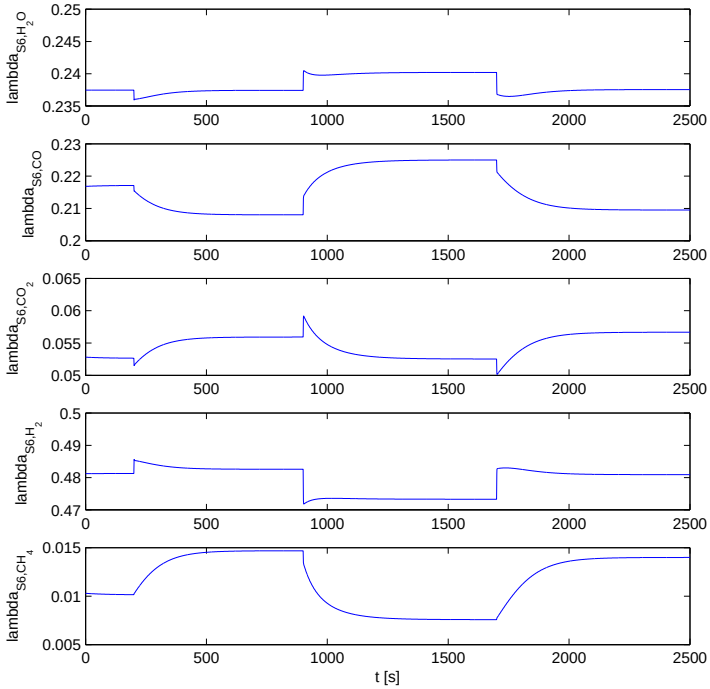

Figure C.4: Molar fraction changes of S6.

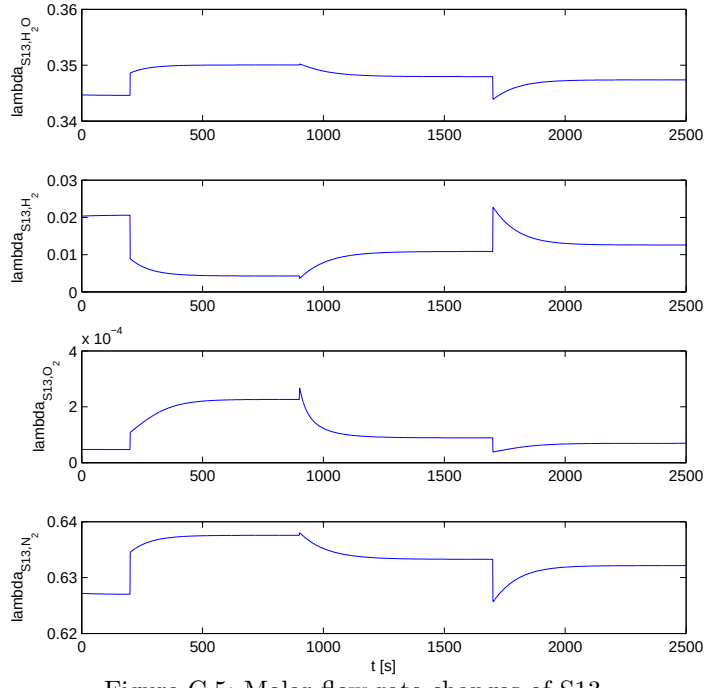

Figure C.5: Molar flow rate changes of S13.

C.3 Water gas shift

Comparisons between the steady state simulations from Aspen plus model and SIMULINK model are shown in Table C.4.

Table C.4: Compare the results from SIMULINK and Aspen plus, WGS.

Variables	$T_{S11}[°C]$	$T_{S41}[°C]$	$\dot{n}_{S41}[kmol/hr]$	$\lambda_{S41,CO}$	λ_{S53}
Mean difference	1.9	1.9	0.005	0.002	0.007

The dynamic responses of MTWGS and LTWGS with respect to two input step changes are depicted in Figure C.6 - C.9. All the variables are scaled by designed values. The figures indicate that the response time of MTWGS is doubled of LTWGS because of the doubled quality. Heat exchangers are integrated inside MTWGS, different inlet flow rate gives different heat transfer and this leads to a more significant response with respect to inlet flow rate changes of MTWGS than LTWGS.

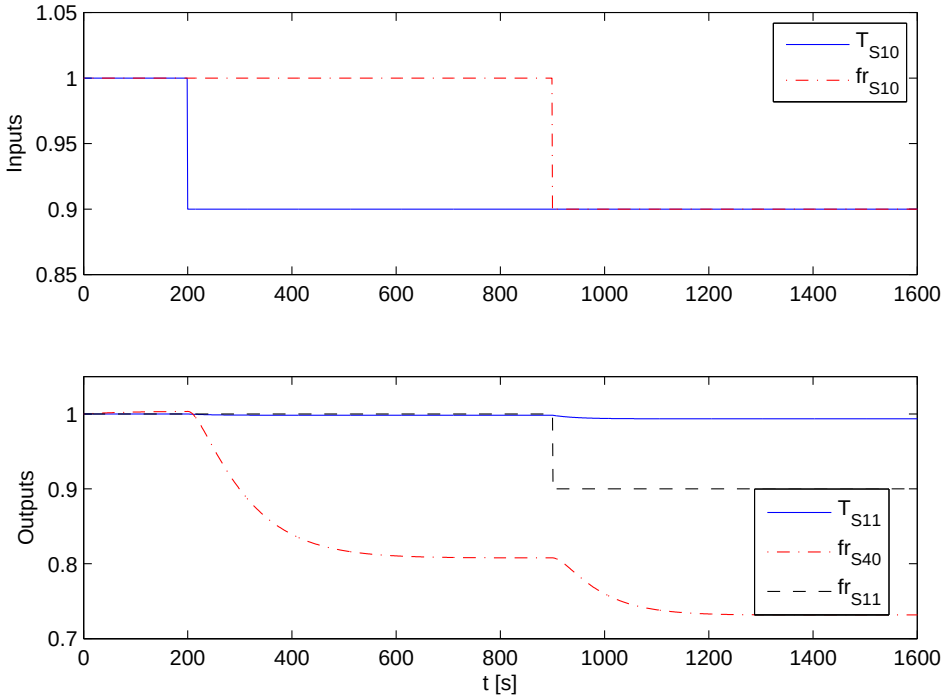

Figure C.6: Input changes and the responses of flow rate and temperature.

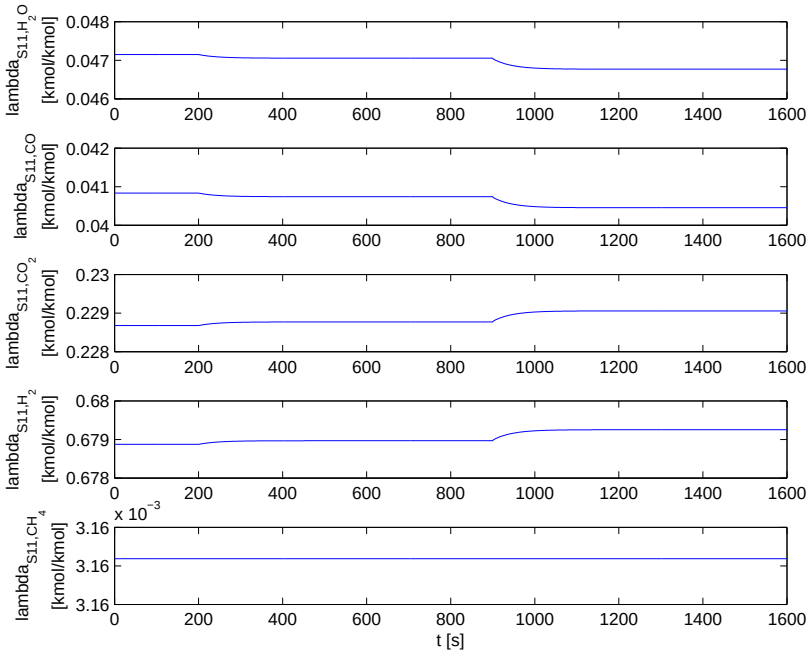

Figure C.7: Molar fraction responses of the MTWGS.

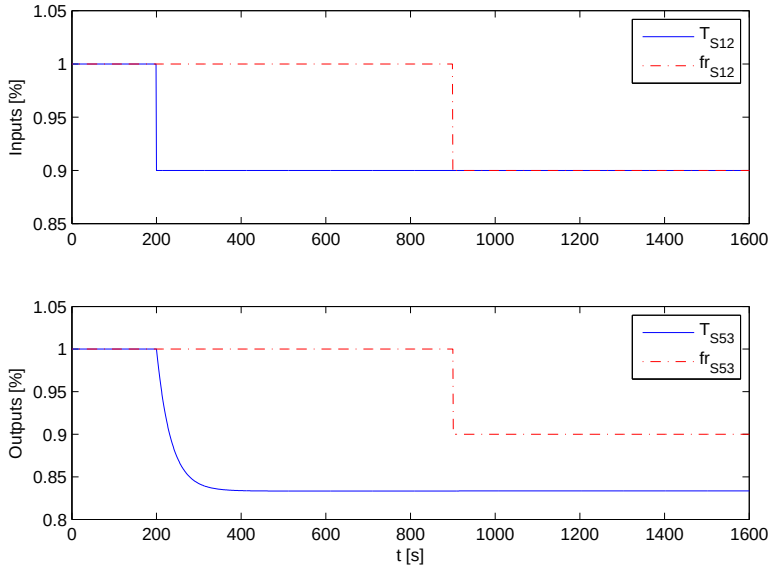

Figure C.8: Input changes and the flow rate and temperature responses of the LTWGS.

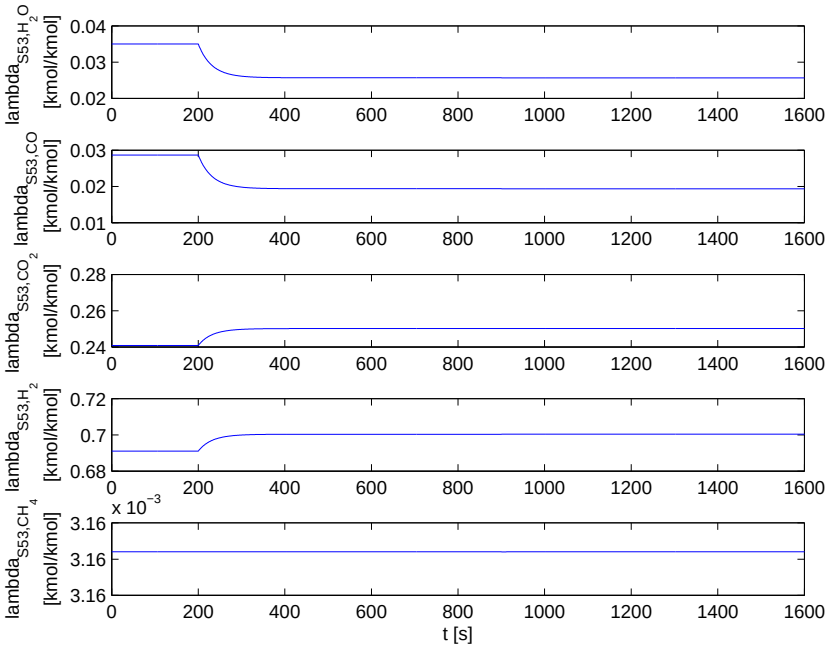

Figure C.9: Molar fraction responses of the LTWGS.

C.4 Combined cycle

Comparisons of the designed values between Aspen plus model and SIMULINK model are depicted in Table C.5.

Table C.5: Comparison between the results from SIMULINK and Aspen plus, GT.

Variables	$W_C[MW]$	$P_T[MW]$	$T_C[°C]$	TET $[°C]$
Mean difference	2.0088	0.0894	1.9742	0.0317

Here, W_C is the power required by compressor, P_T is the power generated by expander, T_C is the air temperature at the outlet of compressor.

The differences are caused by different model structures. In the Aspen plus model, two compressor and turbine models include real industrial performance maps, and the HRSG model includes detailed structures.

The designed power cycle uses a constant rotation speed, and a PI controller is added to stabilize the rotation speed by regulating the inlet fuel flow rate. The parameters of this control loop are in Table C.6.

Table C.6: Controllers for the rotation speed of GT.

Manipulated variables	Fuel flow rate $\dot{n}_{S24}$
Control variable	Rotation speed N
Setpoint	$3600rpm$
PI gain	$k_p = 80$, $k_i = 45$

The dynamic response for the combined cycle with respect to the load and extracted air changes are shown in Figure C.10. The power by GT and ST is scaled by the designed net outlet power, and the other variables are scaled by designed values. The system has a fuel controller, and the results show a nonlinear behavior. Less extraction of air from compressor at $10bar$ results a higher compressor work to compress the air from $10bar$ to $16.4bar$. In the design, the extracted air is future compressed by an air compressor. In this simulation to check the GT models, the assumption of a constant power by the air compressor is made. Higher fuel consumption and higher TIT are observed with respect to a step decrease of air extraction. The increased TIT is used to increase the power by expander and compensate the energy for the compressor. A decreased load results in a decreased power from both GT and ST.

C.5 Other components

Other components in SIMULINK model are mainly algebraic equations. The parameters are tuned to match Aspen Plus model.

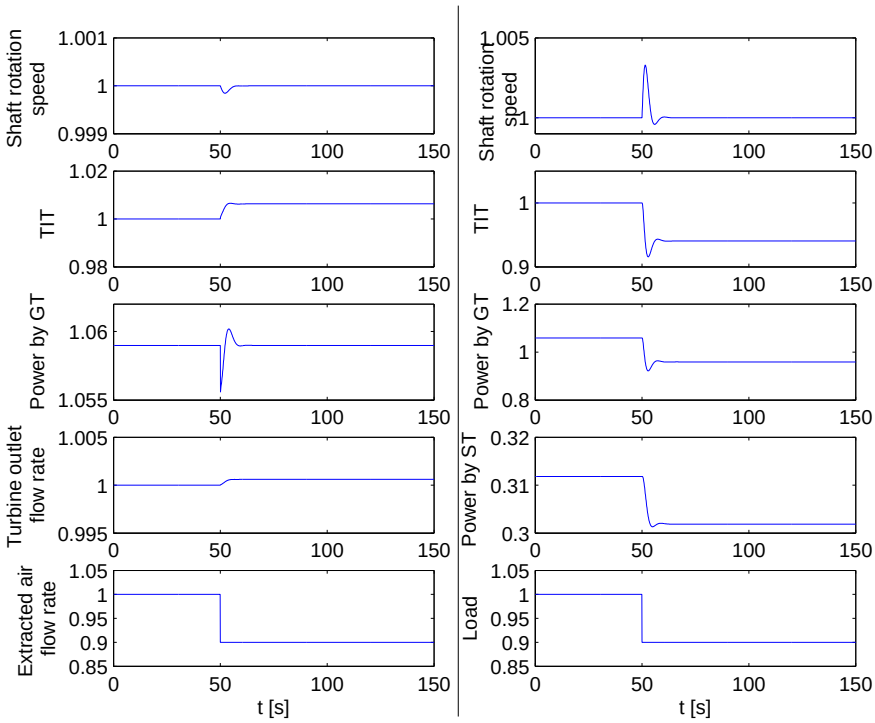

Figure C.10: Dynamic responses with respect to the extracted air flow rate changes (left) and the load changes (right).

References

S. Adhikari and S. Fernando. Hydrogen membrane separation techniques. *Industrial & Engineering Chemistry Research*, 45(3):875–881, 2006.

A. M. Adris, C. J. Lim, and J. R. Grace. The fluidized-bed membrane reactor for steam methane reforming: model verification and parametric study. *Chemical Engineering Science*, 52(10):1609–1622, 1997. ISSN 0009-2509. doi: 10.1016/S0009-2509(96)00511-8.

V. Alstad. *Studies on selection of controlled variables*. PhD thesis, Norwegian University of Science and Technology, Department of Chemical Engineering, 2005.

V. Alstad, S. Skogestad, and E. S. Hori. Optimal measurement combinations as controlled variables. *Journal of Process Control*, 19(1):138–148, Jan. 2009. ISSN 09591524. doi: 10.1016/j.jprocont.2008.01.002.

J. P. Ampaya and R. G. Rinker. Autothermal reactor with internal heat exchanger II: Numerical and preliminary experimental studies of transient behavior including startup in the multiple steady-state region. *Chemical Engineering Science*, 33(6):703–711, 1978. ISSN 0009-2509. doi: 10.1016/0009-2509(78)80048-7.

A. C. Antoulas, D. C. Sorensen, and S. Gugercin. A survey of model reduction methods for large-scale systems. In V. Olshevsky, editor, *AMS-IMS-SIAM joint summer research conference*, Boulder, 1999. American Mathematical Soc.

B. W. Bequette. *Process control: modeling, design, and simulation*. Prentice-Hall International Series in the Physical and Chemical Engineering Sciences. Prentice Hall PTR, 2003. ISBN 9780133536409.

J. Beyer. *Modelling and control of an ATR system for comparison with an HMR system*. PhD thesis, TU Dortmund, 2011.

O. Bolland. Thermal power generation, 2009.

A. C. Bose. *Inorganic membranes for energy and environmental applications*. Springer, 2008. ISBN 9780387345246.

R. Bredesen, K. Jordal, and O. Bolland. High-temperature membranes in power generation with CO_2 capture. *Chemical Engineering and Processing: Process Intensification*, 43(9):1129–1158, 2004. ISSN 0255-2701. doi: 10.1016/j.cep.2003.11.011.

P. S. Buckley. *Techniques of process control*. John Wiley and Sons, 1964.

Z. Chen, Y. Yan, and S. S. E. H. Elnashaie. Catalyst deactivation and engineering control for steam reforming of higher hydrocarbons in a novel membrane reformer. *Chemical Engineering Science*, 59(10):1965–1978, 2004. ISSN 0009-2509. doi: 10.1016/j.ces.2004.01.046.

P. Chiesa, G. Lozza, and L. Mazzocchi. Using hydrogen as gas turbine fuel. *Journal of Engineering for Gas Turbines and Power*, 127:73–80, 2005.

T. S. Christensen. Adiabatic prereforming of hydrocarbons - an important step in syngas production. *Applied Catalysis A: General*, 138(2):285–309, 1996. ISSN 0926-860X. doi: 10.1016/0926-860X(95)00302-9.

A. Corradetti and U. Desideri. Analysis of gas-Steam combined cycles with natural gas reforming and CO_2 capture. *Journal of Engineering for Gas Turbines and Power*, 127(3):545–552, 2005. doi: 10.1115/1.1850941.

K. Damen, R. Gnutek, J. Kaptein, N. R. Nannan, B. Oyarzun, C. Trapp, P. Colonna, E. van Dijk, J. Gross, and A. Bardow. Developments in the precombustion CO2 capture pilot plant at the Buggenum IGCC. *Energy Procedia*, 4(0):1214 – 1221, 2011. ISSN 1876-6102. doi: 10.1016/j.egypro.2011.01.176. 10th International Conference on Greenhouse Gas Control Technologies.

J. Davison. Performance and costs of power plants with capture and storage of CO_2. *Energy*, 32(7):1163–1176, July 2007. ISSN 03605442. doi: 10.1016/j.energy.2006.07.039.

F. P. de Mello, D. J. Ahner, P. M. Anderson, J. H.Doudna, P. Kundur, L. M. Richardson, G. Tandy, C. W.Taylor, and F. V. de Meulebroeke. Dynamic models for combined cycle plants in power system studies. *Power Systems, IEEE Transactions on*, 9(3):1698–1708, Aug. 1994. ISSN 0885-8950. doi: 10.1109/59.336085.

J. M. Douglas. *Conceptual design of chemical processes*. McGraw-Hill, 1988.

E. Drioli and L. Giorno. *Membrane operations: Innovative separations and transformations*. Wiley-VCH, 2009.

K. Eichhorn Colombo, V. V. Kharton, and O. Bolland. Simulation of an oxygen membrane-based gas turbine power plant: dynamic regimes with operational and material constraints. *Energy & Fuels*, 24(1):590–608, 2010. doi: 10.1021/ef9004253.

I. S. Ertesvåg, H. M. Kvamsdal, and O. Bolland. Exergy analysis of a gas-turbine combined-cycle power plant with precombustion CO_2 capture. *Energy*, 30(1):5–39, Jan. 2005. ISSN 03605442. doi: 10.1016/j.energy.2004.05.029.

D. Fiaschi, L. Lombardi, and L. Tapinassi. The recuperative-auto thermal reforming and the recuperative-reforming gas turbine power cycles with CO_2 removal—Part I: The recuperative-auto thermal reforming cycle. *Journal of Engineering for Gas Turbines and Power*, 125(4):933, 2003. ISSN 07424795. doi: 10.1115/1.1587743.

D. Fiaschi, L. Lombardi, and L. Tapinassi. The recuperative auto thermal reforming and recuperative reforming gas turbine power cycles with CO_2 removal—Part II: The recuperative reforming cycle. *Journal of Engineering for Gas Turbines and Power*, 126(1):62–68, 2004. doi: 10.1115/1.1639008.

M. Finkenrath. Cost and performance of carbon dioxide capture from power generation, 2011.

Global CCS Institute. The global status of ccs: 2011. Technical report, Global CCS Institute, Canberra, Australia, 2011.

M. S. Govatsmark. *Integrated optimization and control*. PhD thesis, Norwegian University of Science and Technology, Faculty of Engineering Science and Technology, 2004.

B. F. Hagh. Optimization of autothermal reactor for maximum hydrogen production. *International Journal of Hydrogen Energy*, 28(12):1369–1377, 2003. ISSN 0360-3199. doi: 10.1016/S0360-3199(02)00292-6.

Howard Herzog. An introduction to CO_2 separation and capture technologies. 1999.

IEA. Key World energy statistics. Technical report, IEA, 2011a.

IEA. World energy outlook 2011. Technical report, IEA, 2011b.

K. Iinoya and R. J. Altpeter. Inverse repsonse in process control. *Industrial & Engineering Chemistry*, 54(7):39–43, 1962. doi: 10.1021/ie50631a007.

L. Imsland, D. Snarheim, B. A. Foss, R. Ulfsnes, and O. Bolland. Control issues in the design of a gas turbine cycle for CO_2 capture. *International Journal of Green Energy*, 2(2):217–231, 2005. doi: 10.1081/GE-200058983.

L. A. Irwin. A high accuracy standard for electricity meters. *Schneider Electric*, 2011.

S. L. Jørgensen, P. Nielsen, and P. Lehrmann. Steam reforming of methane in a membrane reactor. *Catalysis Today*, 25(3):303–307, 1995.

R. Kandepu, B. Foss, and L. Imsland. Integrated modeling and control of a load-connected SOFC-GT autonomous power system. *American Control Conference 2006*, pages 3463–3468, 2006.

M. Kanniche, R. Gros-Bonnivard, P. Jaud, J. Valle-Marcos, J.-M. Amann, and C. Bouallou. Pre-combustion, post-combustion and oxy-combustion in thermal power plant for co2 capture. *Applied Thermal Engineering*, 30(1):53 – 62, 2010. ISSN 1359-4311. doi: 10.1016/j.applthermaleng.2009.05.005. Selected Papers from the 11th Conference on Process Integration, Modelling and Optimisation for Energy Saving and Pollution Reduction.

E. C. Kerrigan and J. M. Maciejowski. Soft constraints and exact penalty functions in model predictive control. In *The UKACC International Conference on Control*, 2000.

P. Kiameh. *Power generation handbook : selection, applications, operation, maintenance*. McGraw-Hill Professional, 2002.

J. Kurzke. How to get component maps for aircraft gas turbine performance calculations. In *ASME*, 1996.

T. Larsson and S. Skogestad. Plantwide control - A review and a new design procedure. *Modeling, Identification and Control*, 21(4):209–240, 2000. doi: 10.4173/mic.2000.4.2.

A. Lazzaretto and A. Toffolo. Analytical and neural network models for gas turbine design and off-design simulation. In *International Journal of Thermodynamics*, volume 4, pages 173–182, 2001.

L. Ljung. *System identification: Theory for the user*. Pearson Education, 1998. ISBN 9780132440530.

M. L. Luyben, B. D. Tyreus, and W. L. Luyben. Plantwide control design procedure. *AIChE Journal*, 1997.

J. Mantzaris and C. Vournas. Modelling and stability of a single-shaft combined cycle power plant. *Int. J. of Thermodynamics*, 10(2):71–78, 2007. ISSN 1301-9724.

Y. Matsumura and J. Tong. Methane steam reforming in hydrogen-permeable membrane reactor for pure hydrogen production. *Topics in Catalysis*, 51(1): 123–132, 2008. ISSN 1022-5528.

F. Michelsen, L. Zhao, and B. Foss. Operability analysis and control design of an IRCC cycle HMR unit with membrane leakage. *Energy Procedia (accepted)*, 2012.

F. A. Michelsen, I. J. Halvorsen, and B. F. Lund. The impact of process design decisions on operability and control of an LNG process. *Journal of Natural Gas Science and Engineering*, 2(4):183–191, 2010.

A. Mirandola. Full load and part load operation of gas turbine-steam turbine combined plant. In *ISEC*, 1986.

M. Morari, Y. Arkun, and G. Stephanopoulos. Studies in the synthesis of control structures for chemical processes: Part I: Formulation of the problem. Process decomposition and the classification of the control tasks. Analysis of the optimizing control structures. *AIChE Journal*, 1980.

C. Ng and G. Stephanopoulos. Plant-Wide control structures and strategies. *Preprints Dycops-5*, 1998.

J. Nocedal and S. Wright. *Numerical Optimization*. Springer Series in Operations Research. Springer, 1999. ISBN 9780387987934.

L. O. Nord, R. Anantharaman, and O. Bolland. Design and off-design analyses of a pre-combustion CO_2 capture process in a natural gas combined cycle power plant. *International Journal of Greenhouse Gas Control*, 3(4):385–392, 2009. ISSN 1750-5836. doi: 10.1016/j.ijggc.2009.02.001.

P. Overschee and B. L. R. Moor. *Subspace identification for linear systems: theory, implementation, applications*. Number v. 1. Kluwer Academic Publishers, 1996. ISBN 9780792397175.

C. E. G. Padro and V. Putsche. *Survey of the Economics of Hydrogen Technologies*. National Renewable Energy Laboratory, Golden, Colorado, 1999.

J. B. Rawlings and D. Q. Mayne. *Model predictive control theory and design*. Nob Hill Pub, Llc, 2009. ISBN 9780975937709.

R. Richards. *Surface and nanomolecular catalysis*. Taylor, 2006. ISBN 9781574444810.

P. J. Robinson and W. L. Luyben. Plantwide control of a hybrid integrated gasification combined cycle/methanol plant. *Industrial and Engineering Chemistry Research*, 50(8):4579–4594, 2011. doi: 10.1021/ie102219k.

J. Romagnoli and A. Palazoğlu. *Introduction to process control*. Chemical Industries. Taylor & Francis, 2006. ISBN 9780849334962.

J. A. Rossiter. *Model-based predictive control: a practical approach*. CRC Press control series. CRC Press, 2003. ISBN 9780849312915.

J. R. Rostrup-Nielsen. Activity of nickel catalysts for steam reforming of hydrocarbons. *Journal of Catalysis*, 31(2):173–199, 1973.

J. R. Rostrup-Nielsen and T. Rostrup-Nielsen. Large-Scale hydrogen production. *CATTECH*, 2002.

H. I. H. Saravanamuttoo, G. F. C. Rogers, and H. Cohen. *Gas turbine theory*. Prentice Hall, 2009. ISBN 9780132224376.

F. Seibert, E. Chen, M. Perry, S. Briggs, R. Montgomery, and G. Rochelle. UT/SRP CO_2 capture pilot plant - Operating experience and procedures. *Energy Procedia*, 4(0):1616 – 1623, 2011. ISSN 1876-6102. doi: 10.1016/j.egypro.2011.02.032. 10th International Conference on Greenhouse Gas Control Technologies.

L. F. Shampine, M. W. Reichelt, and J. A. Kierzenka. Solving index-I DAEs in MATLAB and Simulink. *SIAM Review*, 41(3):pp. 538–552, 1999. ISSN 00361445.

D. Simon. *Optimal state estimation: Kalman, H∞ and nonlinear approaches*. Wiley-Interscience, 2006. ISBN 9780471708582.

S. Skogestad. Control structure design for complete chemical plants. *Computers and Chemical Engineering*, 28(1-2):219–234, Jan. 2004. ISSN 00981354. doi: 10.1016/j.compchemeng.2003.08.002.

S. Skogestad and I. Postlethwaite. *Multivariable feedback control: analysis and design*. John Wiley, 2005.

J. B. Smith, K. I. Aasen, K. Wilhelmsen, D. Kaka, T. Risdal, A. Berglund, A. S. Ostby, M. Budd, T. Bruun, and B. Werswick. Recent development in the HMR pre-combustion gas power cycle. *Energy Procedia*, 1:343–351, 2009. ISSN 1876-6102.

R. W. Smith, P. Polukort, C. E. Maslak, C. M. Jones, and B. D. Gardine. *Advanced technology combined Cycle*. GE Power System, Schenectady, NY, 2002.

T. Sperle, D. Chen, R. Lødeng, and A. Holmen. Pre-reforming of natural gas on a Ni catalyst: Criteria for carbon free operation. *Applied Catalysis A: General*, 282:195–204, 2005. ISSN 0926-860X. doi: 10.1016/j.apcata.2004.12.011.

STATOIL. HMR model. *Internal company report*, 2008.

C. Stiller. *Design, operation and control modelling of SOFC and GT hybrid systems*. PhD thesis, Norwegian University of Science and Technology, Faculty of Engineering Science and Technology, 2006.

C. Stiller, B. Thorud, O. Bolland, R. Kandepu, and L. Imsland. Control strategy for a solid oxide fuel cell and gas turbine hybrid system. *Journal of Power Sources*, 158(1):303–315, 2006. ISSN 0378-7753. doi: 10.1016/j.jpowsour.2005.09.010.

Thermoflow Inc. GT PRO/GT MASTER, 2011. URL `http://www.thermoflow.com/`. Version 21.

B. Thorud. *Dynamic modelling and characterisation of a solid oxide fuel cell integrated in a gas turbine cycle*. PhD thesis, Norwegian University of Science and Technology, Department of Energy and Process Engineering, 2005.

T. Umeda and T. Kuriyama. A logical structure for process control system synthesis. *Proceed of IFAC Congress*, 1978.

Union Gas. Chemical composition of natural gas, 2012. URL `http://www.uniongas.com/aboutus/aboutng/composition.asp`.

K. V. T. Waller and C. G. Nygardas. On inverse repsonse in process control. *Industrial & Engineering Chemistry Fundamentals*, 14(3):221–223, 1975. doi: 10.1021/i160055a014.

C. H. Whitson and M. L. Michelsen. The negative flash. *Fluid Phase Equilibria*, 53(0):51–71, 1989. ISSN 0378-3812. doi: 10.1016/0378-3812(89)80072-X.

J. Xu and G. F. Froment. Methane steam reforming, methanation and water-gas shift: I. Intrinsic kinetics. *AIChE Journal*, 35(1):88–96, Jan. 1989. ISSN 0001-1541. doi: 10.1002/aic.690350109.

Q. Zhang and P. L. So. Dynamic modelling of a combined cycle plant for power system stability studies. *Power Engineering Society Winter Meeting, 2000. IEEE*, 2:1538 –1543 vol.2, 2000. doi: 10.1109/PESW.2000.850211.

W. Zhang, X. Xu, and Y. Sun. Quantitative performance design for inverse-response processes. *Industrial & Engineering Chemistry Research*, 39(6):2056–2061, 2000. doi: 10.1021/ie990067z.